SPRINGER BRIEFS IN
PETROLEUM GEOSCIENCE & ENGINEERING

Mehdi Ostadhassan · Kouqi Liu
Chunxiao Li · Seyedalireza Khatibi

Fine Scale Characterization of Shale Reservoirs

Methods and Challenges

Springer

SpringerBriefs in Petroleum Geoscience & Engineering

The SpringerBriefs series in Petroleum Geoscience & Engineering promotes and expedites the dissemination of substantive new research results, state-of-the-art subject reviews and tutorial overviews in the field of petroleum exploration, petroleum engineering and production technology. The subject focus is on upstream exploration and production, subsurface geoscience and engineering. These concise summaries (50–125 pages) will include cutting-edge research, analytical methods, advanced modelling techniques and practical applications. Coverage will extend to all theoretical and applied aspects of the field, including traditional drilling, shale-gas fracking, deepwater sedimentology, seismic exploration, pore-flow modelling and petroleum economics. Topics include but are not limited to:

- Petroleum Geology & Geophysics
- Exploration: Conventional and Unconventional
- Seismic Interpretation
- Formation Evaluation (well logging)
- Drilling and Completion
- Hydraulic Fracturing
- Geomechanics
- Reservoir Simulation and Modelling
- Flow in Porous Media: from nano- to field-scale
- Reservoir Engineering
- Production Engineering
- Well Engineering; Design, Decommissioning and Abandonment
- Petroleum Systems; Instrumentation and Control
- Flow Assurance, Mineral Scale & Hydrates
- Reservoir and Well Intervention
- Reservoir Stimulation
- Oilfield Chemistry
- Risk and Uncertainty
- Petroleum Economics and Energy Policy

Contributions to the series can be made by submitting a proposal to the responsible Springer contact, Charlotte Cross at charlotte.cross@springer.com or the Academic Series Editor, Prof Dorrik Stow at dorrik.stow@pet.hw.ac.uk.

More information about this series at http://www.springer.com/series/15391

Mehdi Ostadhassan · Kouqi Liu
Chunxiao Li · Seyedalireza Khatibi

Fine Scale Characterization of Shale Reservoirs

Methods and Challenges

Springer

Mehdi Ostadhassan
Department of Petroleum Engineering
University of North Dakota
Grand Forks, ND
USA

Chunxiao Li
Department of Petroleum Engineering
University of North Dakota
Grand Forks, ND
USA

Kouqi Liu
Department of Petroleum Engineering
University of North Dakota
Grand Forks, ND
USA

Seyedalireza Khatibi
Department of Petroleum Engineering
University of North Dakota
Grand Forks, ND
USA

ISSN 2509-3126 ISSN 2509-3134 (electronic)
SpringerBriefs in Petroleum Geoscience & Engineering
ISBN 978-3-319-76086-5 ISBN 978-3-319-76087-2 (eBook)
https://doi.org/10.1007/978-3-319-76087-2

Library of Congress Control Number: 2018934917

Printed on acid-free paper

This Springer imprint is published by the registered company Springer International Publishing AG part of Springer Nature
The registered company address is: Gewerbestrasse 11, 6330 Cham, Switzerland

This book is dedicated to the following scientists:

Dr. Thomas Gentzis, Dr. Vamegh Rasouli

&

Mr. David Tuschel

who have kindly supported us to create this book.

Acknowledgements

Preparing the material that is presented in this book entailed a huge amount of analytical assessments, data processing, and interpretation. The amount of hours that was invested in developing each chapter of this book was significant. This included sample preparation, laboratory testing, data reduction, interpretation, and processing of the data. In addition to all these efforts, the extended time of discussions that was dedicated to each topic among the authors as well as our industry and academic collaborators was notable. The scientific merit of this book could not have been achieved without our collaborators' support and input.

The authors would like to express their sincere appreciation, first and foremost to Dr. Thomas Gentzis from Reservoir Geology Group at Core Laboratories in Houston, TX. Thomas is the one who made this book possible in the first place. We are grateful to him for his invaluable supports in many numerous ways and also the Core Laboratories in Houston, TX, for collaborative projects that created high-quality data for several journal publications and of course preparation of this book. We would like to extend our gratitude to Dr. Humberto Carvajal-Ortiz from Reservoir Geology Group at Core Laboratories in Houston, TX, for great discussions and sample processing for geochemical analysis specifically.

The authors of this book would like to express their appreciation to Mr. David Tuschel from Horiba Scientific and his company for tremendous support for testing the samples for Raman Spectroscopy, data analysis, and feedback for interpretations. David's input and knowledge of the field made us very confident about the results that we presented in this book or the manuscripts that are cited here.

Last but not least, Dr. Vamegh Rasouli, Chair of the Petroleum Engineering Department is the one who pushes us to work harder and to seek more collaborative opportunities with industry every day. He is the one who has inspired us to tackle problems and find solutions for obstacles in any shape or form that could have kept us away from more scholarly activities and scientific research. He has provided a significant amount of financial support to make many of these studies and future upcoming ones possible. The authors need to thank Bailey Bubach, one of our main

collaborators for her in-depth understanding and knowledge about the geology of the Williston Basin, ND, which always makes us pick the right samples in the shortest period of time.

Finally, we would like to express our sincere appreciation to North Dakota Core Library for providing us with an adequate number of samples whenever it is requested, the director Jeff Bader and Kent Holland, laboratory technician, in particular. This book happened because of the support and kindness that we have received from our families, friends, and our team members through the past years.

Contents

Chapter 1
Geology

Abstract The Bakken Formation in the Williston Basin, North Dakota, USA, is an unconventional reservoir that has been one of the major producers of oil for almost 50 years. Recently with new advancements in horizontal drilling, hydraulic fracturing and Enhanced Oil Recovery (EOR) techniques, this formation is considered one of the most prolific oil shale plays in the U.S. and around the globe. The combination of all these technologies have highly increased oil production from the Bakken, resulting the state of North Dakota becoming one of the largest oil producers in America. Innovative production technologies in the Bakken has introduced new challenges to the oil industry which can jeopardize successful stimulation, horizontal drilling operations, EOR and hydraulic fracturing. Considering the fact that unconventional shale plays are becoming a major source of energy recently along with shales being the main constituent of all sedimentary basins around the world, we need to address the problems that would encounter in tight shale oil formations for better field operations. Geomechanical modeling, which plays a significant role for a successful field operation, is one of the major concerns which is notably based on a good understanding of various components within any formation. We need to characterize different shale components and their elastic parameters to input them in different rock physics models to improve mechanical earth modeling (MEM). These formations have a large total organic carbon (TOC) content which is not common in conventional reservoirs. Organic matter which is the reason for high TOC has totally a different physio-chemical properties than other rock forming components. Neglecting to include these properties in our modeling will lead to failure and costly operation. Although the importance of such information organic matter characteristics still requires major investigations. Additionally, the pore spaces where hydrocarbons are stored are very small scale compared to conventional reservoirs which makes the permeability or the flow pathways abnormal. Therefore, we have to expand more in-depth studies in various scales of measurements from nano to macro and mega, to examine how production from this reservoirs can be enhanced from 3% to recovery factor levels of conventional reservoirs. In order to focus our studies in a very small scale, more advanced analytical techniques should be developed and employed.

M. Ostadhassan et al., *Fine Scale Characterization of Shale Reservoirs*,
SpringerBriefs in Petroleum Geoscience & Engineering,
https://doi.org/10.1007/978-3-319-76087-2_1

1.1 Organization of This Book

This book presents various subjects that will help us to better characterize the Bakken Formation both as a source rock and a reservoir rock. The authors have tried to address problems that scientists would face while, modeling of the Bakken Formation to improve existing rock physics models. The main objective of this manuscript is to include various physical and chemical properties of different components of the Bakken Formation that are mostly unknown to us in geomechanical, geophysical and geological modeling. Such properties in the Bakken Formation is believed to originate from a combination of factors such as a large presence of clay minerals, high concentration of organic matter with various origins, a wide range of small pore sizes and heterogeneous distribution of them. However, recent improvements in materials science and medical field have facilitated characterization of these properties with high accuracy in the lab. The organization of this book follows the following chapters:

Chapter 1 discusses different shale plays and how they are distributed geographically throughout the U.S. as well as their importance. A brief geological setting of the basin and the Bakken Formation, with the operational history in the Williston Basin is provided as well. We have also presented various organic petrography images of different macerals that are found in the samples to form the Bakken Formation organic matter. A detail of organic geochemistry analysis along with kerogen type is presented in this chapter. Readers will find more organic geochemistry analysis in later chapters since the authors' goal was to tie thermal maturity variations to physical and chemical characteristics of the Bakke samples.

Due to the importance of pore structures in controlling the capacity of the oil and gas stored in the reservoir, Chap. 2 is dedicated to a detailed study of pore network. Different properties such as pore size and shape which can impact the physical, mechanical and chemical properties of the rocks including strength, elastic modulus, permeability, and conductivity have been analyzed. Pore structures are characterized and quantified in several scales of measurements with different techniques including gas adsorption, imaging methods combined with advanced data analysis to better understand pore heterogeneity.

Shale reservoirs with organic-rich intervals are often characterized by high quantities of kerogen, bitumen and also moveable hydrocarbons. Despite lots of conducted studies to improve understanding of kerogen characteristics, as one the main constituents of mudrocks, this component is not thoroughly understood. Hence Chap. 3 of this book presents our understanding from organic matter properties in terms of maturity, content type which is crucial for the development of unconventional reservoirs. In this chapter, conventional geochemical methods along with a new analytical techniques, Raman spectroscopy in particular, are discussed for organic matter characterization.

Finally mechanical properties of shale samples in micro- and nano-scale are being investigated in Chap. 4. Nanoindentation and Atomic Force microscopy were used examine elastic modulus and hardness from the force-displacement curves.

AFM PeakForce quantitative nanomechanical mode is a relatively new method of measurement in AFM probing to produce maps of surface height and modulus at the same time. In this chapter, we report the application of these two techniques on shale samples taken from the Bakken and also the advantages and shortages of each techniques were also discussed. This chapter addresses one of the main understudied properties of organic matter. The reason for lack of information in this area is availability of advanced equipment that can isolate the organic matter and measures is mechanical properties in situ. Nanomechanical properties of organic matter was tested by a new mode in AFM and then was correlated with its thermal maturity.

1.2 U.S. Shale Plays

Significant activities have been carried out in the U.S. to explore and develop America's shale oil plays. The term shale oil plays contain "fine grained, organic rich, sedimentary rocks" where they are both the source and the reservoir for hydrocarbons. They are also defined by the extremely small pore sizes which make them relatively impermeable to fluid flow, unless natural or artificial fractures occur.

To gain a better understanding of the potential U.S. domestic shale oil resources, Energy Information Administration (EIA) commissioned INTEK, Inc. to develop an assessment of onshore Lower 48 States technically recoverable shale oil resources (U.S. Energy Information Administration 2015). This report estimates shale oil resources for the undeveloped portions of 20 shale plays that have been discovered. Eight of those shale plays are subdivided into 2 or 3 areas, resulting in a total of 29 separate resource assessments. The map in Fig. 1.1 shows the location of the shale plays in the Lower 48 States.

According to the shale report's assessment there are 23.9 billion barrels of recoverable of shale oil in the onshore Lower 48 States. The largest shale oil formation is the Monterey/Santos play in southern California, which is estimated to hold 15.4 billion barrels or 64 percent of the total shale oil resources. The Monterey shale play is the primary source rock for the conventional oil reservoirs found in the Santa Maria and San Joaquin Basins in southern California. The next largest shale oil plays are the Bakken and the Eagle Ford, which are assessed to hold approximately 3.6 billion barrels and 3.4 billion barrels of oil, respectively.

Table 1.1 summarizes the amount of recoverable resources in Billion Barrels of Oil (BBO) of major U.S. shale oil plays with the area of extension in square miles. The Estimated Ultimate Recovery (EUR) in thousands barrels (MBO) per well is denoted in the last column (U.S. Energy Information Administration 2017).

In the lower 48 states, unconventional (tight) oil development dominates as the main driver of total U.S. oil production. According to EIA's latest projections, tight shale will account for 60% of the total cumulative domestic production between 2016 and 2040 (U.S. Energy Information Administration 2017) (Fig. 1.2). The following image shows the production of crude oil in the U.S. compared with other

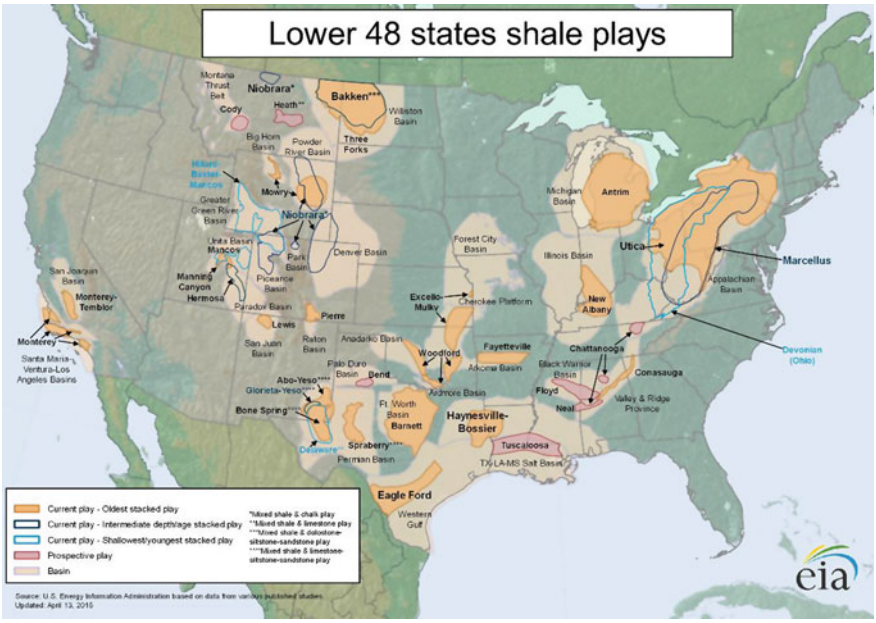

Fig. 1.1 Map of major U.S. shale plays including the Bakken in Williston Basin, ND. *Source* U. S. Energy Information Administration 2015

Table 1.1 Technically recoverable resources in some of the U.S. major shale plays

Region/basin	Play	Area with potential	Average EUR Crude oil	Technically recoverable resources
		(Sq. Miles)	(MMb/well)	(BBO)
Gulf coast				
Western Gulf	Eagle Ford	14,780	0.491	15.5
Western Gulf	Austin Chalk	11,447	0.122	4.7
Western Gulf	Tuscaloosa	7388	0.124	3.7
Southwest				
Permian	Spraberry	15,684	0.098	10.6
Permian	Wolfcamp	18,491	0.151	11.1
Rocky mountain/Dakotas				
Powder River	Tight Oil Plays	19,684	0.035	2.1
Williston	Bakken	14,966	0.953	8.6
Williston	Bakken Three Forks	21,439	0.197	14.9

top producers around the globe. A very interesting aspect of this graph, is the jump in U.S. production in 2010 which is well correlated with the dramatic increase in production in the state of North Dakota. The comparison of these two curves

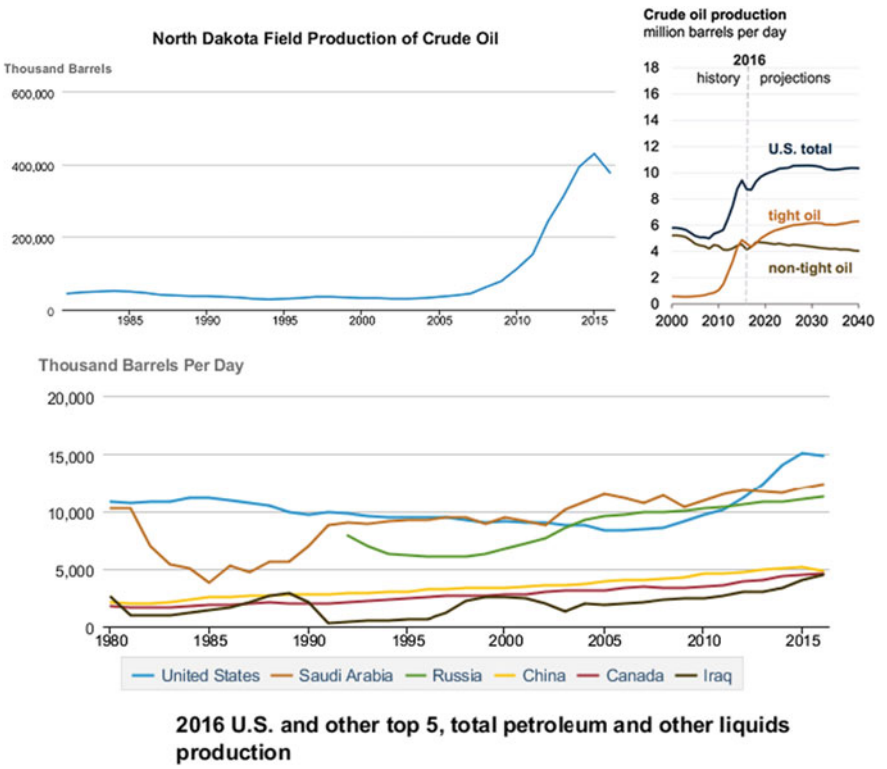

Fig. 1.2 U.S. versus North Dakota crude oil production and projection. *Source* U.S. Energy Information Administration 2017

reveals the importance of the Bakken Formation which accounts for majority of production in Williston Basin, ND. Due to the importance, this book and analysis that is provided is dedicated and focused on the samples from the Bakken Formation, one of the main shale oil plays in the U.S. and in the world.

1.2.1 History of the Bakken

Oil production from the Bakken goes back to 1950 when Antelope field discovery took place. The Bakken production and development history then continued by more vertical drilling when the first horizontal well was drilled in the beginning of 1990s. The Parshall Field discovery in 2006 was a breakthrough in the Bakken production history and caused a skyrocket in the number of horizontal wells drilled in the region. Production from the low permeability Bakken has been significantly enhanced by technologies like horizontal drilling and new stimulation techniques,

such as multi-stage hydraulic fracturing. The Bakken is characterized as a "resource play" or "self-sourced" where all the wells are productive, and the petroleum system, source, reservoir and seal are intermixed.

The Bakken shale oil play is located within the Williston Basin in Montana and North Dakota and extends into the Canadian provinces of Manitoba and Saskatchewan. In 2008, USGS conducted an assessment of the Bakken shale (Pollastro et al. 2008) showing that the total undiscovered resource was estimated between 3063 and 4319 MMOE (Million Barrels of Oil Equivalent), with a mean at 3645 MMBO (Million Barrels of Oil Equivalent) of total continuous resources (U.S. Energy Information Administration 2011). According to EIA's more recent estimates, the Bakken oil play contains an estimated 8.6 billion barrels in technically recoverable reserves which would be the largest finding in U.S. history (U.S. Energy Information Administration 2017). A net acreage area for Bakken is

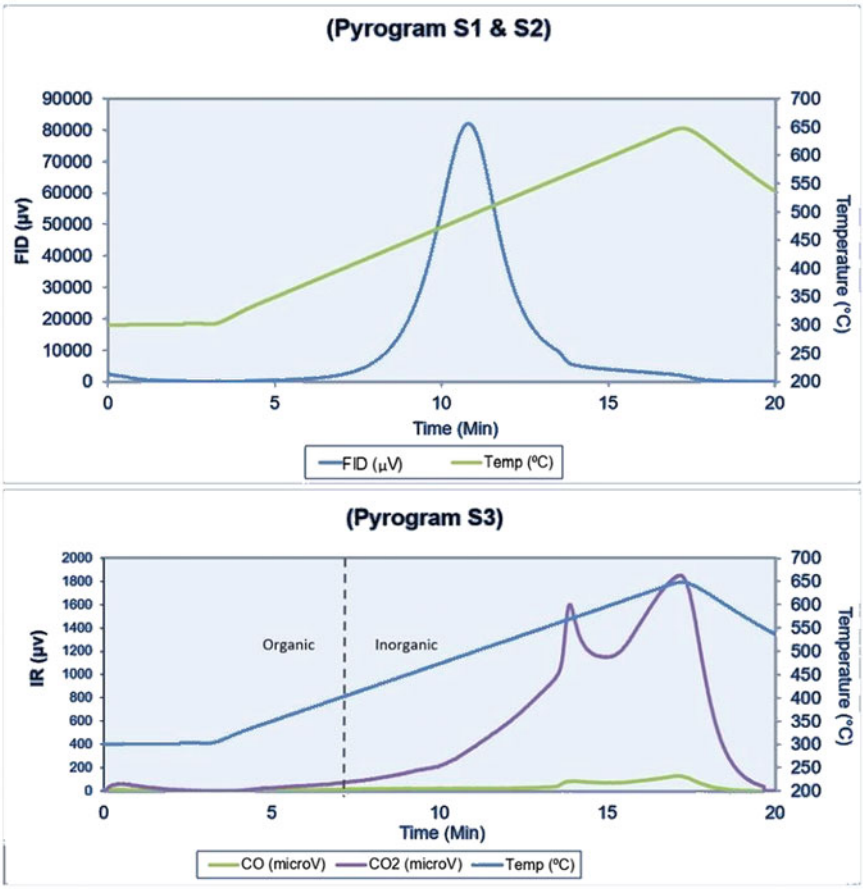

Fig. 1.3 Rock-Eval pyrolysis pyrogram for a sample of the Bakken shales

approximately 14,966 square miles in the U.S. The shale oil play has an average EUR of 953 MBO per well. Figure 1.3 provides a representative type curve for the Middle Bakken and the Three Forks as the main reservoirs in the Bakken play for the state daily production.

1.2.2 Geological Setting of the Bakken

The Bakken petroleum system in Williston Basin is one of the most important unconventional shale plays in North America. The Late Devonian to Early Mississippian Bakken Formation is a widespread clastic formation and occupies portions of North Dakota, Montana, and the Canadian provinces of Saskatchewan and Manitoba. The Bakken Formation consists of three members; the upper and lower members which are black organic-rich shales and the middle member, which is comprised of carbonaceous sandstone and siltstone (LeFever et al. 1991; LeFever 2008). In North Dakota, all three members of the Bakken Formation have an onlap truncation pattern with surrounding sediments and each member has more extensive spread than the older one. The onlapping geometry of the members could have occurred due to a transgression of the Late Devonian-Early Mississippian Sea (Webster 1984; Meissner 1991). The Bakken Formation is underlain by the Three Forks Formation and is overlain by the Lodgepole Formation. This succession creates the Bakken Petroleum System. This system is characterized by low porosity and permeability reservoirs, organic-rich source rocks, and a regional hydrocarbon charge (Sonnenberg and Pramudito 2009).

Conodonts, Tasmanites algae, amber-colored spores, small cephalopods, ostracodes, small brachiopods, and also fish remains are the most abundant fossil assemblages of the Bakken (Wall 1962; Hayes 1985). Presence of the mentioned fauna and flora assemblages, as well as the planar and thin laminations in the Bakken Shale, indicate that deposition has taken place in very low energy water conditions. The very high concentrations of organic matter and pyrite in the Lower and Upper Bakken represent a reducing, deep stratified, and anoxic depositional environment while the middle Bakken was deposited in well oxygenated water (LeFever 1991). The concept of the Devonian-Mississippian "Black Shale Sea" of North America (Ettensohn and Barron 1981) and also a stratified water column in the Williston Basin during Bakken deposition (Lineback and Davidson 1982) is confirmed by the presence of nectonic (fish, cephalopods, and ostracodes), planktonic (algal spores), and epiplanktonic (inarticulate brachiopods) fossil fauna abundance (Webster 1984).

The Bakken Formation has a maximum thickness of 150 ft. ($\sim$50 m) in the central part of the basin without any surface outcrop (LeFever et al. 1991). The formation is a unique case study for geochemical analysis since all stages of thermal maturity (from immature to relatively post-mature stages) can be recognized within a single stratigraphic unit (Webster 1984). The upper and lower shales of the Bakken consist mostly of hard, brittle, waxy-looking black shale, having a very dark brown color. The upper shale mostly consists of organic matter with lesser

amounts of clay, silt, and dolomite grains whereas the lower shale member appears to become less organic-rich and more-clayey, silty, and dolomitic (Meissner 1991).

Different methods have been suggested to determine the source rock potential and quality (Jackson et al. 1980; Epistalié et al. 1985; Tissot and Welte 1978; Peters 1986; Langford and Blanc-Valleron 1990; Bordenave 1993; Peters and Cassa 1994; Burwood et al. 1995; Hunt 1996; Dyman et al. 1996; Lafargue et al. 1998; Petersen and Nytoft 2006; Dembicki 2016). Rock-Eval analyses is the most common analyses initiated on rock samples to assess various bulk geochemical characteristics. This technique were first used to assess the source potential and thermal maturity of cuttings, core, or outcrop samples as an initial screening step.

1.2.3 Organic Geochemistry and Rock Eval Pyrolysis

TOC (wt%), representing organic richness, S_1 (mg HC/g Rock), as free, thermally extractable hydrocarbons present in the whole rock sample, S_2 (mg HC/g Rock), as the hydrocarbons resulting from the cracking of the remaining kerogen and high molecular weight free hydrocarbons that do not vaporize in the S_1 peak, and Tmax (°C) as the temperature of maximum rate of evolution of S_2 hydrocarbons, S_3 (mg CO_2/g Rock) as the organic carbon dioxide evolved during low temperature pyrolysis (<390°C), S_4 (mg/g Rock) as the residual carbon (RC), are the main outcomes of the geochemical analysis by Rock Eval pyrolysis. Using these parameters, other indices can be calculated such as: Hydrogen Index (S2 × 100/TOC), Oxygen Index (S3 × 100/TOC), Production Index (S1/S1 + S2) and S1 + S2.

The Bakken Formation shales have a very high concentration of the total organic carbon (TOC) range from 5 to 20%, with an average of 11.3% across the basin (Webster 1984). TOC measures the quantity of the dispersed organic matter in the rock. The average TOC for the Bakken Shales makes it to be considered as a "very good" source rock from the richness point of view (TOC > 2%; Peters 1986). The TOC (wt%) amount decreases in source rocks as hydrocarbons are generated and expelled (Daly and Edman 1987; Dembicki 2016). The TOC amount has not a uniform distribution across the Williston Basin. The intermediate parts of the basin have the highest concentration of TOC (∼17 wt%) and upper and lower Bakken shales are richer in organic matter whereas, the lowest concentration of TOC could be found along the eastern margin of the basin in the North Dakota and the Bakken shale is relatively organic-lean (>10 wt% of TOC) which probably caused by terrigenous sediments entrance from land and lead to organic matters dilution. Bakken shales contains moderate levels of organic richness (TOC amounts between 13 and 17 wt%) in the central part and eastern Montana area of the basin. The most immature organic matters are located in the Canadian part of the basin with average TOC 20 wt% (Jin and Sonnenberg 2013). Recent evaluation methods consider the

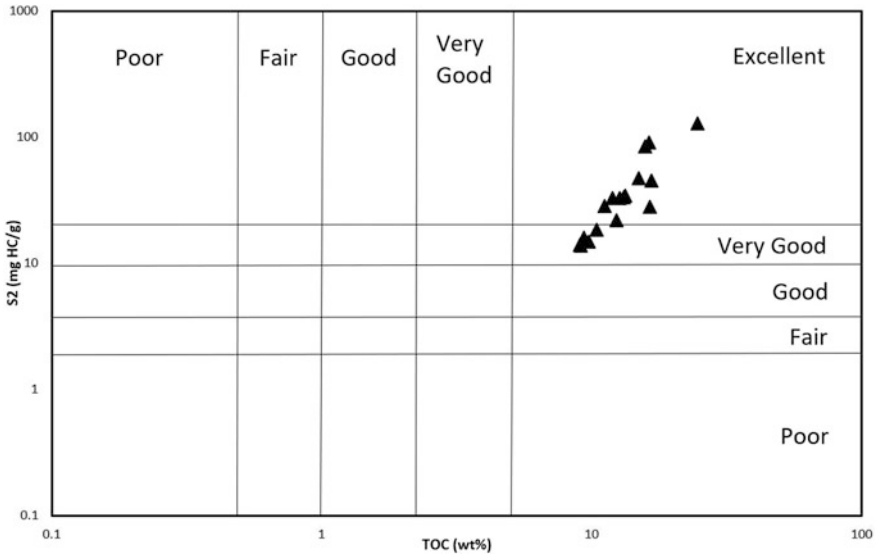

Fig. 1.4 S_2 versus TOC for source rock quality identification for some of the samples from the Bakken shales, from Peters (1986), Abarghani et al. (2018)

S_2 parameter as the principal source richness indicator. Additionally, the S_2 parameter, when in combination with TOC in a cross-plot, provides valuable data for-source rock quality interpretation (Dembicki 2016) (Fig. 1.4).

It should be mentioned that rating the source rock by using cross-plots provides only a general overview of the quality of source rocks and their potential to generate hydrocarbons. Therefore, these results should be confirmed by thermal maturity data and other analytical methods including organic petrography using reflected and transmitted light microscopy (Jackson et al. 1980; Saberi et al. 2016; Dembicki 2016) (Fig. 1.5).

Various methods have been suggested to determine the source rock maturity. Bakken shales maturity has been investigated using different techniques such as Rock-Eval pyrolysis derived thermal maturity data and also by using organic petrology and vitrinite reflectance measurement. Webster (1984) suggests the average threshold of oil generation to occur at 9000 ft and the average threshold of intense oil generation at 10,000 ft and deeper for Bakken Formation. There is no uniform relationship between maturity and depth across the Williston basin. This nonuniformity probably could be explained by different rates of heat flow in various parts of the basin in the geologic history of the basin (Webster 1984).

Jin and Sonnenberg (2013) have shown a meaningful threshold between Tmax and Production Index (PI) in the Bakken shales based on Rock-Eval derived data. Below 425 °C, PI values of Bakken shales are well below 0.08 but with increasing Tmax up to 430 °C and above it, the averaged PI values reach 0.08 and continue to increase up to ~0.4, until Tmax reaches above ~445 °C.

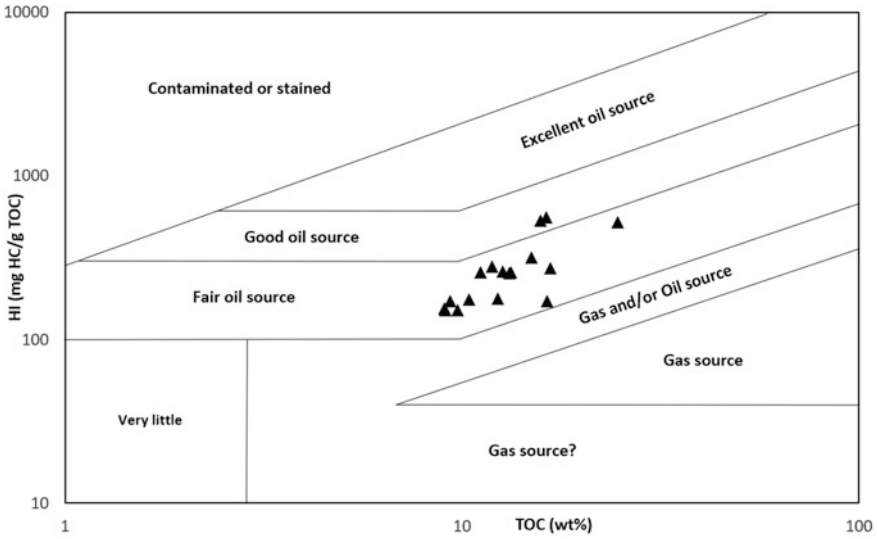

Fig. 1.5 HI versus TOC for source rock quality identification for some of the samples from the Bakken shales Abarghani et al. (2018)

Kerogens of the Bakken Formation source rock is mostly consisting of the amorphous organic matter which is assumed to have algal origin (Powell et al. 1982; Webster 1984). Numerous studies on kerogen typing (e.g. Jin and Sonnenberg 2013; Liu et al. 2017; Khatibi et al. 2018) show that the kerogen type II is the most abundant constituents of the Bakken shales organic matters, however, there is a minor contribution of Kerogens type I and III. Petrographic studies also revealed that most of the organic matter in the Bakken Formation consists of amorphous kerogen under transmitted white light. Additionally, whole-rock microscopic analysis under reflected white and UV light has shown the occurrence of the oil-prone marine kerogen type II of planktonic algal origin (Barker and Price 1985; LeFever 1991; Stasiuk et al. 1991). One way to determine kerogen types is using Rock-Eval derived data and geochemical cross-plots such as HI versus Tmax or S_2 versus TOC (Figs. 1.6, 1.7).

1.2.4 Organic Petrography

Recent organic petrography study in incident light microscopy, polished epoxy-mounted samples shows that the Bakken Upper and Lower shales are mainly consist of primary bitumen, lower-reflecting hydrogen rich bitumen, granular bitumen, amber colored liquid bitumen accumulation, amber-colored bitumen accumulations which are probably generated from algal matter, matrix bituminite, Alginite, Liptodetrinite, Inertinte and minor Zooclast-like abundant large and loose

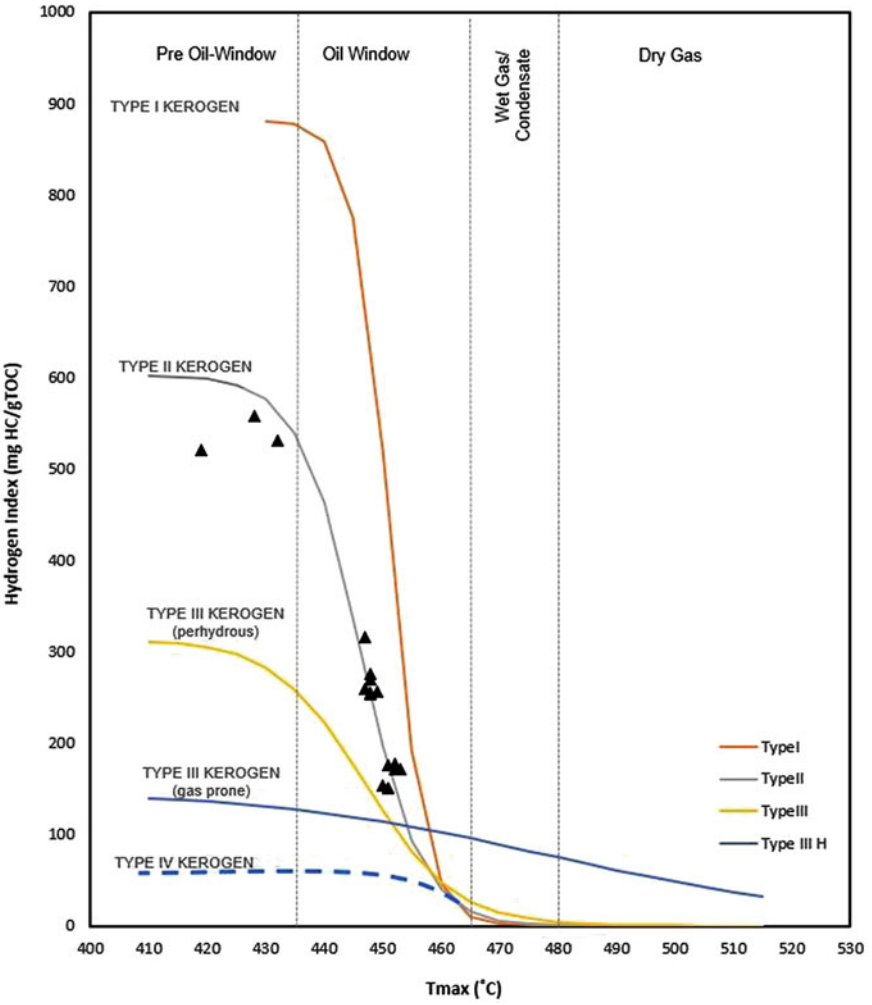

Fig. 1.6 HI versus Tmax for kerogen type identification for some of the samples from the Bakken shales Abarghani et al. (2018)

organic grains Alginite were observed to have dull-yellow fluorescence color under UV light. These findings show that the organic matter is thermally mature and in the middle stage of the oil window. In mature samples, a mean VR_o, ran of 0.88–1.01% measured on some samples from the Bakken Formation. This VR_o values, together with a dull-yellow to light-orange fluorescence color observed for Alginite under UV light, shows that the organic matter is thermally mature and in the middle and early upper stage of the oil window. In the other hand, immature samples mostly

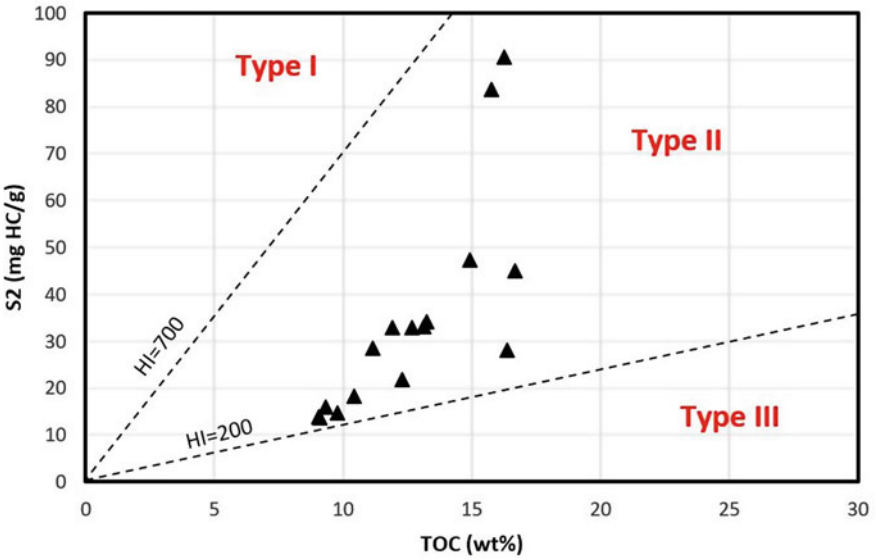

Fig. 1.7 S_2 versus TOC for kerogen type identification for some of the samples from the Bakken shales, from Langford and Blanc-Valleron (1990), Abarghani et al. (2018)

consist of solid bitumen, prasinophyte (blue-green) alginite, unicellular marine alginite (Tasmanites), sporinite, granular macrinite, amorphinte, liptinite, and shell fragments (Figs. 1.8, 1.9).

In certain periods of Earth's history, there were circumstances that deep oceans became oxygen depleted. These particular periods are called "Oceanic anoxic events" or OAE (Meyer and Kump 2008). In the absence of oxygen in an anoxic environment, the level of hydrogen sulfide concentration increased as a result of anaerobic microbial activities. In such conditions, high concentrations of organic matter within the rock matrix occur. In many OAEs the continuation of these conditions led to the creation of an euxinic state, which is characterized by various factors such as high degree of pyritization (Raiswell et al. 1988), pyrite narrower size distribution (Wignall and Newton 2003; Nielsen and Shen 2004), and strong enrichment in Mo, U, V, and Zn (Algeo and Maynard 2004).

Fig. 1.8 Photomicrographs of the Bakken Shale Members: **a** Bitumen (Bit) with Ro of 0.92%. *Qz* Quartz; **b** Bitumen (Bit) whose mean Ro is 1.04%; **c** A thick band of micrinite (Mic) showing slight granularity. Mean *Ro* 0.0.55%; **d** Inertinite (Int), **e** Sporinite (Sp) with yellow fluorescence in the outer part and dull-yellow fluorescence in the center. The spore shows surface punctation; **f** Liptinite (Lip), likely algal, having dull-yellow fluorescence; **g** Granular micrinite (Mic) with Ro of 0.28%, Note the fluorescing amorphinite (Fl Amo) or matrix bituminite; **h** A small oil-prone marine Tasmanites telalginite (Alg) exhibiting golden-yellow fluorescence color; **i** Highly oil-prone thick-walled Tasmanites telalginite (Alg) having golden-yellow fluorescence. All photomicrograohs were taken using a 50X oil immersion objective. UV light parameters were as follows: Excitation filter was at 465 nm; combined dichroic and barrier filters have a cut at 515 nm, Abarghani et al. (2018) ►

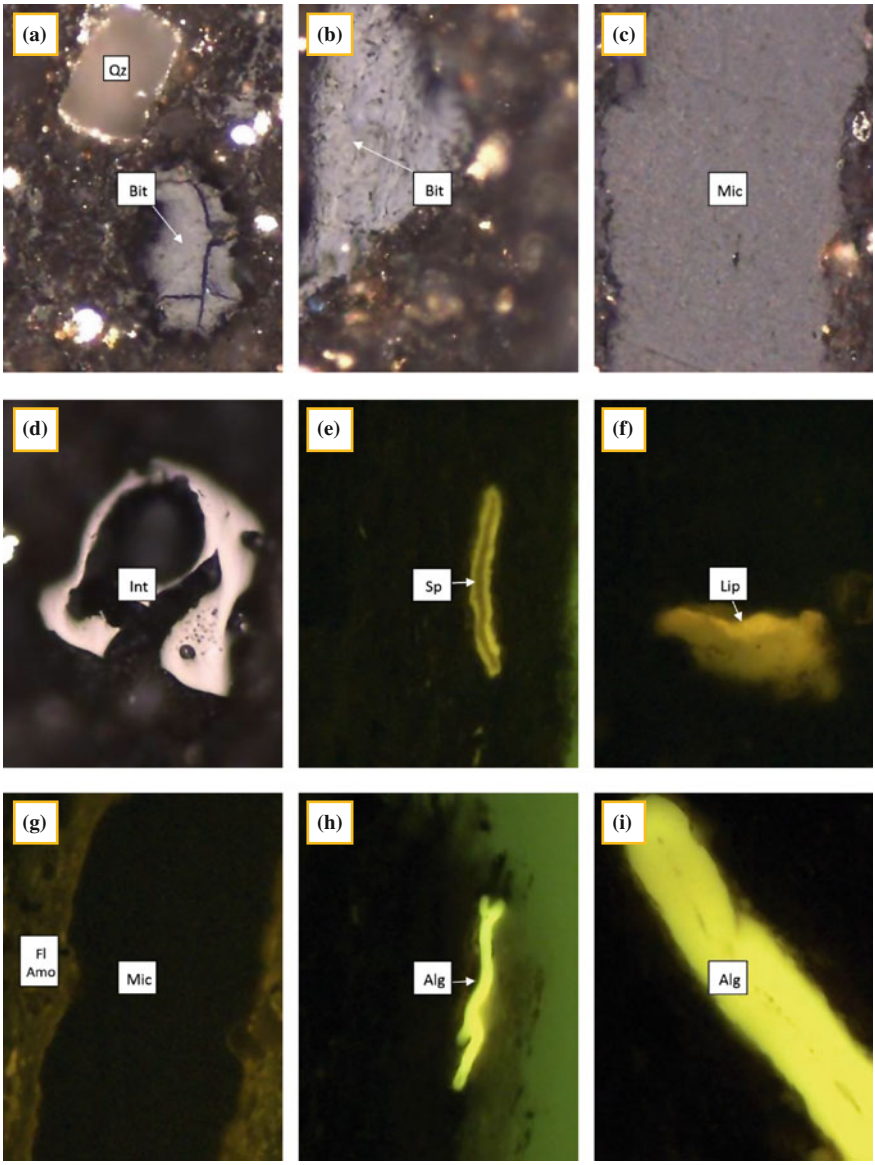

The Kellwasser anoxic oceanic event is known as one of the most widespread evidences for OAEs and basinal euxinia and is reported to have taken place from the Late Devonian and Early Mississippian (Meyer and Kump 2008). Devonian-Mississippian New Albany shales (Ingall et al. 1993), Kellwasser

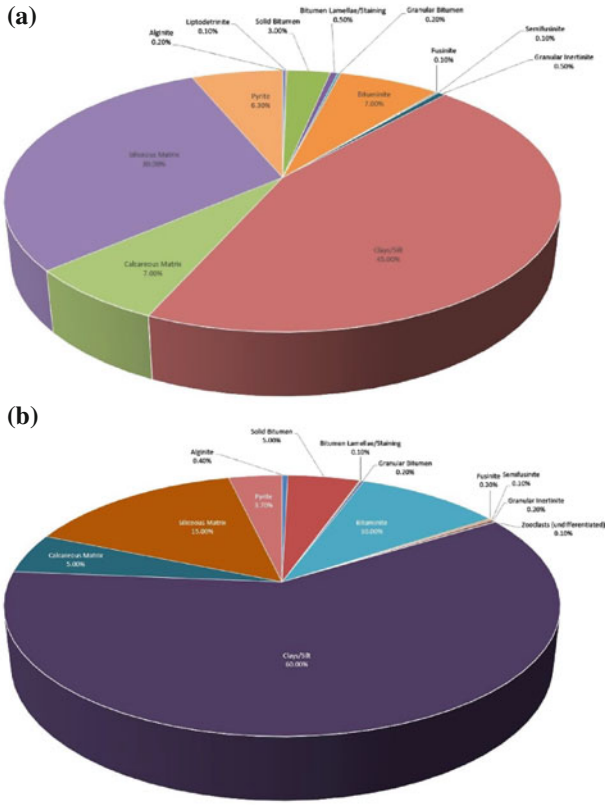

Fig. 1.9 2Pie-diagrams for a Sample from Upper Bakken (**a**) and a Sample from Lower Bakken (**b**) illustrating the composition of each sample , Abarghani et al. (2018).

horizons in the black shales (Frasnian/Famenian) from New York State (Murphy et al. 2000), Black shales from the Illinois and Michigan basins (Brown and Kenig 2004), the classic Frasnian/Famennian Kellwasser events of the Holy Cross Mountains of Poland (Bond et al. 2004) and the lower Mississippian Sunbury Shale of Kentucky (Rimmer 2004) are few examples of this anoxic oceanic event. The reason for this anoxic state is determined to be the thermal stratification which is perpetuated by anoxic productivity feedbacks (Meyer and Kump 2008). The Bakken Formation shales, with very high concentration of organic matter, very high degree of pyritization, the presence of pyrite framboidal shape and narrower size distribution, strong enrichment in Mo, V, and Zn, as well as petrographic evidences could be linked to the remarkable anoxic/euxinic conditions that characterized the Late Devonian (latest Frasnian) and Early Mississippian Kellwasser oceanic anoxic events.

References

Abarghani A, Ostadhassan M, Gentzis T, Carvajal-Ortiz H, Bubach B (2018) Organofacies study of the Bakken source rock in North Dakota, USA, based on organic petrology and geochemistry. Int J Coal Geol 188:79–93

Algeo TJ, Maynard JB (2004) Trace-element behavior and redox facies in core shales of Upper Pennsylvanian Kansas-type cyclothems. Chem Geol 206:289–318

Barker LC, Price CE (1985) Suppression of vitrinite reflectance in amorphous rich kerogen—a major unrecognized problem. J Pet Geol 8:59–84

Bond D, Wignall PB, Racki G (2004) Extent and duration of marine anoxia during the Frasnian-Famennian (Late Devonian) mass extinction in Poland, Germany, Austria and France. Geol Mag 141:173–193

Bordenave ML (1993) Applied petroleum geochemistry. Technip Paris

Brown TC, Kenig F (2004) Water column structure during deposition of Middle Devonian-Lower Mississippian black and green/gray shales of the Illinois and Michigan Basins: a biomarker approach. Palaeogeogr Palaeoclimatol Palaeoecol 215:59–85

Burwood R, De Witte S, Mycke B, Paulet J (1995) Petroleum geochemical characterization of the lower Congo Coastal Basin Bucomazi formation. Petroleum Source Rocks 235–263

Daly AR, Edman JD (1987) Loss of organic carbon from source rocks during thermal maturation. AAPG Bull 71

Dembicki H (2016) Practical petroleum geochemistry for exploration and production. Elsevier

Dyman TS, Palacas JG, Tysdal RG, Perry W Jr, Pawlewicz MJ (1996) Source rock potential of middle cretaceous rocks in southwestern Montana. AAPG Bull 80:1177–1183

Epistalié J, Deroo G, Marquis F (1985) La pyrolyse rock éval et ses applications. Rev Inst Fr Pétr 40:563–579

Ettensohn FR, Barron LS (1981) Depositional model for the Devonian-Mississippian black-shale sequence of North America: a tectono-climatic approach. Kentucky University, Lexington (USA). Department of Geology

Hayes MD (1985) Conodonts of the Bakken formation (Devonian and Mississippian), Williston Basin, North Dakota. The Mountain Geologist

Hunt M (1996) Petroleum geochemistry and geology. WH Freeman and company

Ingall ED, Bustin R, Van Cappellen P (1993) Influence of water column anoxia on the burial and preservation of carbon and phosphorus in marine shales. Geochim Cosmochim Acta 57:303–316

Jackson K, Hawkins P, Bennett A (1980) Regional facies and geochemical evaluation of the southern Denison Trough, Queensland. APPEA J 20:143–158

Jin H, Sonnenbergy SA (2013) Characterization for source rock potential of the Bakken Shales in the Williston Basin, North Dakota and Montana. In: Unconventional Resources Technology Conference (URTEC)

Khatibi S, Ostadhassan M, Tuschel D, Gentzis T, Bubach B, Carvajal-Ortiz H (2018) Raman spectroscopy to study thermal maturity and elastic modulus of kerogen. Int J Coal Geol 185:103–118

Lafargue E, Marquis F, Pillot D (1998) Rock-Eval 6 applications in hydrocarbon exploration, production, and soil contamination studies. Revue de l'institut français du pétrole 53:421–437

Langford F, Blanc-Valleron M-M (1990) Interpreting Rock-Eval pyrolysis data using graphs of pyrolizable hydrocarbons versus total organic carbon (1). AAPG Bull 74:799–804

LeFever JA (1991) History of oil production from the Bakken Formation, North Dakota

LeFever J (2008) Isopach of the Bakken Formation: North Dakota geological survey geologic investigations 59. Bakken map series, scale 1, pp 1–5

LeFever JA, Martiniuk CD, Dancsok EF, Mahnic PA (1991) Petroleum potential of the middle member, Bakken Formation, Williston Basin. In: Williston Basin symposium

Lineback J, Davidson M (1982) The Williston Basin-sediment-starved during the Early Mississippian. In: Williston Basin symposium

Liu K, Ostadhassan M, Gentzis T, Carvajal-Ortiz H, Bubach B (2017) Characterization of geochemical properties and microstructures of the Bakken Shale in North Dakota. Int J Coal Geol

Meissner FF (1991) Petroleum geology of the Bakken Formation Williston Basin, North Dakota and Montana

Meyer KM, Kump LR (2008) Oceanic euxinia in Earth history: causes and consequences. Annu Rev Earth Planet Sci 36:251–288

Pollastro RM, Cook TA, Roberts LN et al (2008) Assessment of undiscovered oil resources in the Devonian-Mississippian Bakken Formation, Williston Basin Province, Montana and North Dakota, (No 2008–3021). Geol Surv (US)

Webster RL (1984) Petroleum source rocks and stratigraphy of the Bakken Formation in North Dakota. In: RMAG guidebook, Williston Basin, anatomy of a Cratonic Oil Province, pp 268–285

Wignall PB, Newton R (2003) Contrasting deep-water records from the Upper Permian and Lower Triassic of South Tibet and British Columbia: evidence for a diachronous mass extinction. Palaios 18:153–167

Chapter 2
Pore Structures

Abstract Pore structures play a very critical role in the petroleum industry, which controls the capacity of oil and gas storage in the reservoir (Anovitz and Cole in Rev Miner Geochem 80(1):61–164, 2015). Pore with different properties such as pore size and pore shape can impact the physical, mechanical and chemical properties of the rocks including strength, elastic modulus, permeability, and conductivity (Boadu in J Appl Geophys 44(2–3):103–113, 2000; Sanyal et al. in Chem Eng Sci 61(2):307–315, 2006; Wang et al. in J Appl Geophys 86:70–81, 2012). Therefore, characterization and quantification of the pore structures appear to be crucial for reservoir development. The boom of the unconventional resources in the recent decade brought the attention of the many researchers' attention. Shale oil formation is one of the typical unconventional reservoirs and the understanding of these kinds of formation is still limited. In comparison to the conventional reservoirs such as sandstone or limestone, the pore structures in shale reservoirs are more complex due to the abundance of the nano-pores. In this chapter, various kinds of methods are introduced and applied to analyze the micro structures of the shale oil formation.

2.1 Methods

2.1.1 SEM

SEM has been one of the most useful tools to study the pore microstructures. High-resolution SEM images can discriminate between solid matrix and pores due to the different gray level pixels and have been the main tool to analyze the pore structures of the porous medium (Bogner et al. 2007; Joos et al. 2011). For the shale oil formation, such as the Bakken shale, Small chips that are parallel to the bedding from the cores were taken. Samples were trimmed down to the 0.5 cm square cube, using a trim saw. Cube is then smoothed out on all faces by hand with a Buehler polishing wheel using 600-grit silicon carbide grinding paper. The samples are mounted to the ion mill sample holder using carbon tape and placed in the

M. Ostadhassan et al., *Fine Scale Characterization of Shale Reservoirs*,
SpringerBriefs in Petroleum Geoscience & Engineering,
https://doi.org/10.1007/978-3-319-76087-2_2

Leica EM TIC 3X argon ion mill. After that, all samples were milled at an accelerating voltage of 8 kV, with gun current at 3 mA for 8 h. Finally, samples were removed from the ion mill's sample holder and mounted on a clean SEM stub using carbon paint. A high-quality image is required for accurate segmentation and subsequent quantification analysis.

2.1.1.1 SEM Image Processing

After we had derived the gray scale image from the FESEM, we segmented the images by converting the original image into the binary image where white pixels represent pores, and black pixels exhibit the solid matrix. The porosity can be calculated as the ratio of the area of white pixels to the whole scan area. Finding a suitable threshold accurately to segment the gray level images can affect the analysis results directly. Only under the circumstances that the segmentation algorithm which is precise and reproducible, we can get the meaningful quantitative data which can be used to formulate the microstructure properties relationships. Based on the comparison made by Wong et al. (2006), we applied critical overflow point technique, which is related to the inflection of the cumulative brightness histogram to find the accurate upper threshold gray level for porosity.

After we had determined the upper threshold value, we segmented the image and converted it into binary format. Then Image J software, which is a commonly used image analysis software, was used to study the pore structures.

2.1.1.2 Pore Size

We used a popular image processing software to analyze the pore structures of the segmented area and applied box plot to compare the pore sizes of the four samples.

Two shape parameters (Aspect Ratio and Circularity) were utilized to describe the pore shape information of the rocks (Liu and Ostadhassan 2017a, b, c).

The aspect ratio of the image describes the proportional relationships between its width and height. For the pore structure analysis, the aspect ratio can determine the shape of the pores which is defined as Takashimizu and Iiyoshi (2016):

$$AR = \frac{x_{F\max}}{x_{F\min}} \tag{2.1}$$

where $x_{F\max}$ and $x_{F\min}$ are the major and the minor axis of the approximate ellipse, respectively. Therefore, if the aspect ratio is approaching 1, the pore is approximate to a perfect circle while a decreasing aspect ratio can be translated to the increased deformation of the pores.

Circularity is defined as the degree to which the particle is similar to a circle by taking into consideration of the smoothness of the perimeter. Circularity is a

dimensionless value which can be described using the following equation (Cox 1927):

$$C = 4\pi \frac{A_I}{P_I^2} \tag{2.2}$$

where A_I and P_I are the pore area and the perimeter of the pore, respectively.

The circularity value ranges from 0 to 1. If the circularity is close to 1, the pore is approximate to a perfect round and smooth circle.

2.1.1.3 Fractal Dimension

The main attraction of the fractal geometry originates from its strong ability to describe the irregular or fragmented shape of natural features as well as other complex objects that traditional Euclidean geometry fails to characterize (Lopes and Betrouni 2009). The key parameter in fractal geometry is the fractal dimension, D, which can offer a systematic approach to quantify irregular patterns. Among all fractal dimension computing methods, the box-counting method which was defined by Russel et al. (1980), is the most popular method to calculate the fractal dimension (Lopes and Betrouni 2009).

The Box-counting technique is used to get the scaling properties of 2-D fractal objects by covering the 2-D image with a range of boxes of size ε and counting the number of boxes N. Each box contains at least one pixel representing objects under study. This procedure is then repeated for a range of ε values. Then we get the different box counting numbers N covering the pore space at various grid size ε. Finally, we calculate the fractal dimension based on the following equation:

$$D_0 = \lim_{\varepsilon \to 0} \frac{\log N_{(\varepsilon)}}{\log(1/\varepsilon)} \tag{2.3}$$

For the 2D image, the fractal dimension D ranges from 1 to 2.

2.1.1.4 Multifractal Analysis

The significant interest in production from unconventional plays including oil and gas shales has called for several studies to better characterize such complex resources. Unlike the homogeneous pore structures in sandstones, the pores in shale formations are always heterogeneous. The heterogeneities which can be identified over the various scales from nanometers to meters will result in different properties of the rocks even at the same porosity (Vasseur et al. 2015). The impact of the heterogeneity of the pore structures on shale's properties needs to be understood in order for economic production. For the SEM images, multifractal and lacunarity theory can be used for the pore structure heterogeneity analysis.

The single fractal dimension which is widely used to study the porous structures cannot describe the complex structures with subsets of regions having various properties. However, the multifractal theory, which considers the amount of mass inside each box, appears to be able to characterize the pore structure properties.

For the measurement of fractal dimension, the number $N(\varepsilon)$ of features of certain size ε scale as Chhabra and Jensen (1989), Mendoza et al. (2010)

$$N(\varepsilon) \sim \varepsilon^{-D_0}, \tag{2.4}$$

where D_0 is called the fractal dimension, which is frequently be expressed as:

$$D_0 = \lim_{\varepsilon \to 0} \frac{\log N(\varepsilon)}{\log \frac{1}{\varepsilon}}, \tag{2.5}$$

D_0 can be derived by counting the number of boxes with various sizes to cover the object under investigation and then estimating the slope value from the log-log plot.

Then, the following equation will be applied to quantify the local densities by estimating the mass probability in the *i*th box:

$$p_i(\varepsilon) = N_i(\varepsilon)/N_T, \tag{2.6}$$

where $N_i(\varepsilon)$ is the number of pixels containing mass in the *i*th box and N_T is the total mass of the system. Thus the probabilities in the *i*th box $P_i(\varepsilon)$ can be written as the following equation:

$$P_i(\varepsilon) \sim \varepsilon^{\alpha_i}, \tag{2.7}$$

where α_i is the singularity strength which can characterize the density in the *i*th box (Feder 1988; Halsey et al. 1986).

For multifractal measurements, a probability distribution is measured as:

$$\sum_i [p_i(\varepsilon)]^q \sim \varepsilon^{\tau(q)}, \tag{2.8}$$

where q is the exponent expressing the fractal properties in different scales of the object. τ_q can be defined as:

$$\tau(q) = \lim_{r \to 0} \left[\ln \left(\sum_i P_i(\varepsilon)^q \right] / \ln(1/\varepsilon), \right. \tag{2.9}$$

and the generalized dimension D_q which is related with q can be expressed as Halsey et al. (1986):

$$D_q = \tau(q)/(q-1), \tag{2.10}$$

Also, we can use the relationship between parameters of $f(\alpha)$ versus α to calculate the multifractal spectra:

$$N(\alpha) \sim \varepsilon^{-f(\alpha)}, \tag{2.11}$$

where $N(\alpha)$ is the number of boxes for which probability $P_i(\varepsilon)$ has singularity strengths between α and $\alpha + d\alpha$. $f(\alpha)$ contains the same information of generalized dimensions D_q and can be defined as Halsey et al. (1986), Chhabra and Jensen (1989):

$$f(\alpha(q)) = q\alpha(q) - \tau(q), \tag{2.12}$$

where $\alpha(q)$ can be defined as:

$$\alpha(q) = d\tau(q)/dq. \tag{2.13}$$

2.1.1.5 Lacunarity Analysis

In order to quantify the heterogeneities of the pore structures of the sample, lacunarity was introduced to solve this kind of problem. Lacunarity which was introduced by Mandelbrot (1983) is a counterpart of the fractal dimension which can be used to describe the size distributions. Lacunarity measures the deviation of a geometric object that has translational invariance and can be thought as a measure of gapiness of the geometric structure. If the structure has more wide or large gaps, the structure has higher lacunarity value.

The gliding-box counting algorithm was applied to calculate the lacunarity in this paper by utilizing a moving window (Smith et al. 1996; Plotnick et al. 1993). A box of size r is positioned at the upper left corner of the image and the number of the occupied sites can be regarded as the box mass. Then the box is moved one column to the right and the box mass is again counted. This process is repeated over all rows and columns of the image producing a frequency distribution, mass M, of the region that we studied. The number of the boxes with the size r containing a mass (M) of the image was designated by $n(M, r)$, with the total number of boxes counted designated by $N(r)$. If the image size is P, then:

$$N(r) = (P - r + 1)^2 \tag{2.14}$$

Then the probability distribution $Q(M, r)$ can be calculated by the frequency distribution (Backes 2013; Plotnick et al. 1993):

$$Q(M,r) = \frac{n(M,r)}{N(r)} \tag{2.15}$$

The first and second moments of this distribution are defined by:

$$A^{(1)} = \Sigma MQ(M,r) \tag{2.16}$$

$$A^{(2)} = \Sigma M^2 Q(M,r) \tag{2.17}$$

Then the lacunarity of this box size is defined as:

$$\Lambda(r) = \frac{A^{(2)}}{(A^{(1)})^2} \tag{2.18}$$

The statistical behavior of $\Lambda(r)$ can be understood by recognizing that:

$$A^{(1)} = u(r) \tag{2.19}$$

$$A^{(2)} = u(r)^2 + \sigma^2(r) \tag{2.20}$$

Finally, we can get (Allain and Cloitre 1991; Malhi and Román-Cuesta 2008)

$$\Lambda(r) = \frac{\sigma^2(r)}{u(r)^2} + 1 \tag{2.21}$$

Here $\sigma^2(r)$ is the variance of the number of sites per box and $u(r)$ is the mean value of the number sites per box. Then we can repeat this process with different box size and get the set of the lacunarity values at various box size.

2.1.2 AFM (Atomic Force Microscopy)

AFM is derived from the principles from the scanning tunneling microscope and the stylus profilometer (Binnig et al. 1986) and a quite new technology in the big characterization family. Compared with other types of microscopy such as SEM, AFM has a high ability in characterizing the surface features at nanometer and angstrom scales and can produce 3D topography image which can be used to study the depth, roughness and many other things (Bruening and Cohen 2005). AFM is now widely used in biology and material science research but still rarely used in petroleum engineering (Javadpour 2009; Javadpour et al. 2012; Liu et al. 2016a).

The working mechanism of the AFM can be described as below: The cantilever is held at one end while free on the other end, as the tip approaches or retracts from the surface, the cantilever is moved vertically due to the changes of the interactive

force. Then the deflected laser beam can be detected and the related signal can be transmitted to data-processing equipment. Contact mode and tapping mode have become the two most used methods for imaging. In contact mode, the deflection of the cantilever is kept constant. The drawback of this mode is that the dragging motion of the tip can cause some potential damage to both sample and probe and will influence the accuracy of the image. This mode is quite suitable for hard surface samples. In order to overcome the shortages of the contact mode, tapping mode was developed which is implemented in ambient air by oscillating the cantilever assembly at or near the cantilever's resonance frequency using a piezoelectric crystal.

2.1.3 Gas Adsorption

Low pressure adsorption measurement which has been extensively used in the surface chemistry analysis for characterization of porous medium nowadays has been applied to quantify the pore structures of the shale formation (Kuila and Prasad 2013; Cao et al. 2016; Sun et al. 2016). Nitrogen is the most widely used gas for the adsorption analysis. One limitation of nitrogen, which originates from the gas molecule and pore throat sizes, makes it inaccurate in characterizing the micro-pore size range. CO_2 adsorption was then used to analyze the micro-pores since it works well in the media containing pores less than 2 nm (Tang et al. 2003). The combination of nitrogen and CO_2 can give us information about the whole pore size distributions less than 200 nm. Need to add some more explanation here about the gas adsorption.

Prior to adsorption measurement, the samples were degassed for at least 8 h at 110 °C to remove moisture and volatile in the sample pores. Low-pressure nitrogen was measured on a Micromeritics® Tristar II apparatus at 77 K. Carbon dioxide adsorption was measured on a Micromeritics® Tristar II plus apparatus at 273 K. Gas adsorption volume was measured over the relative equilibrium adsorption pressure (P/P_0) range of 0.01–0.99, where P is the gas vapor pressure in the system and P_0 is the saturation pressure of nitrogen (Liu et al. 2017).

The gas adsorption experimental data was used to quantify the amount of the gas adsorbed at different relative pressures (P/P_0) where P_0 is the saturation pressure of the absorbent and the P is gas vapour pressure in the system.

For nitrogen adsorption, the total volume can be derived from the total amount of vapor adsorbed at the relative pressure (P/P_0) which is close to 1, assuming that the pores are filled with the liquid adsorbate. The average pore radius of the sample can be calculated as:

$$r_p = \frac{2V}{S}, \tag{2.22}$$

where V is the total amount of the nitrogen adsorbed, and S is the surface area derived from the BET (Brunauer, Emmett and Teller) theory (Labani et al. 2013).

To calculate the pore size distribution (PSD) from the nitrogen adsorption, BJH and DH model cannot give the realistic description of micro-pore filling which can lead to an underestimation of pore sizes for micro pores and even the smaller meso-pores (Ravikovitch et al. 1998). In this study, we applied density functional theory (DFT) molecular model due to its applicability in determining the PSD in micro-pore scale as well as meso-pore scale (Do and Do 2003). The carbon dioxide adsorption data were interpreted using the non-local density functional theory (Amankwah and Schwarz 1995; Fan and Ziegler 1992).

Fractal geometry, proposed by Mandelbrot (1982), has a strong ability to describe the irregular or fragmented shape of natural features as well as other complex objects that traditional Euclidean geometry fails to characterize (Lopes and Betrouni 2009). Fractal dimension (D) is the key parameter in the fractal geometry, which can offer a systematic approach to quantify irregular patterns. For the gas adsorption theory, several fractal models have been developed such as the BET model, fractal FHH model and the thermodynamic model (Avnir and Jaroniec 1989; Cai et al. 2011; Yao et al. 2008). The fractal FHH model which focuses on the capillary condensation region of the fractal surface, has been proven to be the most effective method for analyzing the fractal behavior of porous medium (Yao et al. 2008). FHH model can be described using the following equation:

$$\ln V = Constant + (D - 3)\ln(\ln(1/(P/P_0))) \tag{2.23}$$

where V is the total volume of the adsorption, P is the equilibrium pressure, P_0 is the saturated vapour pressure of the adsorption and D is the fractal dimension.

2.2 Examples and Results

2.2.1 SEM Image Analysis

2.2.1.1 Image Processing

SEM gray image of Sample 1 at the scan size 6.35 × 4.42 μm^2 by the FEI Quanta 650 SEM apparatus (Fig. 2.1a) and analyzed the influence of the threshold value on the pore area. Figure 2.1b represents the pore area under different threshold values (the intensities of the grayscale image) (Liu and Ostadhassan 2017a, b, c).

It can be found from the series of images shown in Fig. 2.1b, that the segmented area (white pixel areas) increases steadily as the threshold value increases. Once the threshold is above 70, a sudden increase in the segmented area is notified due to changes of the beam interaction volume used to capture the boundary (Wong et al. 2006; Goldstein et al. 1981). This phenomenon is analogous to filling up a pore with a fluid. Before the fluid arrives near the edge, the volume filled with the fluid

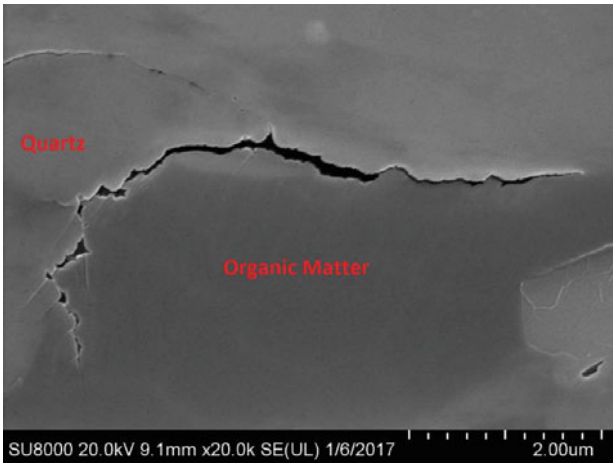

(a) original image

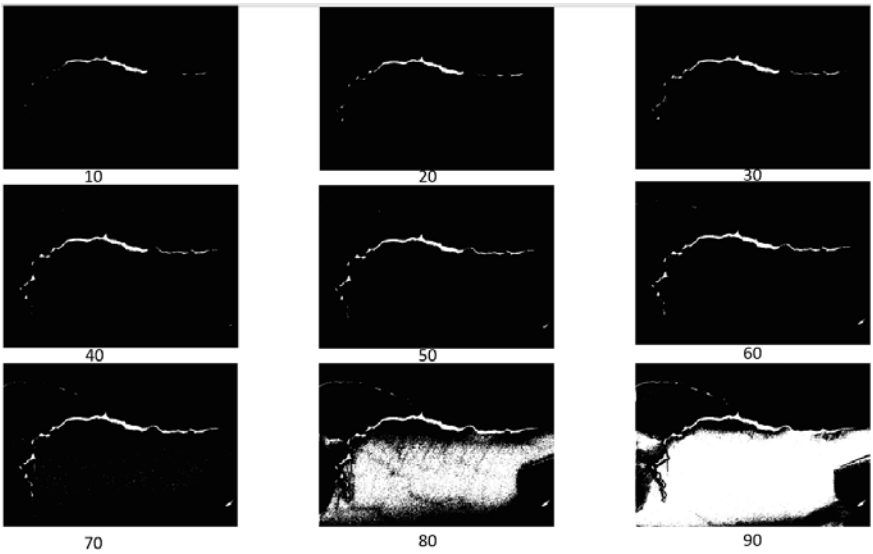

(b) Binary images

Fig. 2.1 The influence of the threshold value on the segmented area (white pixels represent pores; black pixels denote solids)

will increase gradually, once it arrives near the edges, a critical point is reached and the liquid will overflow to the surrounding areas, and this will lead to a sudden increase of the area covered with the fluid. Therefore, the threshold value of

Fig. 2.2a is 74.2 and the segmented pore area of this image under this threshold value are provided in Fig. 2.2b.

Based on the above method, we determined the threshold value of the four samples we analyzed both at high magnification ratio (scan area 21.19 × 14.7 μm^2) and low magnification ratio (scan area 127.15 × 88.11 μm^2) and derived the surface porosity which is summarized in Table 2.1.

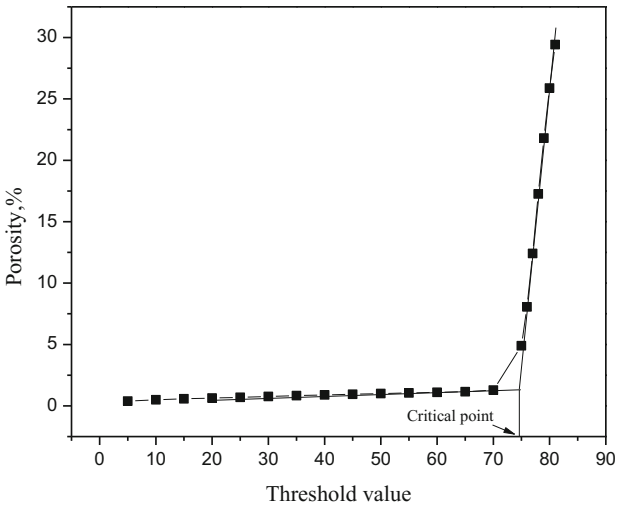

(a) Cumulatively gray scale histogram of Sample 1 (scan size 6.35×4.42 um^2).

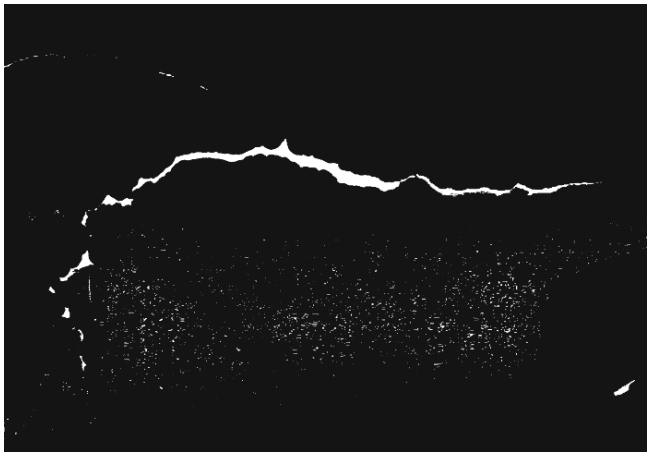

(b) Pores segmented at threshold value 74.2

Fig. 2.2 Application of overflow criteria to determine the threshold level for quantifying porosity

Table 2.1 Information about the pore structures of Bakken formation

	Formation		Pore counts	Pore area (%)	Mean pore size (nm)
Sample 1	Upper Bakken	LM	15,257	6.77	91.55
		HM	11,220	6.47	15.94
Sample 2	Upper Bakken	LM	10,738	4.03	89.31
		HM	5360	5.21	18.04
Sample 3	Middle Bakken	LM	7167	6.34	186.42
		HM	1053	6.96	30.09
Sample 4	Middle Bakken	LM	4532	6.5	211.63
		HM	702	4.046	29.66

Note HM means high magnification ratio (image size 21.19 × 14.7 μm^2) while LM denotes low magnification ratio (image size 127.15 × 88.11 μm^2)

The results showed that surface porosity of all the samples under two different magnifications are in the low range, less than 7%. Both under high and low magnification ratios, Upper Bakken has more pore counts than that of the Middle Bakken Formation. This is because the Upper Bakken has more clay minerals than the Middle Bakken formation. Pores are most abundant in the clay matrix, compared with other mineral matrix (Houben et al. 2014). The pore structures of the same sample derived from the image analysis method show different values (pore counts, porosity and mean pore size values) under different magnification ratios, showing the importance of studying the effect of the magnification ratio on the pore structures.

2.2.1.2 Pore Size Distribution Analysis

Pore Size Distribution (PSD) of each sample under both HM and LM is presented in Fig. 2.3.

Figure 2.3 shows that the pore size distributions of the four samples both under high and low magnification are largely positive skewed, which means that most pores have small pore sizes. Only a few outliers can be found in Fig. 2.4, which illustrates that only a small number of large pores exist in the samples while most pores are at the nanoscale range.

2.2.1.3 Pore Shape Distributions Analysis

We used the aspect ratio and circularity to analyze the pore shape and distributions of the samples. Figure 2.5 shows that the aspect ratio distributions demonstrate positive skewness whereas the circulation distributions show negative skewness.

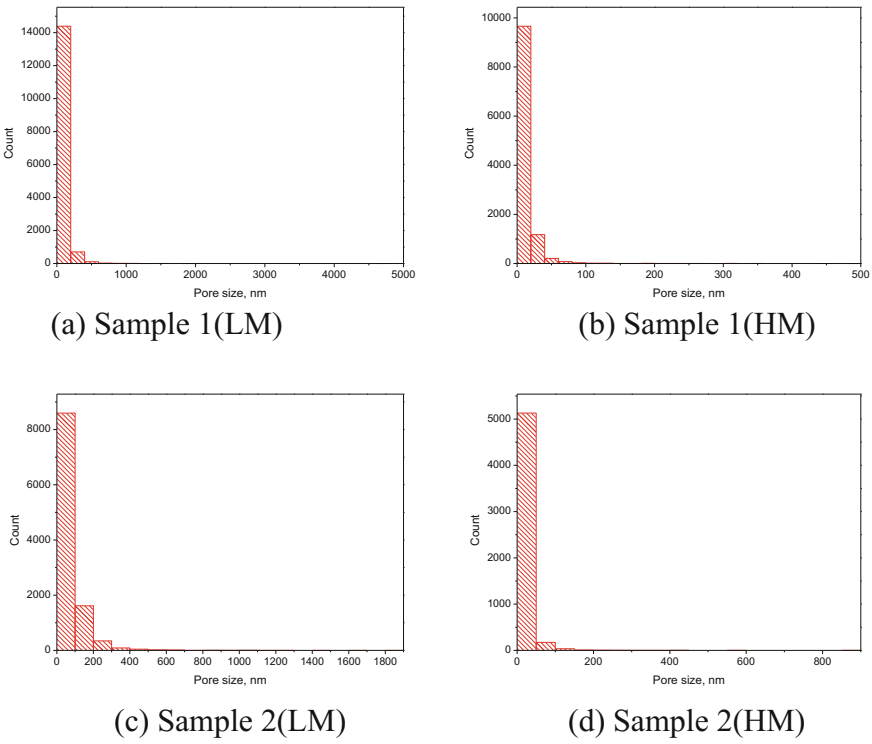

Fig. 2.3 Pore size distributions of four samples

The distribution illustrates that many pores are prone to round pores since they have the small aspect ratios and high circularity values.

Based on further observations of the pores we deduced that if the circularity value was close to 0, the pores were representing micro-cracks, and if the circularity was approaching 1, round and circular pores were abundant. We divided all the pores with different circularity values into three different groups of micro-cracks ($C < 0.2$), intermediate pores (0.2–0.8) and round pores ($C > 0.8$).

We grouped the pores of all the samples both under high and low magnification ratios. Results in Tables 2.2 and 2.3 show that Sample 1 and Sample 2 host more round pores but fewer micro-cracks compared with the pore structures of Sample 3 and Sample 4.

The pore structure analysis of the four samples illustrates that the Upper member has an abundance of smaller round pores than those of the Middle member, which hosts more micro-cracks. This is in agreement with the mineralogical composition of each member. Upper Bakken has more clay minerals (illite) whereas the Middle Bakken consists of more brittle minerals such as dolomite, pyrite, and feldspar, which are believed to have a very strong control over the pore shape and structure (Liu et al. 2016b).

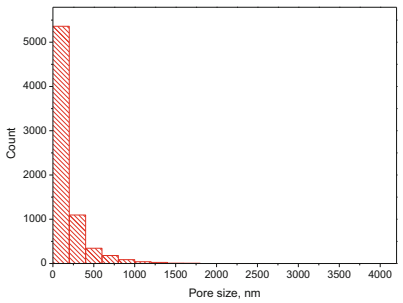

(e) Sample 3(LM)

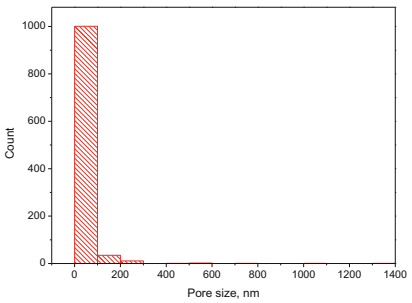

(f) Sample 3(HM)

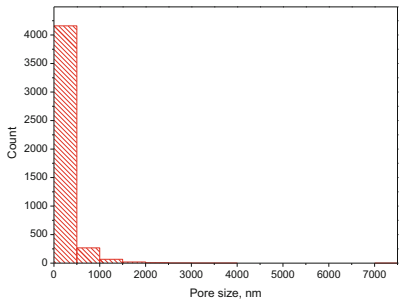

(g) Sample 4(LM)

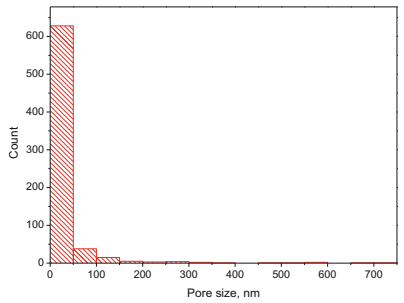

(h) Sample 4(HM)

Fig. 2.3 (continued)

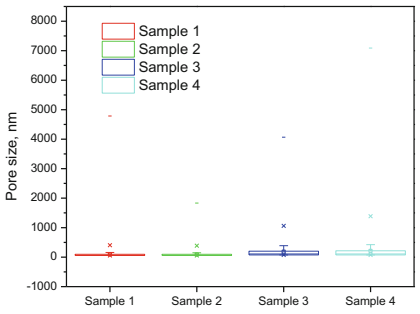

(a) LM

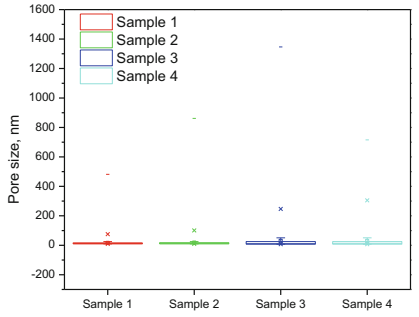

(b) HM

Fig. 2.4 Boxplot of pore area distributions of the four samples

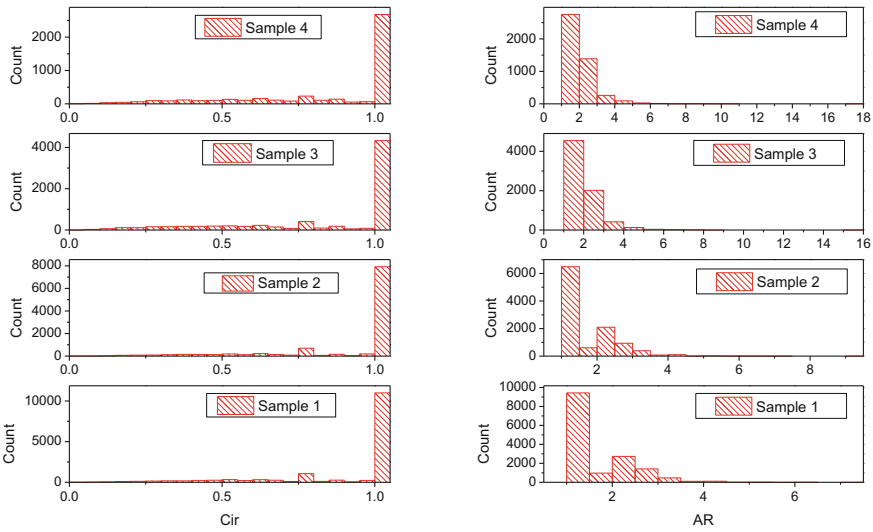

(a) Circularity (LM) (b) Aspect ratio (LM)

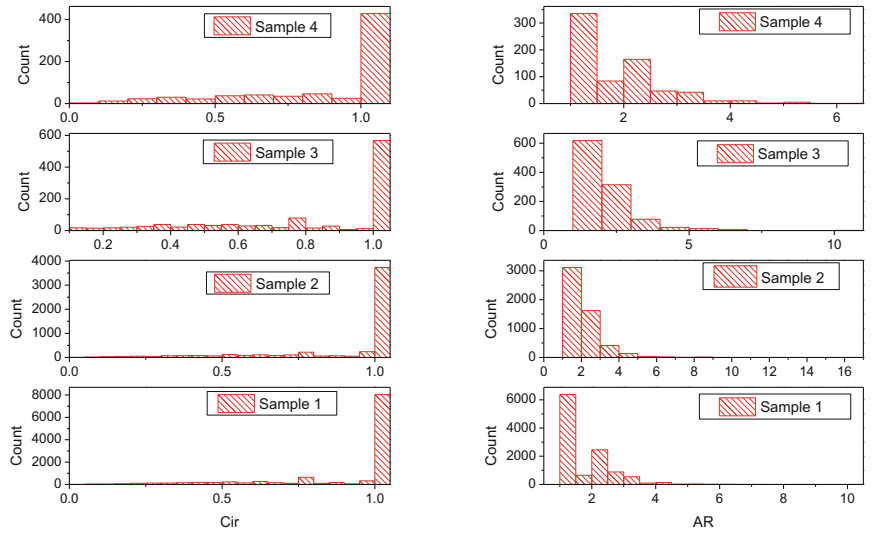

(c) Circularity (HM) (d) Aspect ratio (HM)

Fig. 2.5 Pore shape distributions of the samples

Table 2.2 Ratio of pores with different shapes to the whole scan image area

		Total porosity (%)	Micro-cracks (%)	Intermediate pores (%)	Round pores (%)
Sample 1	LM	6.771	2.283	2.851	1.618
	HM	6.47	2.423	2.732	1.298
Sample 2	LM	4.026	1.027	1.821	1.167
	HM	5.213	1.625	2.853	0.726
Sample 3	LM	6.343	2.542	3.198	0.589
	HM	6.956	5.408	1.455	0.092
Sample 4	LM	6.585	2.908	3.102	0.52
	HM	4.05	2.444	1.492	0.112

Table 2.3 Ratio of pores with various shapes to the total pore area

		Micro-cracks (%)	Intermediate pores (%)	Round pores (%)
Sample 1	LM	33.71732388	42.10604047	24.17663565
	HM	37.44976816	42.22565688	20.32457496
Sample 2	LM	25.50919026	45.23099851	29.25981123
	HM	31.17200000	54.72850000	14.09936697
Sample 3	LM	40.07567397	50.41778338	9.506542645
	HM	77.74583094	20.91719379	1.336975273
Sample 4	LM	44.16097191	47.1070615	8.731966591
	HM	60.34567901	36.83950617	2.814814815

2.2.1.4 Fractal Dimension Determination

Two-dimensional box counting calculations of the pore spaces of the samples have been carried out in the following section. Figure 2.6 shows boxes with different length scale to cover the pore spaces within sample 1 at the scan size $6.35 \times 4.42\ \mu m^2$. Figure 2.7 displays the fractal dimension of this image.

The fitting curve was applied to the data in Fig. 2.7 to correlate an evident linear relationship between $\ln N$ and $\ln \varepsilon$ with the correlation coefficients of higher than 0.99, which indicates that the pore structure of rock samples presents very strong fractal characteristics. Then we calculated the fractal dimension of all the samples. Table 2.4 shows that all the samples under high magnification and low magnification demonstrate fractal characteristics with high correlation coefficients. However, the four samples with different pore structures showed different fractal dimensions. Sample 1 has the highest fractal dimension values both under high magnification and under low magnification, showing that Sample 1 has the most complex pore structures. Under high magnification, Upper Bakken Formation has higher fractal dimension compared with the value of Middle Bakken Formation due to abundant small pores exist in clay minerals appear in the scan image.

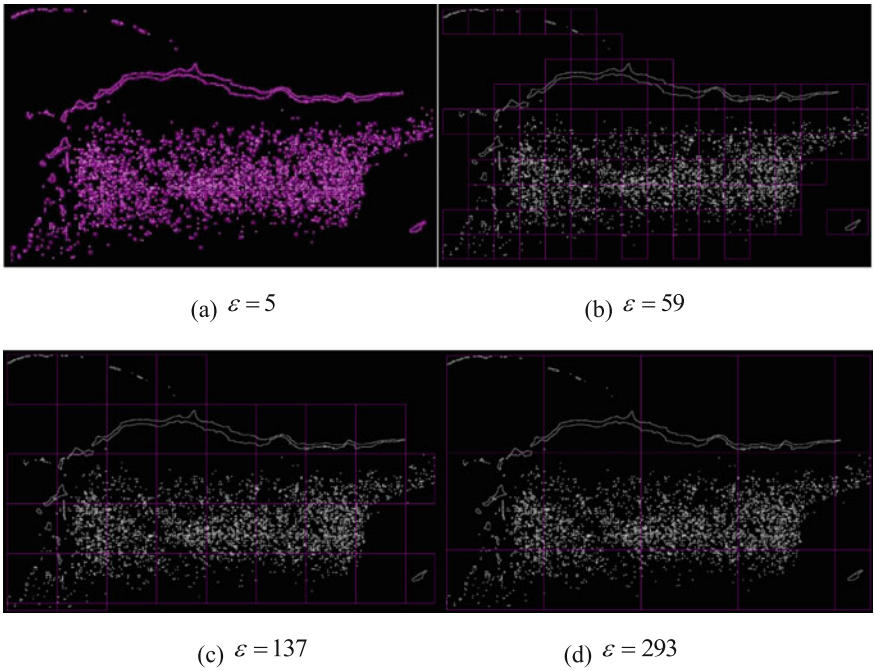

Fig. 2.6 SEM image of Sample 1 divided by grids with different length scale

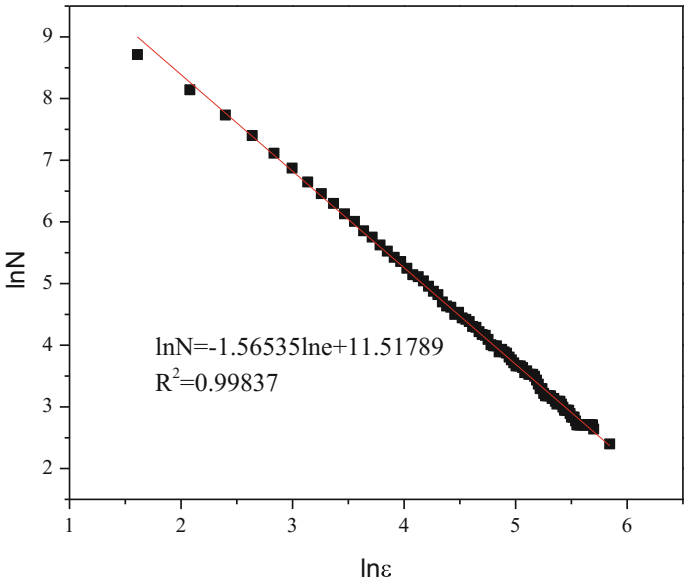

Fig. 2.7 Fractal dimensions of pore structures of sample shown in Fig. 2.6

Table 2.4 Fractal dimension analysis results

		D	R^2
Sample 1	LM	1.81444	0.99806
	HM	1.82341	0.99708
Sample 2	LM	1.75422	0.99685
	HM	1.71802	0.99444
Sample 3	LM	1.79201	0.99604
	HM	1.47195	0.99126
Sample 4	LM	1.73229	0.99211
	HM	1.38407	0.98966

2.2.1.5 Heterogeneity Analysis

Based on the determination of the REA, we segmented all the samples into binary format. Then we did multifractal analysis of all the samples. The mean of generalized dimensions (D_q) versus variable q (between −10 and +10) for the five samples are shown in Fig. 2.8.

Figure 2.8 shows that all samples follow a sigmoid fit and exhibit pronounced decreasing D_q values with increasing q. D_0, D_1 and D_2 are the three parameters that are commonly used for the multifractal analysis. D_0 is called the capacity dimension which provides the average values of the analyzed structure distribution, indicating the complexity of the pore structures. D_1 is called the information dimension and D_2 is the correlation dimension (Li et al. 2012). The values of these parameters for the samples tested in this study are listed in Table 2.5.

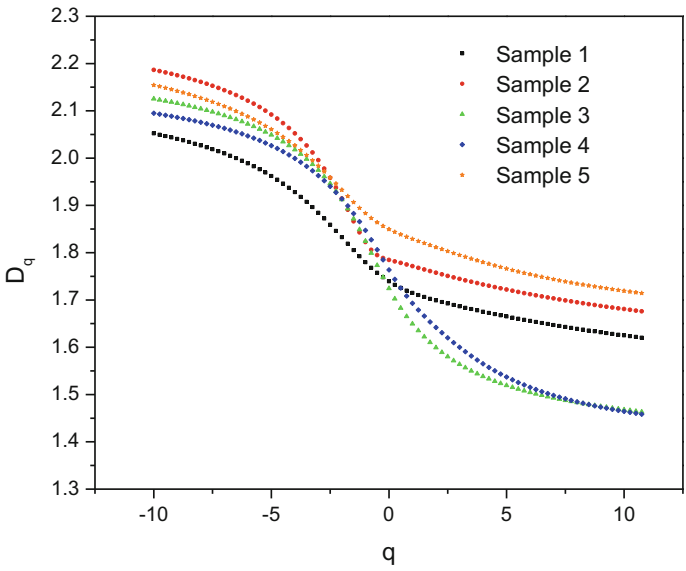

Fig. 2.8 Generalized dimensional spectra for the images of the five samples

Table 2.5 Values of D_0, D_1 and D_2 for the five samples

	D_0	D_1	D_2	D_1/D_0
Sample 1	1.7394	1.7149	1.6990	0.9859
Sample 2	1.7846	1.7716	1.7576	0.9927
Sample 3	1.7243	1.6495	1.5993	0.9566
Sample 4	1.7637	1.6930	1.6419	0.9599
Sample 5	1.8496	1.8289	1.8115	0.9888

The parameters in Table 2.5 demonstrate that all the five samples have the same characteristics: $D_0 > D_1 > D_2$, confirming that the pore distributions of the five samples are multifractal. Sample 5 has the highest D_0 value while Sample 3 showing the smallest demonstrating that Sample 5 has the most complex pore structures as opposed to Sample 3 with the least complex pore structures. The ratio of D_1/D_0 is an indication of the dispersion of the porosity with respect to the pore size since it provides the information of proportional variation instead of the absolute variation (Mendoza et al. 2010). Sample 2 and Sample 3, correspondingly, carry the largest and lowest ratio D_1/D_0 among the five samples tested in this study.

The multifractal spectrum can be plotted to visualize the distribution of the pores of the samples. Figure 2.9a illustrates the relationship between α_q and q of the five samples. Similar to D_q, α_q also decreases as q increases. As $q < 0$, α_q decreases steadily followed by a sudden drop. Figure 2.9b shows the relationship between $f(\alpha)$ and α_q. Due to the difference of the D_0 values in the five samples tested, a shift is observed in the crest of the spectra from top to the bottom, which corresponds to the apex of the spectrum. Sample 5 has the largest $f(\alpha)$ value due to its largest D_0 value among all the samples.

From the curves in Fig. 2.9a, we can read the values of α_{max} and α_{min}, which indicate the fluctuation of maximum and minimum probability of pixels (Costa and Nogueira 2015). The related extension of singularity length $\Delta\alpha$ which is defined as $\Delta\alpha = \alpha_{max} - \alpha_{min}$ can be calculated and the curve asymmetry of singularity spectrum (A) can be quantified based on the following equation (Hu et al. 2009; Shi et al. 2009):

$$A = \frac{\alpha_0 - \alpha_{min}}{\alpha_{max} - \alpha_0} \tag{2.24}$$

The values of A calculated for the samples are shown in Table 2.6. The data in this Table show that Sample 3 has the highest value of the $\Delta\alpha$ whereas Sample 1 experiencing the lowest value. Sample 3 has the largest probability distribution and strongest multifractality. The asymmetry values of Sample 1, 2 and 5 listed in Table 2.6 are less than 1, i.e. the curve is left skewed, indicating the domain of low exponents and slight fluctuation, while the values of Sample 3 and Sample 4 are larger than 1, demonstrating the domain of large exponents and large fluctuation.

The magnitude of the difference in the values of α_0 and D_0 is a measure of heterogeneity (Li et al. 2012). Figure 2.10 shows the plot of α_0 versus D_0 of the five tested samples. The data points of all samples deviate from the 45^0 line indicating

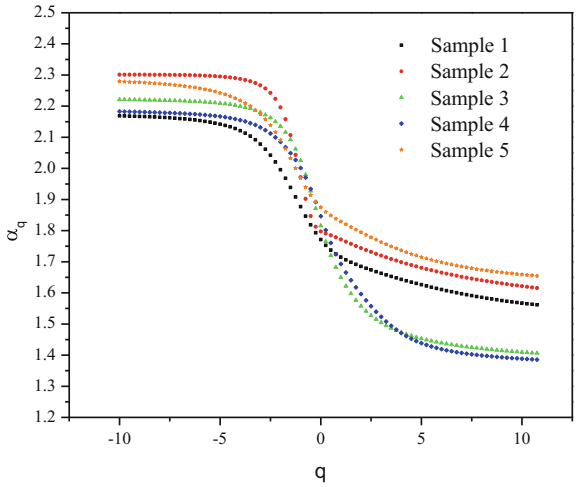

(a) $\alpha(q)$ versus q

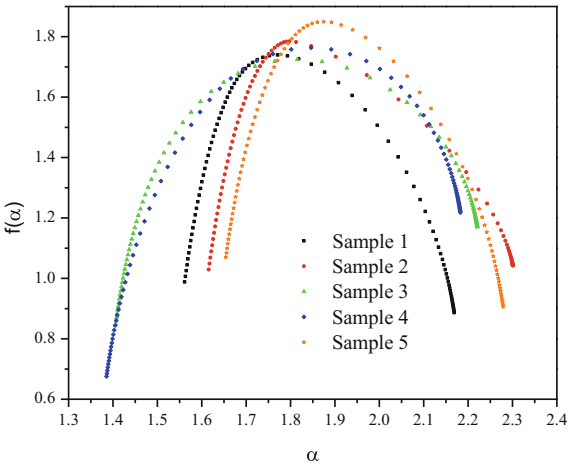

(b) $f(\alpha)$ versus $\alpha(q)$

Fig. 2.9 The multifractal spectrum of the five samples tested

Table 2.6 Values of $\Delta\alpha$ and asymmetry values of singularity spectrum (A) of samples

Sample	α_{max}	α_{min}	α_0	$\Delta\alpha$	A
1	2.1688	1.5615	1.7711	0.6073	0.5270
2	2.3009	1.6157	1.7973	0.6852	0.3606
3	2.2210	1.4062	1.8156	0.8148	1.0099
4	2.1826	1.3855	1.8464	0.7971	1.3709
5	2.2792	1.6544	1.8748	0.6248	0.5450

that the samples are heterogeneous and should be described by the multifractal spectra rather than the monofractal dimension. From Fig. 2.10, it can also be found that the distance between Sample 3 and the 45^0 line is the largest, indicating that Sample 3 is the most heterogeneous one among all these samples.

We changed the window moving size and calculated the related lacunarity. Figure 2.11 shows the grids of the image at different scales for Sample 1, as an example. Then we plotted lacunarity values against a range of different moving window sizes and the results presented in logarithmic axes. Figure 2.12 shows that the lacunarity values vary as the box size changes. In all cases, as the box size increases, the lacunarity value decreases. This is because at small spatial scales, the moving window size is much smaller than the size of the dominant textual components of the image, and most boxes are either mostly occupied or left empty. As a result, the variance of the number of occupied sites in a moving window is large, resulting in high lacunarity. As the box size increases, the size of the moving window increases and becomes larger than any repeating spatial pattern in the image, the variance in the number of the occupied sites in the moving window diminishes and the lacunarity tends to unity (and its logarithm value tends to zero) (Malhi and Román-Cuesta 2008). The plots of Sample 1 and Sample 2 show lower values than those of Sample 3, 4 and 5, showing smaller lacunarity values.

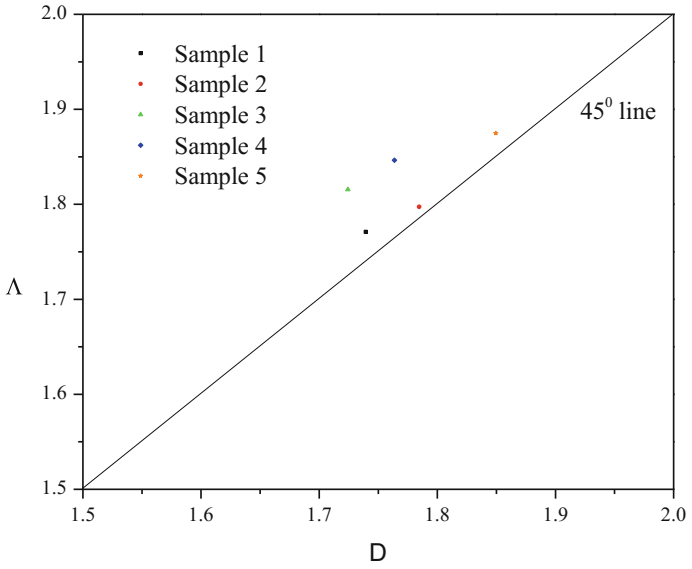

Fig. 2.10 Homogeneity of the five samples

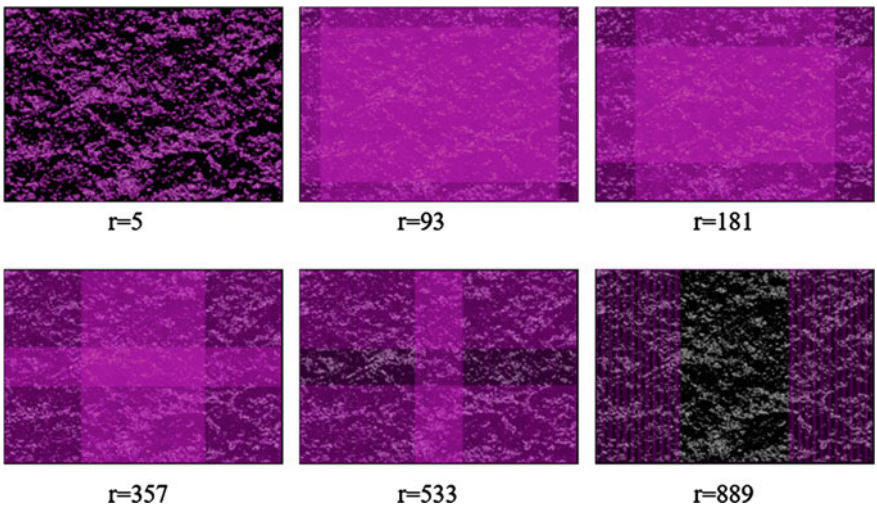

Fig. 2.11 SEM image of Sample 1 divided by grids with different length scale

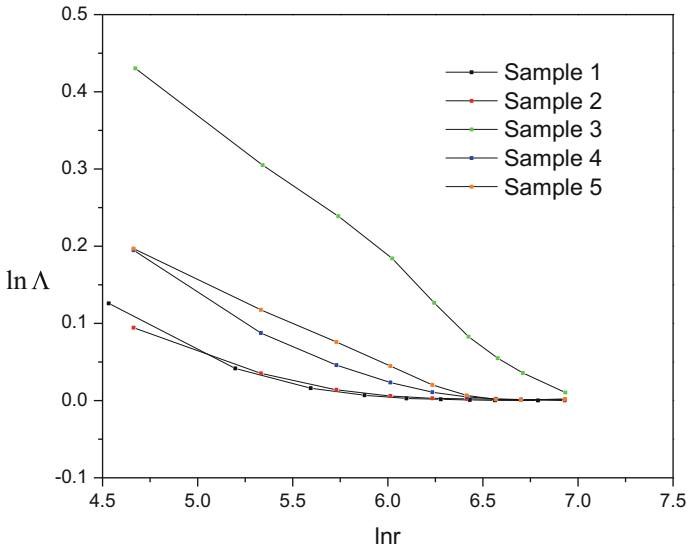

Fig. 2.12 Lacunarity analysis of five samples

The mean lacunarity, which is to put the heterogeneity from one perspective and one series of grid sizes into an average, was calculated based on the following equation (Costa and Nogueira 2015):

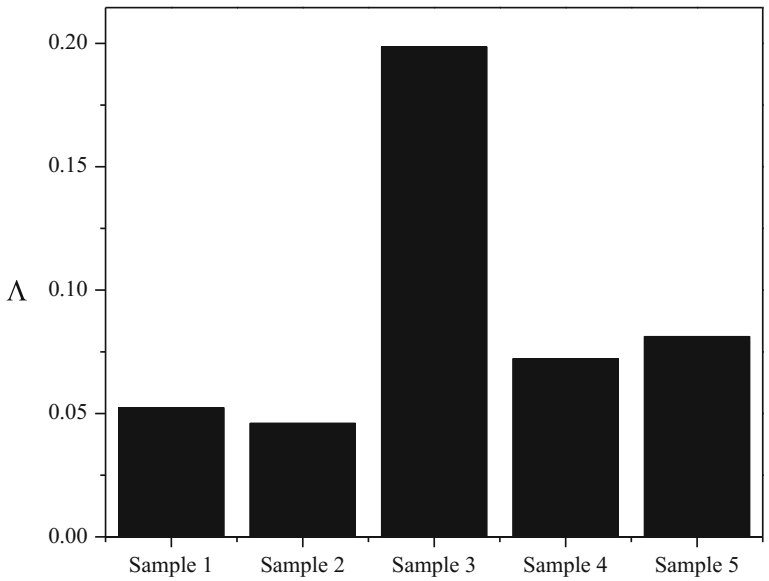

Fig. 2.13 Lacunarity values of five tested samples

$$\Lambda = \frac{\left[\sum_i (1 + \sigma(r)/u(r))^2\right]}{n(M, r)} \tag{2.25}$$

The results of the calculations for the five samples are shown in Fig. 2.13.

This figure shows that Sample 3 has the highest lacunarity value whereas Sample 2 has the lowest. As it was mentioned earlier, the sample with higher lacunarity has larger exhibits larger gaps in the image, indicating more heterogeneity. Overall, from the lacunarity analysis, Sample 3 exhibits the most heterogeneous pore structure among all samples. We compared the heterogeneity analysis using both lacunarity and multifractal fractal methods. The results showed that we could derive the same results, i.e. Sample 3 is the most heterogeneous and Sample 2 is the most homogeneous among all the testing samples, which demonstrates that multifractal theory and lacunarity method can derive same results regarding the samples' heterogeneity.

2.2.2 AFM

Figure 2.14a shows the relationships between force (V) and Z (the height) for the tip approaching and retracting process from one test point of the sample (Liu et al. 2017). When the cantilever is far away from the surface, there are no detect

interaction forces. As the cantilever approaches the surface, forces such as van der Waals electrostatic forces come into play. The gradually attractive force exceeds the spring constant, and the tip begins to contact the surface. As the tip retracts a particular point (adhesion force point), the spring constant exceeds the gradient of the force of adhesion and the tip suddenly breaks away from the sample to its equilibrium position (Kumar et al. 2008). Figure 2.14b are the part of the approaching and retracting curves of the sample of different points. From this pic we find different test points have different contact points, then we combined the location of the test points and contact point value and finally we got the topography image of the sample surface.

Figure 2.15a shows the topography image of one sample from Bakken Formation in 2D format. The color differences in the picture show the height difference. The darker the color in the image, the lower the depth of the test point. Figure 2.15b is the 3D image of the sample surface which can tell the height difference more directly.

Since the sample was polished, we can regard that the surface is very flat, then the height difference between different test points can be viewed as the existence of pores. We consider the highest height value point as the sample surface and then the height difference between the studying point and the highest point can be calculated as pore depth. Figure 2.16b illustrates the pore depth along the scanning line in Fig. 2.16a. The maximum pore depth in this scanning line is 0.5687 μm. A typical pore with diameter 2.43 μm and depth 0. 55621 μm was extracted and can be found in Fig. 2.6c. Then we calculated the pore surface area and volume area showing in Table 2.7. Results showed that this pore has a surface area around 1.03 μm^2 and

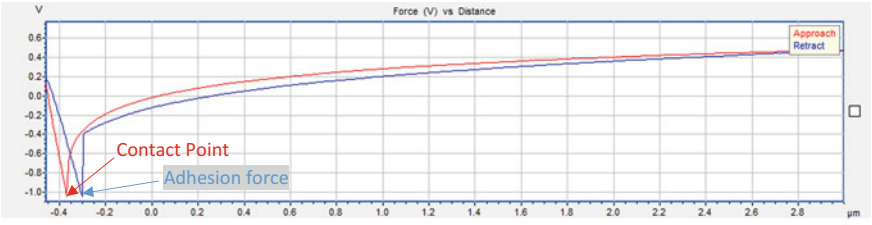

(a) One test point

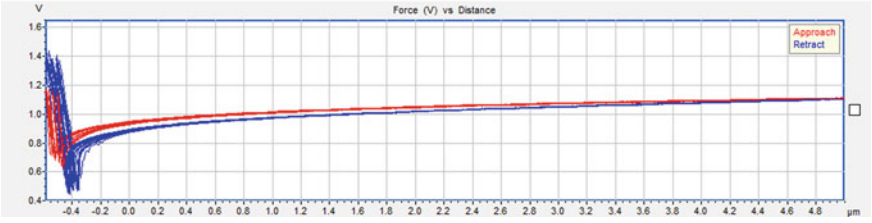

(b) Part of the whole test points

Fig. 2.14 Approaching and retracting curves

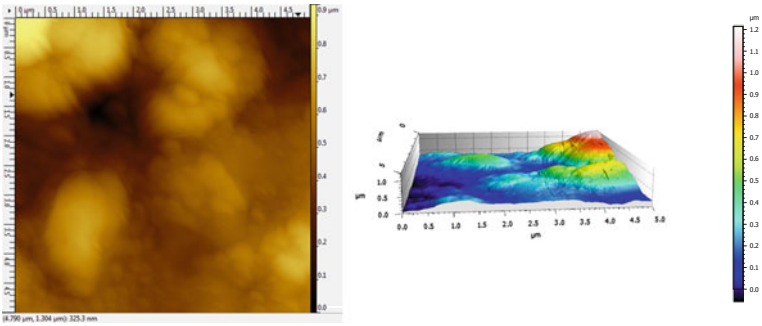

(a) 2D **(b)** 3D

Fig. 2.15 AFM image of the shale sample

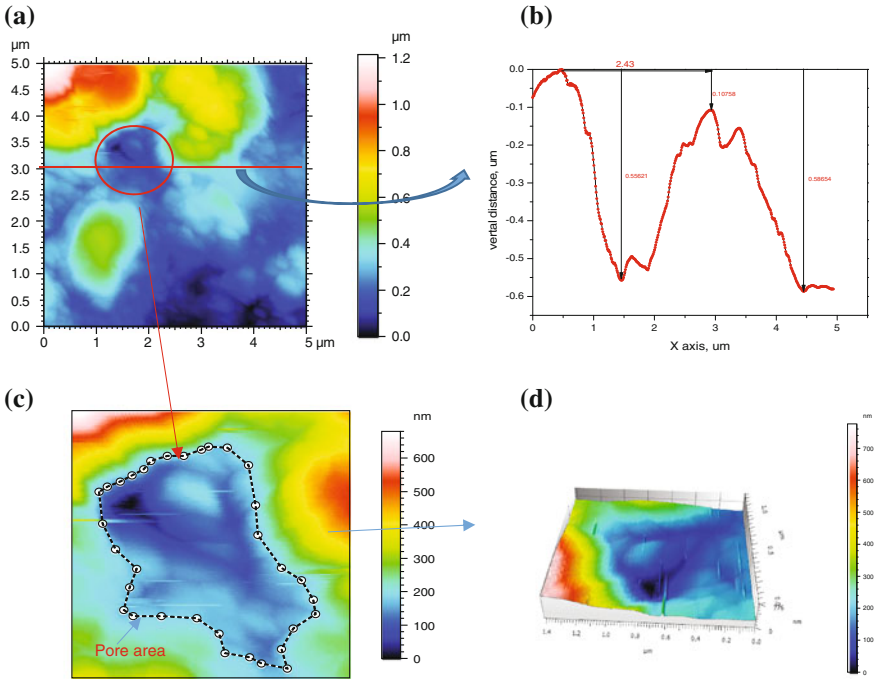

Fig. 2.16 Pore structure analysis (**a** is the surface image of the sample, **b** is the vertical distance value from line from (**a**), **c** is the pore image extracted from (**a**), and **d** is the 3D format of (**c**))

volume around 0.04467 μm^3. This further proves that AFM can detect the depth of the pores and estimate the pore volumes which is beyond the ability of SEM (Hirono et al. 2006).

Table 2.7 Pore parameters analyzed from Fig. 2.16c

Parameters	Value	Unit
Horizontal area	1.03	μm^2
Valley area	1.32	μm^2
Volume	44,676,431	nm^3
Perimeter	4.4	μm

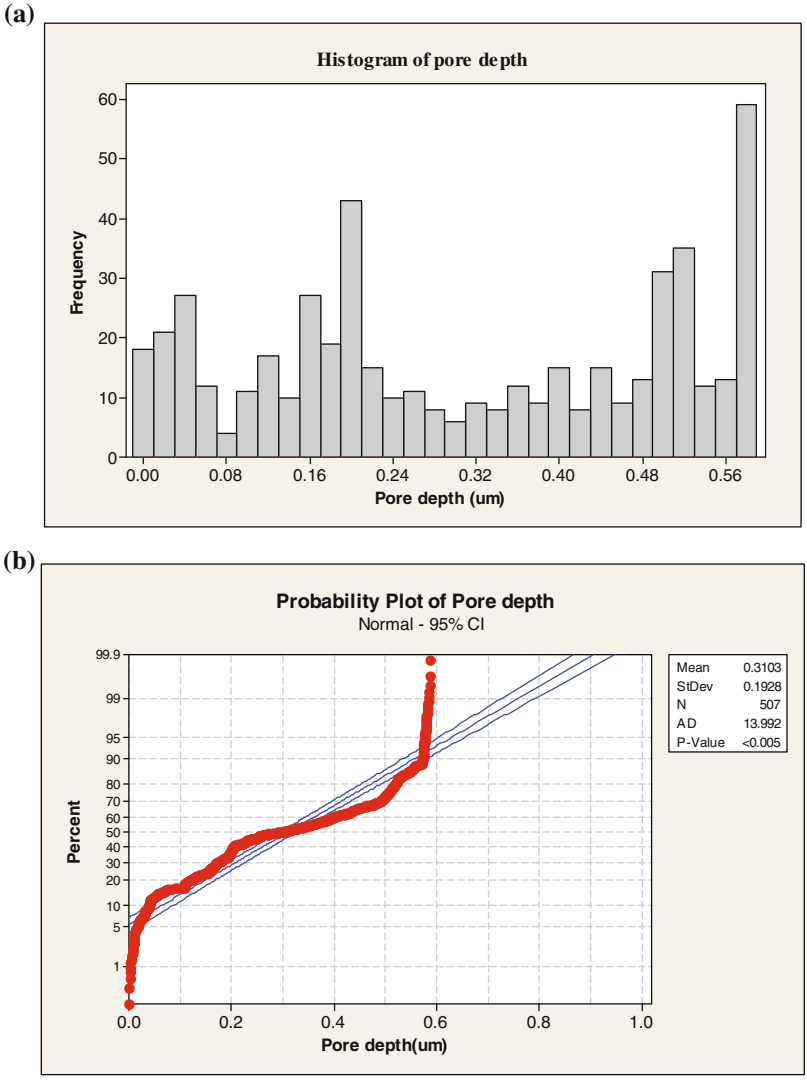

Fig. 2.17 Statistical analysis of the pore depth of the sample from the line (**a** is the Pore depth distribution and **b** is the probability plot)

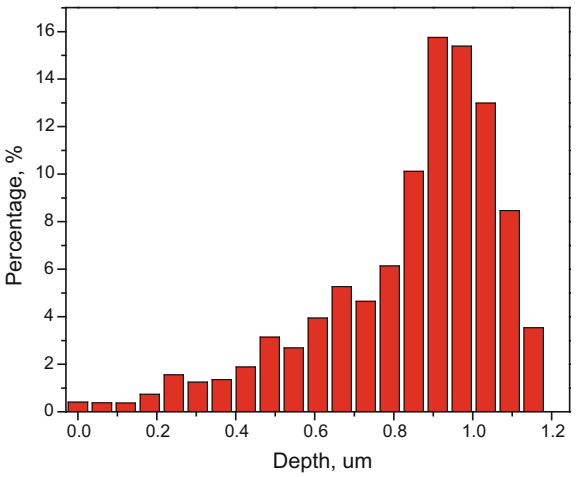

Fig. 2.18 Statistical analysis of the pore depth distributions of the whole sample surface

Pore size distributions play a major role in determining the adsorbing properties of the rock which need to be analyzed. Statistical analysis method was used to study the pore depth distributions of the line in Fig. 2.16a. Results can be observed from Fig. 2.17. Figure 2.17a illustrates that the number of pores with depth larger than 0.56 μm are the most while the number of the pores with depth around 0.08 μm are the least among all the groups. Probability plot of pore depth in Fig. 2.17b depicts that the mean of the pore depth of the pore is 0.3108 μm and around 70% of the pores have the depth less than 0.5 μm.

Based on the different depths of the test points, we get the distributions of the depths of the whole sample surface. Figure 2.18 shows that the depth of the sample surface has a wide range from 0 to 1.2 μm and more than 50% of the points are above 0.6 μm. The maximum pore depth of the scanned sample surface is 1.15445 μm, more than 60% of the pores whose depths are between 0.8 and 1.1 μm.

2.2.3 Gas Adsorption

2.2.3.1 Nitrogen Gas Adsorption Curve Analysis

Figure 2.19 represents the nitrogen gas adsorption data for the Bakken samples. At the extremely low relative pressure, the pores exhibit micro-pore filling and the amount of the adsorption will depend on the micro-pore volume. Then as the relative pressure increases, the multilayer adsorption will be formed. The knee-bend in Fig. 2.19a in the adsorption isotherm indicates the completion of the monolayer and the beginning of the multilayer, which can reflect the existence of the meso-pores and macro-pores. At the higher relative pressure, the gas in the pores

starts to condense. It should be mentioned that gas condensation at various pressures takes place in pores with different sizes. For the desorption part of the Middle Bakken samples (Fig. 2.19b), as the relative pressure decreases, the quantity of gas adsorption decreases. Then, the desorption curve was forced to coincide with the adsorption curve which is caused by the "tensile strength effect" (Groen et al. 2003). The hysteresis loop between the adsorption and desorption can be viewed in Fig. 2.19b due to the existence of the meso-pore pores in the Middle Bakken samples (Liu et al. 2017).

The capillary condensation will occur during adsorption and is proceeded by a metastable fluid state while capillary evaporation during desorption occurs via a hemispherical meniscus, separating the vapor and the capillary condensed phase (Groen et al. 2003). The sudden disappearance of the hysteresis loop in Fig. 2.19b around a certain relative pressure can indicate the presence of the small pores less than 4 nm in the Middle Bakken samples. This is due to the hemispherical meniscus that will collapse during the capillary evaporation in pores with the diameter less than 4 nm. The shape of the hysteresis loop can indicate the pore type of the porous medium. From Fig. 2.19 in the Middle Bakken samples, the desorption part of measurement exhibits an obvious yielding point at the critical relative pressure. When the relative pressure becomes larger than the critical point, the adsorption and desorption both increase steeply and the hysteresis loop is very narrow which represents the plate type pores in the Middle Bakken Formation. For the Upper and Lower Bakken, the hysteresis loop is very wide and the adsorption and desorption portion of the curve is flat from the beginning to the end of desorption, which represents the silt type pore. In comparison with Middle Bakken samples, the hysteresis loop in the Upper and Lower Bakken samples does not disappear suddenly and there was no obvious forced closure phenomenon (Fig. 2.19a, c). This indicates that the samples from Upper and Lower Bakken Formation contain abundant pores smaller than 4 nm (Cao et al. 2015). The plate-shape pores in the Middle Bakken and the silt-shape pores in Upper and Lower Bakken is advantageous for the flow of the hydrocarbon due to their excellent openness. None of the samples we analysed in this study, showed a horizontal plateau at the relative pressure close to 1, which illustrates that the Bakken shale samples still contain a range of macro-pores which cannot be analysed by the nitrogen gas adsorption method (Cao et al. 2016; Schmitt et al. 2013).

2.2.3.2 PSD Analysis from the Nitrogen Adsorption

Due to the tensile strength effect, the pore size distribution analysis which can be estimated from the desorption curve, will be limited to 4–5 nm which cannot describe the pore structures accurately. So, the adsorption branch will be chosen for the PSD analysis. Figure 2.20 shows the pore size distribution of the samples based on the DFT theory. The PSD curve of all samples exhibited the multimodal characteristic with several volumetric maxima. The pore structures were analysed and the following observations were reached:

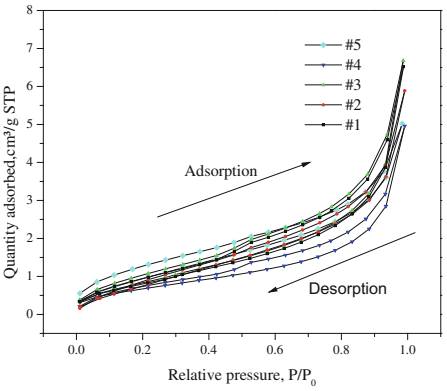

(a) Upper Bakken

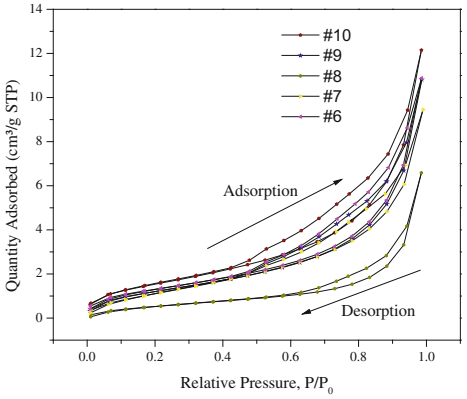

(b) Middle Bakken

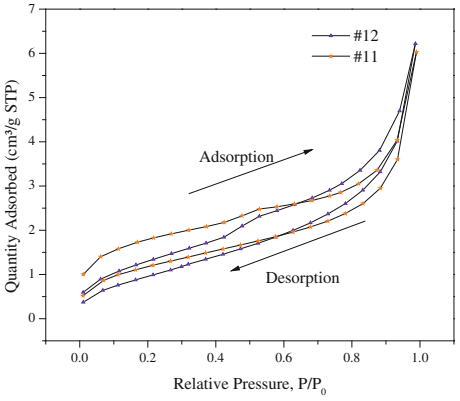

(c) Lower Bakken

Fig. 2.19 Low pressure N_2 isotherms for the Bakken shale samples

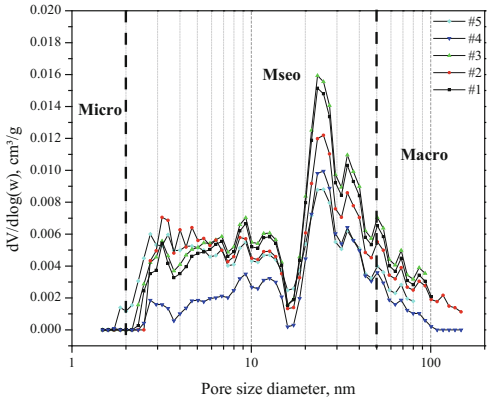

(a) Upper Bakken

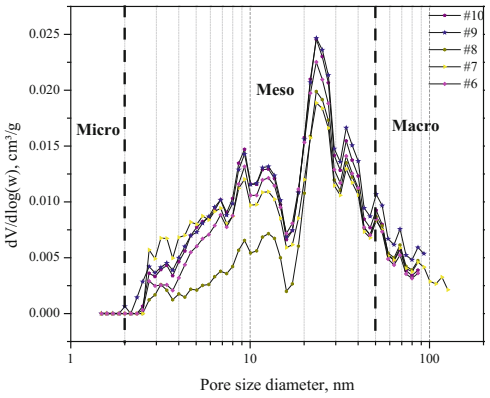

(b) Middle Bakken

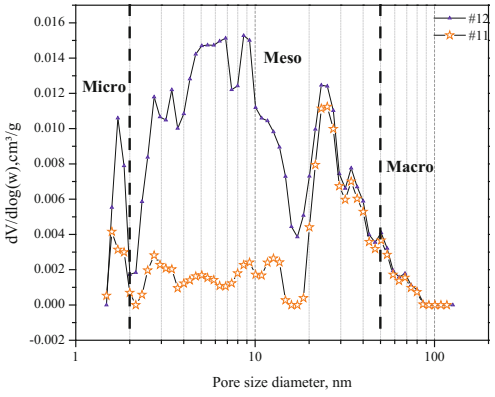

(c) Lower Bakken

Fig. 2.20 PSD analysis of Bakken samples using nitrogen adsorption

Table 2.8 Low pressure nitrogen adsorption analysis results

Samples	Bakken formation	BET surface area (m^2/g)	Total pore volume (cm^3/100 g)	Micro-meso pore (cm^3/100 g)	Average pore diameter (nm)
#1	UpperBakken	3.292	0.937	0.829	11.384
#2	UpperBakken	3.785	0.887	0.765	9.370
#3	UpperBakken	3.481	1.003	0.890	11.525
#4	UpperBakken	2.624	0.476	0.435	7.262
#5	UpperBakken	4.08	0.747	0.697	7.321
#6	MiddleBakken	5.021	1.372	1.265	10.929
#7	MiddleBakken	4.823	1.425	1.256	11.818
#8	MiddleBakken	2.197	0.998	0.874	18.179
#9	MiddleBakken	4.765	1.633	1.462	13.711
#10	MiddleBakken	5.934	1.525	1.409	10.277
#11	Lower Bakken	4.359	0.499	0.469	4.581
#12	Lower Bakken	3.897	0.856	0.777	8.784

- Middle Bakken has larger pore volume and average pore size diameter than the Upper and Lower Bakken (Table 2.8).
- Positive relationships exist between macro pore volume and average pore diameter (Fig. 2.21a); total pore volume and pore diameter (Fig. 2.21b).
- An overall inverse correlation exists between the average pore diameter and the BET surface area (Fig. 2.22a). BET shows an increasing trend as the micro-meso pore volume increases (Fig. 2.22b) while no obvious relationship can be seen between the macro-pore volume and BET surface area (Fig. 2.22c).

2.2.3.3 Fractal Analysis

Based on previous studies (Sun et al. 2016), the nitrogen adsorption isotherm can be divided into two main regions (Fig. 2.23a). Region 1 is the monolayer-multilayer adsorption in which the dominant force is van der Waals and Region 2 is the capillary condensation regime with the surface tension being the dominant force (Khalili et al. 2000; Qi et al. 2002). We separated the nitrogen adsorption isotherm and analysed the fractal behaviour of the two regions respectively. D_1 can reflect the fractal behaviour of region 1 with D_2 representing the fractal behaviour of region 2 (Fig. 2.23b). The fractal analysis results for the samples are presented in Table 2.9. The results show that for all the samples, the fractal dimension of region 2 (D_2) is larger than the fractal dimension of region 1 (D_1). This is interpreted as D_2 describes the capillary condensation of gas clumps occurred in the shale pores while D_1 value represents the mono-multilayer adsorption. As more gas was adsorbed, more molecules were available to cover the aggregated outline thus increasing the surface fractal dimension (Sahouli et al. 1997; Tang et al. 2016). D_2 is larger than

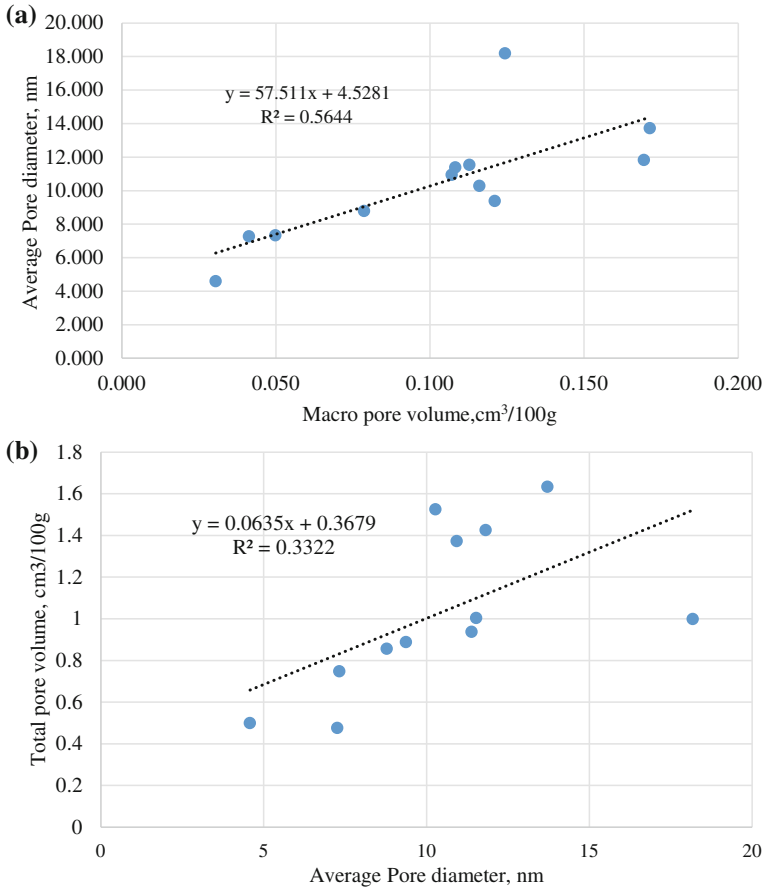

Fig. 2.21 Average pore diameter versus **a** Macro-pore volume and **b** Total pore volume

D_1 can also indicate that the pore structures of the shale samples are more complicated than the pore surface. Samples from the Middle Bakken Formation with higher average D_1 values and lower D_2 values than samples from the Upper and Lower Bakken Formation corresponds to more irregular pore surface and less complicated pore structures.

The correlations between the fractal dimension (D_2) and the pore structures were analysed further. Figure 2.24 shows that the fractal dimension D_2 has a negative linear relationship between the total pore volume and the average diameter. The shale samples in the Bakken Formation with smaller pore volume and smaller average diameter tends to have higher fractal dimension D_2, demonstrating that those samples have more complex pore structures.

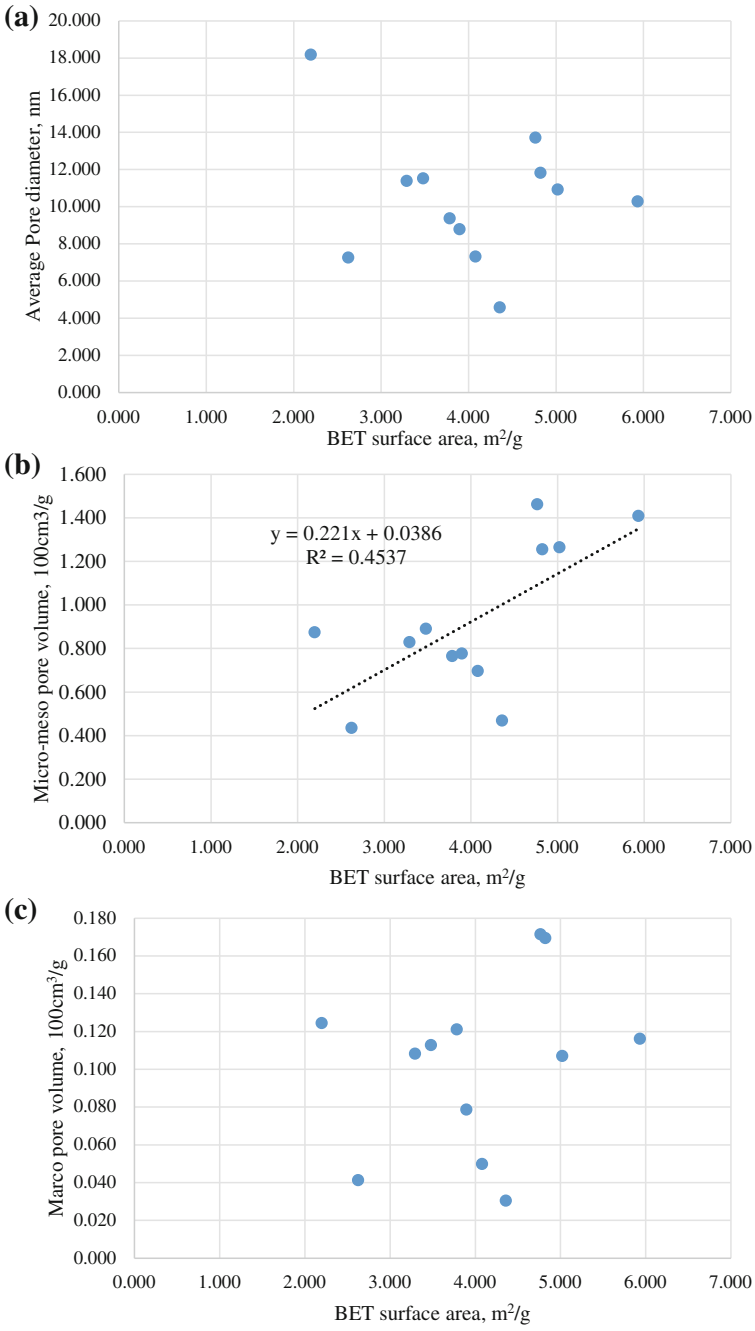

Fig. 2.22 BET versus **a** Average pore diameter. **b** Micro-meso pore volume and **c** Macro pore volume

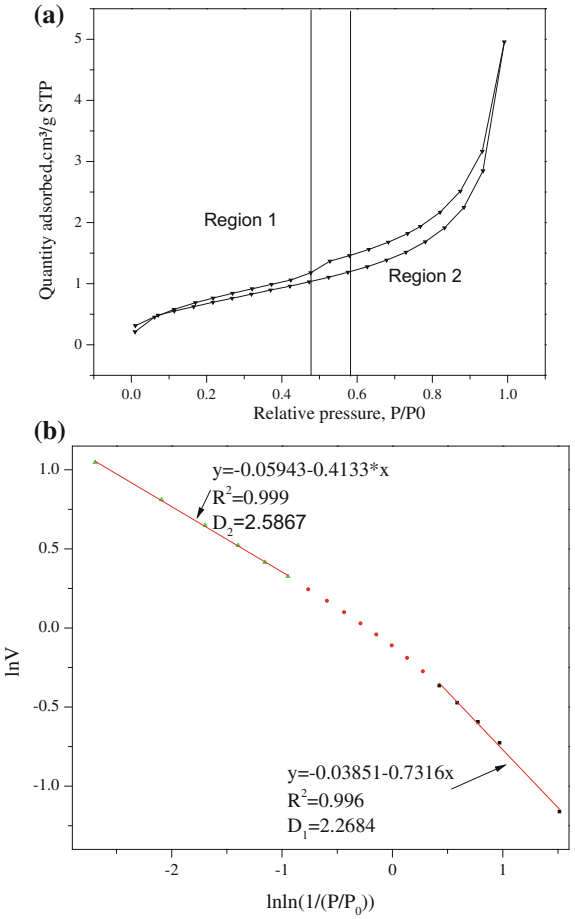

Fig. 2.23 Fractal analysis of Bakken sample (#4)

2.2.3.4 CO_2 Adsorption Analysis

In order to characterize the pores with sizes less than 2 nm, CO_2 gas adsorption was applied. Figure 2.25 shows the CO_2 adsorption isotherms of all samples tested in this study. The CO_2 adsorption isotherms of the Upper Bakken and Lower Bakken have similar shapes. As the relative pressure increases from 0, the adsorption quantity increases rapidly followed by a slow increase after the relative pressure reaches a critical point. For the Middle Bakken, the adsorption quantity increases with an increasing rate as the relative pressure increases. This is since CO_2 is first adsorbed into the smaller pores and then into the relatively large pores as relative pressure increases. The difference in the CO_2 adsorption isotherms between the Upper/Lower and the Middle Bakken Formation originates from their different pore microstructures. The results in Table 2.10 show that Upper and Lower Bakken formations own more micro-pores (approximately 3 times) than the Middle Bakken.

Table 2.9 Fractal analysis of the Bakken samples

Samples	Bakken formation	Slope	D_1	R^2	Slope	D_2	R^2
#1	Upper Bakken	0.769	2.231	0.998	0.368	2.632	0.991
#2	Upper Bakken	1.297	1.703	0.999	0.269	2.731	0.993
#3	Upper Bakken	0.885	2.115	0.997	0.359	2.641	0.995
#4	Upper Bakken	0.732	2.268	0.996	0.413	2.587	0.999
#5	Upper Bakken	0.952	2.048	0.999	0.270	2.730	0.994
#6	Middle Bakken	0.632	2.368	0.999	0.519	2.481	0.998
#7	Middle Bakken	1.107	1.893	0.996	0.456	2.544	0.996
#8	Middle Bakken	0.868	2.132	0.997	0.602	2.398	0.999
#9	Middle Bakken	0.724	2.276	0.996	0.500	2.500	0.997
#10	Middle Bakken	0.662	2.338	0.999	0.470	2.530	0.997
#11	Lower Bakken	0.818	2.182	0.990	0.298	2.703	0.999
#12	Lower Bakken	0.895	2.105	0.994	0.304	2.697	0.994

Pores with sizes less than 1 nm exist in the Upper and Lower Bakken. Pores with size range of 1–2 nm are the main contributors to the total porosity of micro-pores for the Bakken samples.

2.2.3.5 Full Range Pore Size Analysis

CO_2 adsorption can characterize the pore sizes less than 2 nm while nitrogen performs well in quantifying the meso-pores and the macro-pores (less than 200 nm). In this section, the pore size distribution results of the two gas adsorption methods were combined in order to analyse the pore structures. The blue curve in Fig. 2.9 shows the pore size distributions (less than 200 nm) of several samples. In order for quantitative measure of the pore size distributions, deconvolution method was applied to determine the mean size and the standard deviation of each pore size family in a given distribution. The pore size family can be quantified by the distinct peaks from the pore size distribution. Gaussian/normal distribution is commonly used to describe the experiments regardless of whatever probability distribution describes an individual experimental result. The detailed deconvolution procedure can be found in Ulm et al. (2007). In this procedure, it can be assumed that the pores can be divided into $J = 1, n$ pore size groups with sufficient contrast in pore size distributions. The J_{th} pore group occupies a volume fraction f_J of the total porosity. The theoretical probability density function (PDF) of the single phase, which is assumed to fit a normal distribution is defined as:

$$P_J(x_i, U_J, S_J) = \frac{2}{\sqrt{2\pi(S_J)^2}} \exp\left(\frac{-(x_i - (U_J))^2}{2(S_J)^2}\right), \tag{2.26}$$

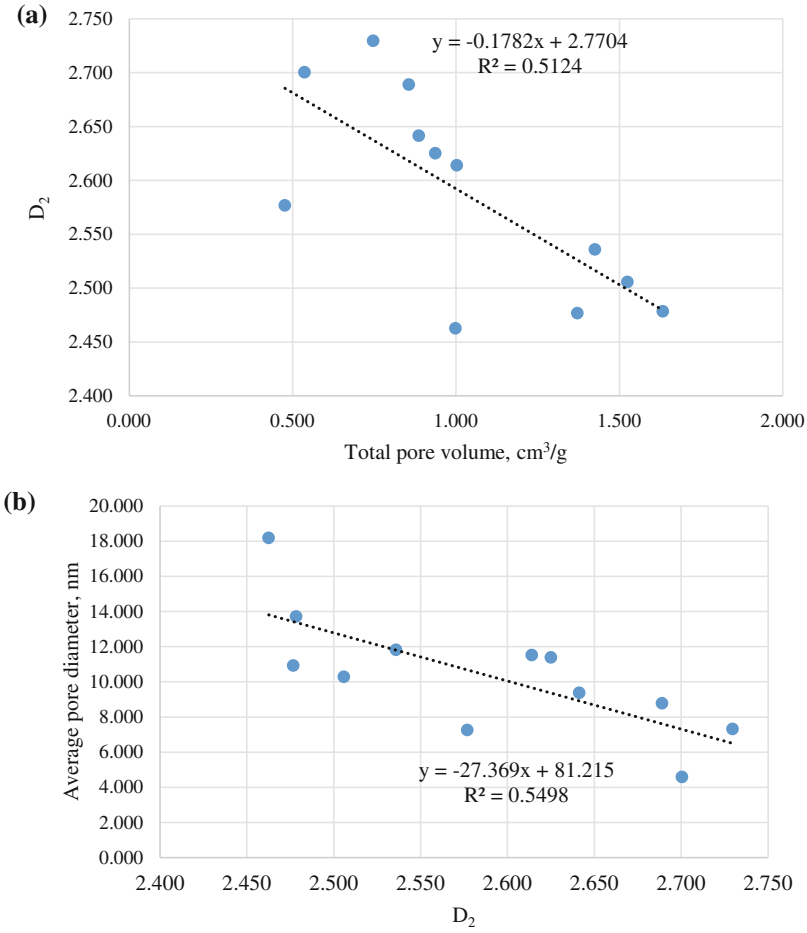

Fig. 2.24 Correlations between the D_2 and **a** Total pore volume. **b** Average pore diameter

where U_J and S_J are the mean value and the standard deviation of pore size distributions of the phase $J = 1$ to n. Minimizing the difference between the data from the weighted model-phase probability distribution function (PDF) and the experimental PDF using the following equation, we can derive the unknowns $\{f_J, U_J, S_J,\}$:

$$\min\left[\sum_{i=1}^{m}\sum^{N}\left(\sum_{J}^{n} f_J P_J(x_i, U_J, S_J) - P_x(x_i)\right)^2\right] \tag{2.27}$$

$$\sum_{J=1}^{n} f_J = 1 \tag{2.28}$$

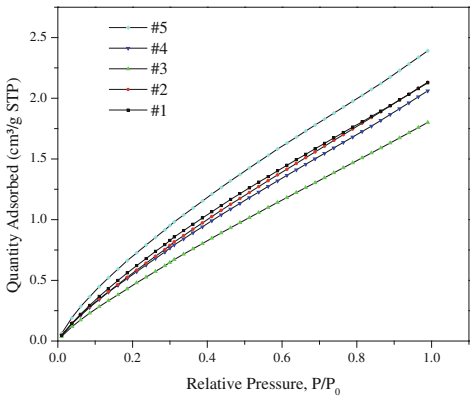

(a) Upper Bakken

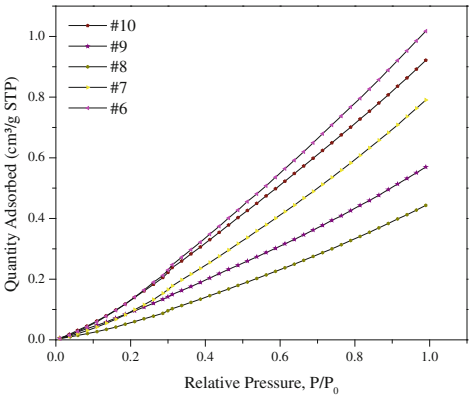

(b) Middle Bakken

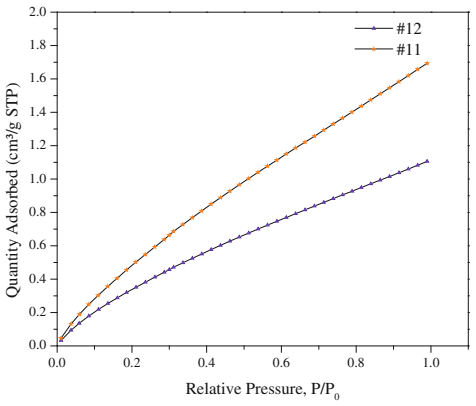

(c) Lower Bakken

Fig. 2.25 CO_2 adsorption isotherms for Bakken samples

Table 2.10 Pore size analysis from the CO_2 adsorption

Samples	Bakken formation	Micro-pore <2 nm (cm^3/100 g)	Micro-pore <1 nm (cm^3/100 g)
#1	Upper Bakken	0.159	0.025
#2	Upper Bakken	0.152	0.025
#3	Upper Bakken	0.126	0.020
#4	Upper Bakken	0.146	0.025
#5	Upper Bakken	0.186	0.039
#6	Middle Bakken	0.048	0.000
#7	Middle Bakken	0.035	0.000
#8	Middle Bakken	0.019	0.000
#9	Middle Bakken	0.028	0.000
#10	Middle Bakken	0.048	0.000
#11	Lower Bakken	0.128	0.024
#12	Lower Bakken	0.090	0.020

In the above equation, $P_x(x_i)$ is the measured value of the normalized frequency of the pore size x_i and m is the number of the intervals (bins).

To ensure that the pore size groups have sufficient contrast, the overlap of successive Gaussian curves representative of the two phases is constrained by the following criterion (Sorelli et al. 2008).

$$U_J + S_J < U_{J+1} + S_{J+1} \tag{2.29}$$

The colorful curves in Fig. 2.26 display the deconvolution results of the samples and the red dash curve shows the fit sum of the deconvolution phases. The fitting coefficients of all the samples are above 0.85 which shows that the models fit the experiment data very well. It can be found that the pores in Upper, Middle and Lower Bakken have five typical pore size categories. The deconvolution results of the samples demonstrate that the Bakken samples analysed (Upper, Middle, and Lower Bakken shales) have similar pore size families. One pore size category exists in the micro-pore scale with mean value around 1.5 nm (Family 1), which is defined as the micro-pore size family and one pore size category that is in the macroscale with mean size value larger than 50 nm (Family 5), which is defined as the macro-pore size family. The other three pore families belong to the meso-pore scale with mean size value 9 nm (Family 2), 24 nm (Family 3) and 34 nm (Family 4), respectively, which can be defined as the meso-pore families. Compared with the volume ratios of each pore size family, it was observed that the percentage of micro-pore size family is larger in the samples from the Upper and Lower Bakken than that of the Middle Bakken.

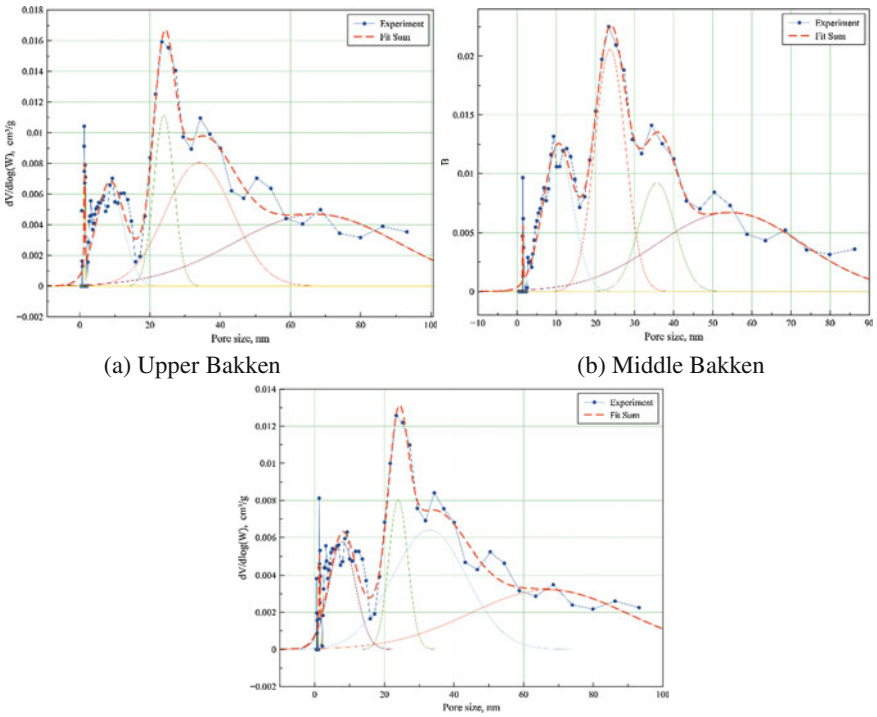

Fig. 2.26 Full pore size distribution from gas adsorption and its deconvolution results

References

Allain C, Cloitre M (1991) Characterizing the lacunarity of random and deterministic fractal sets. Phys Rev Ann 44:3552–3558

Amankwah KAG, Schwarz JA (1995) A modified approach for estimating pseudo-vapor pressures in the application of the Dubinin-Astakhov equation. Carbon 33:1313–1319

Anovitz LM, Cole DR (2015) Characterization and analysis of porosity and pore structures. Rev Miner Geochem 80(1):61–164

Avnir D, Jaroniec M (1989) An isotherm equation for adsorption on fractal surfaces of heterogeneous porous materials. Langmuir 5(6):1431–1433

Backes AR (2013) A new approach to estimate lacunarity of texture images. Pattern Recognit Lett 34(13):1455–1461

Binnig G, Quate CF, Gerber C (1986) Atomic force microscopy. Phys Rev Lett 56(9):930–933

Boadu FK (2000) Predicting the transport properties of fractured rocks from seismic information: numerical experiments. J Appl Geophys 44(2–3):103–113

Bogner A, Jouneau PH, Thollet G, Basset D, Gauthier C (2007) A history of scanning electron microscopy developments: towards "wet-STEM" imaging. Micron 38(4):390–401

Bruening FA, Cohen AD (2005) Measuring surface properties and oxidation of coal macerals using the atomic force microscope. Int J Coal Geol 63:195–204

Cai Y, Liu D, Yao Y et al (2011) Fractal characteristics of coal pores based on classic geometry and thermodynamics models. Acta Geol Sin (English) 85(5):1150–1162

Cao TT, Song ZG, Wang SB et al (2015) A comparative study of the specific surface area and pore structure of different shales and their kerogens. Sci China Earth Sci 58(4):510–522
Cao Z, Liu G, Zhan H et al (2016) Pore structure characterization of Chang-7 tight sandstone using MICP combined with N2GA techniques and its geological control factors. Sci Rep-UK 6:36919
Chhabra A, Jensen RV (1989) Direction of determination of the f(a) singularity spectrum. Phys Rev Lett 62(12):1327–1330
Costa EVL, Nogueira RA (2015) Fractal, multifractal and lacunarity analysis applied in retinal regions of diabetic patients with and without nonproliferative diabetic retinopathy. Fractal Geom Nonlinear Anal Med Biol 1(3):112–119
Cox EP (1927) A method of assigning numerical and percentage values to the degree of roundness of sand grains. J Paleontol 1(3):179–183
Do DD, Do HD (2003) Pore characterization of carbonaceous materials by DFT and GCMC simulations: a review. Adsorpt Sci Technol 21(5):389–423
Fan L, Ziegler T (1992) Nonlocal density functional theory as a practical tool in calculations on transition states and activation energies. Applications to elementary reaction steps in organic chemistry. J Am Chem Soc 114:10890–10897
Feder J (1988) Fractals. Plenum Press, New York
Goldstein JI, Newbury DE, Echlin P (1981) Scanning electron microscopy and X-ray microanalysis. A text for biologists, material scientists, and geologists, Plenum Press, New York, 673 p
Groen JC, Peffer LAA, Pérez-Ramírez J (2003) Pore size determination in modified micro-and mesoporous materials. Pitfalls and limitations in gas adsorption data analysis. Micropor Mesopor Mat 60(1):1–17
Halsey TC, Hensen MH, Kadanoff LP et al (1986) Fractal measures and their singularities: the characterization of strange sets. Phys Rev A 33(2):1141–1151
Hirono T, Lin W, Nakashima S (2006) Pore space visualization of rocks using an atomic force microscope. Int J Rock Mech Min Sci 43:317–320
Houben ME, Desbois G, Urai JL (2014) A comparative study of representative 2D microstructures in Shale and Sandy facies of Opalinus Clay (Mont Terri, Switzerland) inferred from BIB-SEM and MIP methods. Mar Pet Geol 49:143–161
Hu MG, Wang JF, Ge Y (2009) Super-resolution reconstruction of remote sensing images using multifractal analysis. Sensors 9(11):8669–8683
Javadpour F (2009) CO_2 injection in geological formations: determining macroscale coefficients from pore scale processes. Transp Porous Med 79:87–105
Javadpour F, Farshi MM, Amrein M (2012) Atomic force microscopy: a new tool for gas-shale characterization. J Can Pet Technol 51(04):236–243
Joos J, Carraro T, Weber A, Ivers-Tiffée E (2011) Reconstruction of porous electrodes by FIB/SEM for detailed microstructure modeling. J Power Sour 196(17):7302–7307
Khalili NR, Pan M, Sandi G (2000) Determination of fractal dimensions of solid carbons from gas and liquid phase adsorption isotherms. Carbon 38(4):573–588
Kuila U, Prasad M (2013) Specific surface area and pore-size distribution in clays and shales. Geophys Prospect 61(2):341–362
Labani MM, Rezaee R, Saeedi A et al (2013) Evaluation of pore size spectrum of gas shale reservoirs using low pressure nitrogen adsorption, gas expansion and mercury porosimetry: a case study from the Perth and Canning Basins, Western Australia. J Petrol Sci Eng 112:7–16
Li L, Chang L, Le S, Huang D (2012) Multifractal analysis and lacunarity analysis: A promising method for the automated assessment of muskmelon (*Cucumis melo L.*) epidermis netting. Comput Electron Agric 88:72–84
Liu K, Ostadhassan M (2017a) Quantification of the microstructures of Bakken shale reservoirs using multi-fractal and lacunarity analysis. J Nat Gas Sci Eng 39:62–71
Liu K, Ostadhassan M (2017b) Microstructural and geomechanical analysis of Bakken shale at nanoscale. J Pet Sci Eng 153:133–144
Liu K, Ostadhassan M (2017c) Multi-scale fractal analysis of pores in shale rocks. J Appl Geophys 140:1–10

Liu K, Ostadhassan M, Bubach B (2016a) Pore structure analysis by using atomic force microscopy. URTEC 2448210

Liu K, Ostadhassan M, Jabbari H, Bubach B (2016b) Potential application of atomic force microscopy in characterization of nano-pore structures of Bakken formation. In: Society of petroleum engineers, 2016

Liu K, Ostadhassan M, Zhou J, Gentzis T, Rezaee R (2017) Nanoscale pore structure characterization of the Bakken shale in the USA. Fuel 209:567–578

Lopes R, Betrouni N (2009) Fractal and multifractal analysis: a review. Med Image Anal 13 (4):634–649

Malhi Y, Román-Cuesta RM (2008) Analysis of lacunarity and scales of spatial homogeneity in IKONOS images of Amazonian tropical forest canopies. Remote Sens Environ 112(5):2074–2087

Mandelbrot BB (1982) The fractal geometry of nature. Freeman, New York

Mandelbrot BB (1983) The fractal geometry of nature. WH Freeman & Co., New York

Mendoza F, Verboven P, Ho QT et al (2010) Multifractal properties of pore-size distribution in apple tissue using X-ray imaging. J Food Eng 99(2):206–215

Plotnick RE, Gardner RH, O'Neill RV (1993) Lacunarity indices as measures of landscape texture. Lands Ecol 8(3):201–211

Qi H, Ma J, Wong P (2002) Adsorption isotherms of fractal surfaces. Colloid Surf A 206(1):401–407

Ravikovitch PI, Haller GL, Neimark AV (1998) Density functional theory model for calculating pore size distributions: pore structure of nanoporous catalysts. Adv Colloid Interfac 76:203–226

Russel DA, Hanson J, Ott E (1980) Dimension of strange attractors. Phys Rev Lett 45(14):1175–1178

Sahouli B, Blacher S, Brouers F (1997) Applicability of the fractal FHH equation. Langmuir 13 (16):4391–4394

Sanyal D, Ramachandrarao P, Gupta OP (2006) A fractal description of transport phenomena in dendritic porous network. Chem Eng Sci 61(2):307–315

Schmitt M, Fernandes CP, da Cunha Neto JAB et al (2013) Characterization of pore systems in seal rocks using nitrogen gas adsorption combined with mercury injection capillary pressure techniques. Mar Pet Geol 39(1):138–149

Shi K, Liu CQ, Ai NS (2009) Monofractal and multifractal approaches in investigating temporal variation of air pollution indexes. Fractals 17:513–521

Smith TG, Lange GD, Marks WB (1996) Fractal methods and results in cellular morphology—dimensions, lacunarity and multifractals. J Neurosci Methods 69(2):123–136

Sorelli L, Constantinides G, Ulm F-J, Toutlemonde F (2008) The nano-mechanical signature of ultra high performance concrete by statistical nanoindentation techniques. Cem Concr Res 38 (12):1447–1456

Sun M, Yu B, Hu Q et al (2016) Nanoscale pore characteristics of the Lower Cambrian Niutitang Formation Shale: a case study from Well Yuke# 1 in the Southeast of Chongqing, China. Int J Coal Geol 154:16–29

Takashimizu Y, Iiyoshi M (2016) New parameter of roundness R: circularity corrected by aspect ratio. Prog Earth Planet Sci 3(1):1–16

Tang P, Chew NYK, Chan HK et al (2003) Limitation of determination of surface fractal dimension using N_2 adsorption isotherms and modified Frenkel–Halsey–Hill theory. Langmuir 19(7):2632–2638

Tang X, Jiang Z, Jiang S et al (2016) Effect of organic matter and maturity on pore size distribution and gas storage capacity in high-mature to post-mature shales. Energy Fuels 30(11):8985–8996

Ulm FJ, Vandamme M, Bobko C et al (2007) Statistical indentation techniques for hydrated nanocomposites: concrete, bone, and shale. J Am Ceram Soc 90(9):2677–2692

Vasseur J et al (2015) Heterogeneity: the key to failure forecasting. Sci Rep 5:13259

Wang H et al (2012) Fractal analysis and its impact factors on pore structure of artificial cores based on the images obtained using magnetic resonance imaging. J Appl Geophys 86:70–81

Wong HS, Head MK, Buenfeld NR (2006) Pore segmentation of cement-based materials from backscattered electron images. Cem Concr Res 36(6):1083–1090

Yao Y, Liu D, Tang D et al (2008) Fractal characterization of adsorption-pores of coals from North China: an investigation on CH_4 adsorption capacity of coals. Int J Coal Geol 73(1):27–42

Chapter 3
Geochemical Properties

Abstract Shale reservoirs with organic-rich intervals are often characterized by high quantities of kerogen, bitumen and also moveable hydrocarbons. Despite lots of conducted studies to improve understanding of the shale characteristics, kerogen, as one the main constituents of mudrocks, is not thoroughly understood. Understanding organic matter properties in terms of maturity, content, and type are crucial for the development of unconventional reservoirs. Studies also showed the presence of organic matter has a non-negligible effect on hydraulic fracturing operations. In this chapter, organic matter characterization by conventional methods along with a new analytical method known as Raman spectroscopy are discussed.

3.1 Characterizing Geochemical Properties of Organic Matter

Organic matter, predominantly kerogen, is formed from the burial and preservation of living organisms and is interspersed within the mineral matrix (Hutton et al. 1994), Fig. 3.1. In order to study organic matter properties, bulk sample, Fig. 3.1a, or isolated kerogen, Fig. 3.1b–d, can be used. Rock-Eval pyrolysis, vitrinite reflectance, infrared and Raman spectroscopy, elemental analysis, and X-ray absorption near edge structure are some techniques for evaluating the organic matter. Parameters that are mostly considered are: maturity level, hydrogen and oxygen richness, total organic content, aromaticity of kerogen structure, and potential to produce hydrocarbon which are discussed in the following sections.

The main method to understand the thermal maturity of kerogen is the optical inspection of vitrinite macerals, known as vitrinite reflectance (Diessel et al. 1978). Vitrinite reflectance analysis can be challenging when samples contain dispersed or no primary vitrinite (Hackley et al. 2015; Sauerer et al. 2017), Fig. 3.2. In order to find the maturity for these samples, a mean of bitumen maturity (%Bro) can be used

M. Ostadhassan et al., *Fine Scale Characterization of Shale Reservoirs*,
SpringerBriefs in Petroleum Geoscience & Engineering,
https://doi.org/10.1007/978-3-319-76087-2_3

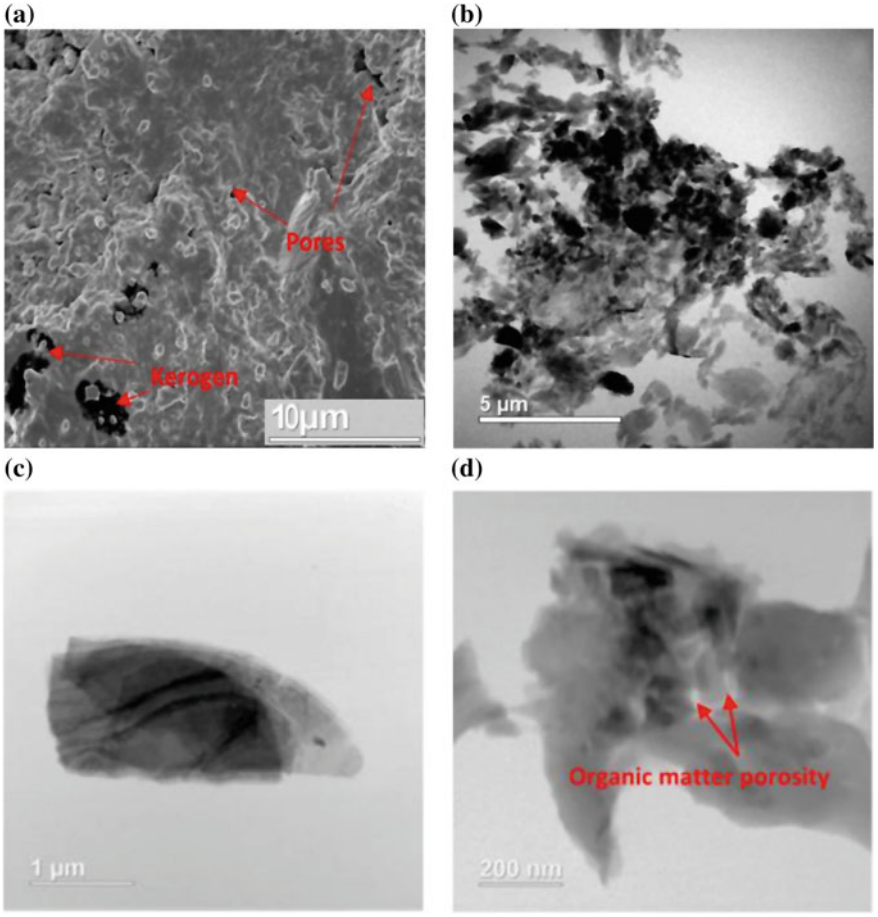

Fig. 3.1 **a** SEM images of Bakken shale sample, **b–d** STEM image of isolated kerogen at different scales

to obtain an equivalent vitrinite maturity (%VRo). This can be done by using linear Equation proposed by Jacob (1989) or converting T_{max} from Rock-Eval (Table 3.1) to %VRo through Eq. 3.2 (Jarvie et al. 2001).

$$\%VRo = \%BRo * 0.618 + 0.4 \tag{3.1}$$

$$\%VRo = 0.0180 * T_{max} - 7.16 \tag{3.2}$$

The common methods for evaluating organic matter properties are LECO, Rock-Eval pyrolysis, and organic petrography by microscopic methods. Rock-Eval (RE) pyrolysis is a universally accepted analysis in which a sample is subjected to a programmed heating (Espitalie et al. 1985; Peters 1986; Behar et al. 2001).

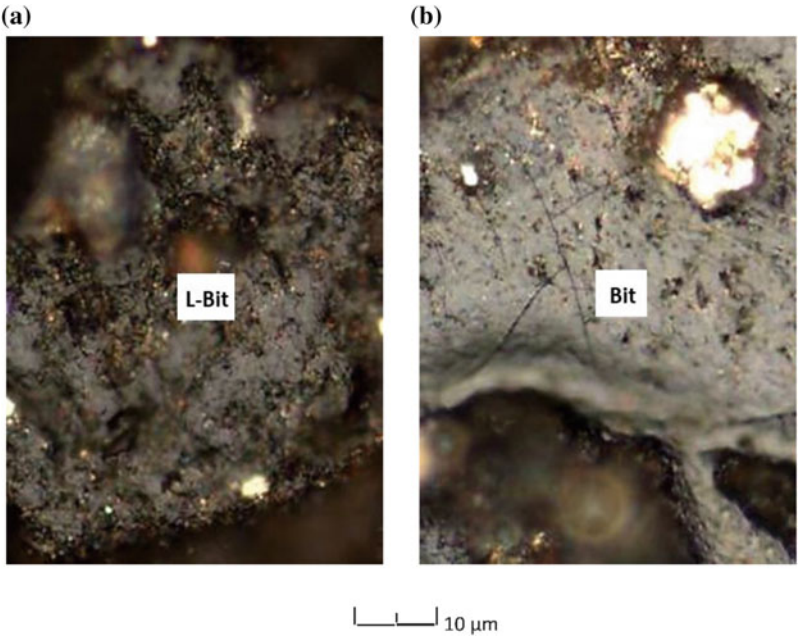

Fig. 3.2 **a**, **b** Two samples with organic matter comprises primary low-reflecting bitumen (L-B) bitumen (Bit), while no reliable grain of primary vitrinite is encountered

Table 3.1 Direct and derived parameters from Rock-Eval

Direct measurements		Derived measurements	
S1	Presents the already generated oil in the rock which will be distilled out of the sample at initial heating of the sample (350 °C)	TOC	Known as total organic carbon and is calculated as the sum of pyrolyzed OC and residual OC
S2	Presents the amount of hydrocarbon generated through thermal cracking of kerogen (550 °C). S2 is hydrocarbon which potentially will be produced	HI	Is the ratio of S_2 to TOC as a measure of the hydrogen richness of the source rock
S3	Is the trapped CO_2 released during pyrolysis (up to 390 °C) which is proportional to the oxygen presents in the kerogen	OI	Is the ratio of S_3 to TOC as a measure of the oxygen richness of the source rock

(continued)

Table 3.1 (continued)

Direct measurements		Derived measurements	
S4	Is the residual carbon content of a sample, with little or no potential to generate hydrocarbons	PI	Known as production index which is the ratio of already generated hydrocarbon (S1) to the total potential of hydrocarbon (S1 + S2). Low ratios indicate either immaturity or extreme post-mature organic matter. High ratios are interpreted as the mature stage or contamination by drilling additives or migrated hydrocarbons
T_{max}	Is the temperature at the top of the S2 peak (maximum release of hydrocarbons during pyrolysis). It is an indicator of thermal maturity	OSI	Known as oil saturation index which is the potential oil flow zones in shale reservoirs. The higher OSI, the higher chance of production. The main reason for using OSI rather than TOC for evaluating the real potential of shale oil reservoir is that OSI considers the fraction of TOC that contains moveable hydrocarbon

The Rock-Eval process results in different parameters in which some are directly measured, and some can be derived from the results (Lafargue et al. 1998; Carvajal-Ortiz and Gentzis 2015), Table 3.1.

Using parameters yield from Rock-Eval, different plots can be generated to graphically show Kerogen type, its potential to produce hydrocarbon, quality and its position in gas/oil window, such as in Fig. 3.3.

The complexity of shale plays in terms of constituent components has demonstrated that new analytical methods should be acquired to better understand hydrocarbon generation processes. One of the new methods for characterizing organic rich shales is Raman spectroscopy. Raman spectroscopy, based on molecular vibration, can provide chemical composition information of samples. Structural changes of organic matter while maturation process can be monitored by Raman spectroscopy and yields valuable information in terms of organic matter properties. In the following section, the ability of Raman spectroscopy on the characterization of organic matter is discussed.

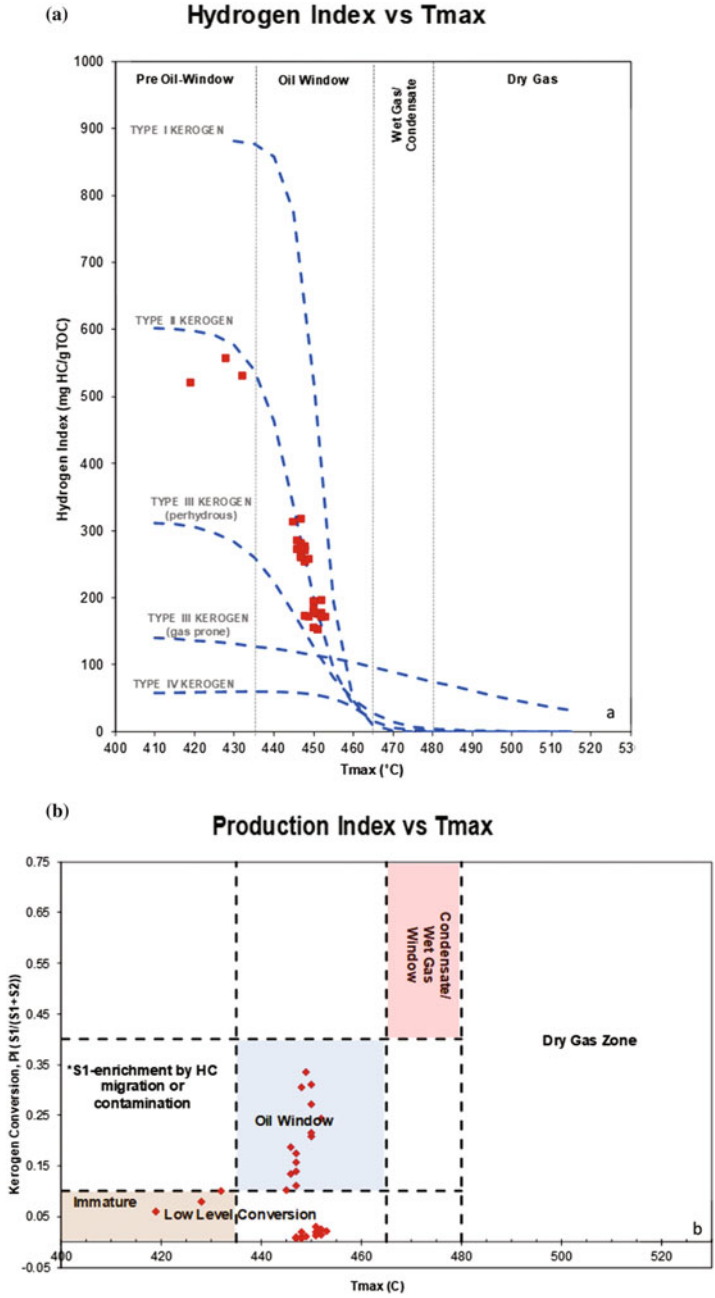

Fig. 3.3 **a** Hydrogen index versus T_{max} for kerogen type, **b** PI versus T_{max} for finding the level of kerogen conversion

3.2 Raman Spectroscopy

In Raman spectroscopy, the sample is irradiated by intense laser beams in the UV-visible region, and the scattered light is usually observed in the direction perpendicular to the incident beam. The scattered light consists of two types: one, called Rayleigh scattering, is strong and has the same frequency as the incident beam (i_f), and the other, called Raman scattering, is very weak (almost 10^{-5} of the incident beam) and has frequencies $i_f \pm m_f$, where m_f is a vibrational frequency of a molecule. Thus, in Raman spectroscopy, we measure the vibrational frequency as a shift from the incident beam frequency (Reich and Thomsen 2004; Amer 2009).

In diatomic molecules, the vibration occurs only along the chemical bond connecting the nuclei. In polyatomic molecules, the situation is complicated because all the nuclei perform their own harmonic oscillations. However, we can show that any of these complicated vibrations of a molecule can be expressed as a superposition of a number of "normal vibrations" that are completely independent of each other (Mitra 1962).

The Raman spectrum of kerogen consists of two main peaks known as G and D bands (Cesare and Maineri 1999; Marshall et al. 2010; Tuschel 2013), Fig. 3.4a. The G band refers to graphite, which appears at approximately 1600 cm^{-1} with a sharp peak. The origin of the G band is due to the inplane E_{2g2} vibrational modes of the carbon atoms in aromatic ring structures (sp^2 carbon) exhibiting D^4_{6h} symmetry (Sauerer et al. 2017). The D band refers to a disorder in the atoms which appears around 1350 cm^{-1} as a narrow peak which is a result from the Raman-active A_{1g} symmetry associated with lattice defects and discontinuities of the sp^2 carbon network (Sauerer et al. 2017; Khatibi et al. 2018). In some literature, two more minor defect bands are also detected around 1510 and 1625 cm^{-1} (Beyssac et al. 2002; Huang et al. 2010). It is worth mentioning that, Raman spectroscopy can also show the presence of other components present in organic rich shale such as Calcium carbonate, Titanium dioxide, Pyrite and Dolomite as discussed by Tuschel (2013), Fig. 3.4b, c, which is out of scope of this book.

3.3 Raman Spectroscopy for Geochemical Characterization of Shale Reservoirs

The hydrocarbon-generating potential of source rocks can be assessed by tracking physical and chemical changes in the molecular structure of kerogen through thermal maturation. Since, compared with other carbonaceous materials, the complex kerogen structure is closely related to its maturity (Khatibi et al. 2018).

By increasing maturity structural changes take place in organic matter which can be detected by Raman Spectroscopy and yield valuable information. When kerogen undergoes maturity, its aromaticity will increase which is followed by a shift in the position of the D band (as disorder band) towards lower wavelength and lower

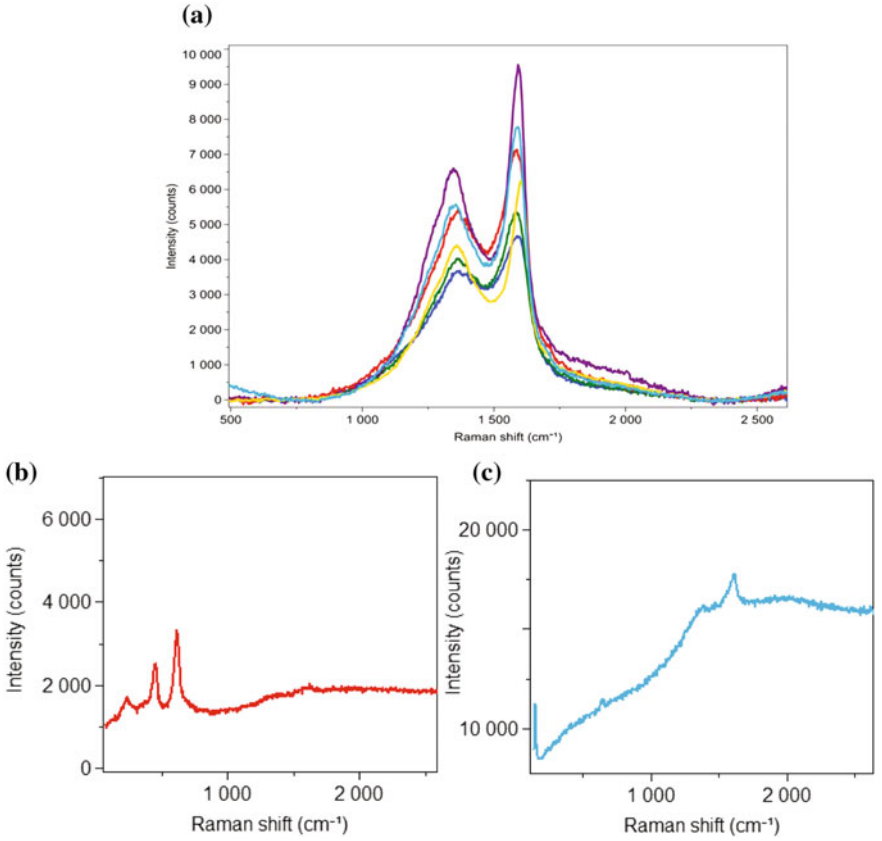

Fig. 3.4 **a** Raman spectra of six different samples with different maturity levels. Note the two major bands and also change of band position and amplitude for each sample, **b**, **c** other peaks corresponding to other components in organic rich shale

intensities. This shift is attributed to the increase of larger aromatic clusters and more ordered-structure kerogen (Schito et al. 2017; Khatibi et al. 2018). While, changes for G band position is a slight shift towards higher wavelength. This process allows for Raman to detect different levels of maturation by considering band separation (the distance between two major bands), Fig. 3.5. At initial stages of maturation, band separation increases with a higher intensity while this rapid growth tapers off over higher maturities. This might be explained by the fact that cracking of organic matter before the peak oil window is faster than the post peak oil window (Khatibi et al. 2018). Gao et al. (2017) detected abrupt changes in the structure of kerogen before the peak oil window and at the end of the oil window by the artificial maturation of oil shale kerogen. The sudden drop in HI during the peak oil window also supports the elimination of the oil potential from the kerogen residue. Consequently, after the oil window, structural changes decrease which can be reflected by the slope of line in Fig. 3.5.

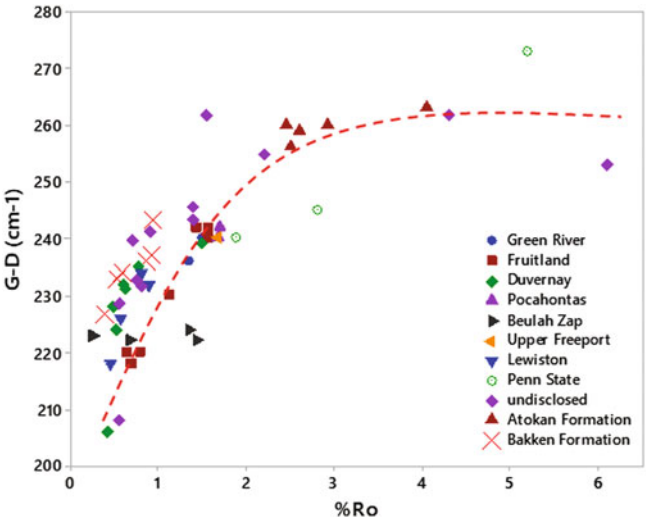

Fig. 3.5 Band separation of major Raman spectroscopy bands versus maturity for 12 different fields

Table 3.2 Average values of TOC content, vitrinite reflectance, hydrogen index, IR aliphatic carbon content, and NMR carbon aromaticity. As seen, by increasing maturity, HI and aliphatic carbon decrease, while aromaticity increases. *Source* modified from Witte et al. (1988)

TOC (wt%)	% VRo	HI (mg HC/gr rock * gr TOC)	Aliphatic carbon (mg aliph. C/gr rock)	Carbon aromaticity (from NMR)
10.56	0.48	664	47.8	0.33
7.83	0.66	642	38.5	0.43
6.16	0.88	361	22.5	0.60
5.90	1.45	74	10.1	0.80

Major molecules in kerogen are aromatics linked by aliphatic and heteroatomic moieties (Kelemen and Fang 2001) in which solid bitumen (soluble in organic solvents) may be trapped as well (Wopenka and Pasteris 1993). During hydrocarbon generation, many of the aliphatic carbon linkages are lost. The aliphatic portion of organic matter is the main contributor for hydrocarbon production (Witte et al. 1988; Schenk et al. 1986; Gao et al. 2017) which can be attributed to S2 peak in the Rock-Eval analysis which represents the potential of kerogen to produce hydrocarbons. These structural changes can be detected by different spectroscopy methods (Quirico et al. 2005). Witte et al. (1988) used Infrared Spectroscopy (IR) to show that aliphatic carbon concentrations decrease with an increase in maturity of the samples, Table 3.2. Gao et al. (2017) exposed the samples to artificial maturation and presented that mostly, CH_2 groups (aliphatic) are the contributing compound to the hydrocarbon generation using quantitative ^{13}C DP MAS NMR spectra.

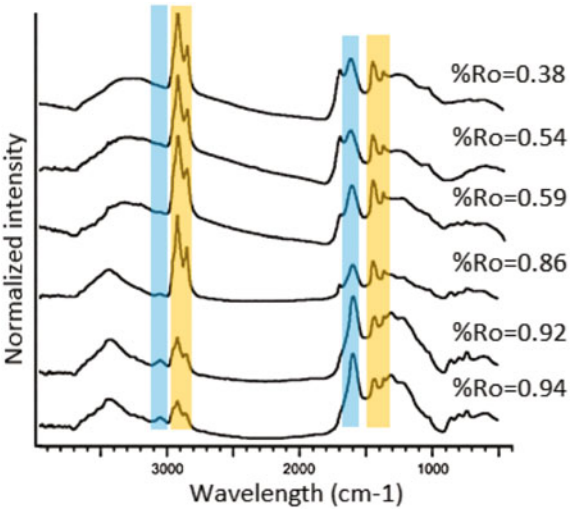

Fig. 3.6 FTIR spectra of kerogens with increasing maturity exhibit increasing aromatic absorption (blue area) and decreasing aliphatic absorption (orange area)

Fourier Transform InfraRed (FTIR), the preferred method of infrared spectroscopy, can be used to identify chemical compounds in organic materials and verify the results from the Raman spectroscopy. Figure 3.6 shows how FTIR spectra of kerogens with increasing maturity exhibit increasing aromatic absorption, decreasing aliphatic absorption for six samples with natural maturity level. Chen et al. (2015) also used micro-FTIR chemistry map of integrated peak area of aliphatic CH_x groups on Shale samples at different maturity levels (by artificial maturation procedure). They showed, in response to the increase in thermal stress, convertible carbon gradually transforms into hydrocarbons that can later be expelled from the rock, and consequently, the intensity of aliphatic groups decreases, as evidenced by the low intensity of aliphatic IR absorbance in highly mature samples.

This notable change in kerogen molecular structure and clustering of aromatics were also detected by Quirico et al. (2005) using high-resolution transmission electronic microscope (TEM). By increasing maturity, the number of stacked aromatic layers slightly increases, and onion ring microtexture will be visible for higher mature samples (Beyssac et al. 2002).

Such structural change can also be detected by Raman spectroscopy (Wang et al. 1990) and related to other properties. As mentioned before, the origin of the G band in Raman spectroscopy is because of the inplane E_{2g2} vibrational modes of the carbon atoms in aromatic ring structures (Beyssac et al. 2002, 2003; Sauerer et al 2017). The abundance of aromatic structures means less potential to produce hydrocarbon, thus, S2 from Rock-Eval can be correlated to G band from Raman spectroscopy, Fig. 3.7.

During the maturation and increase in produced hydrocarbons, the heteroatom-rich organic precursors lose many of their oxygenated and hydrogenated chemical groups (Oberlin et al. 1980; Rouzaud and Oberlin 1989) and attachments separating

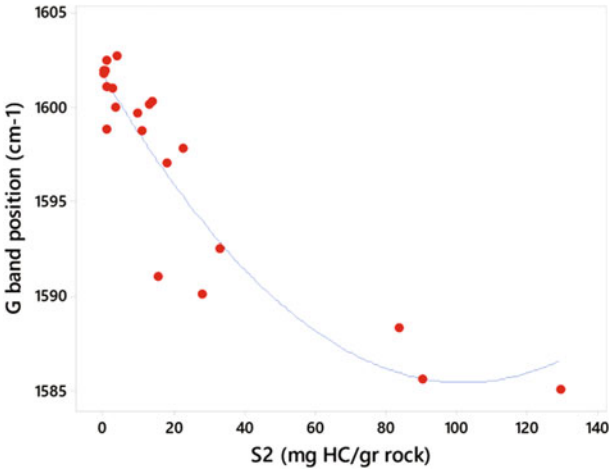

Fig. 3.7 G band position versus S2 from Rock-Eval

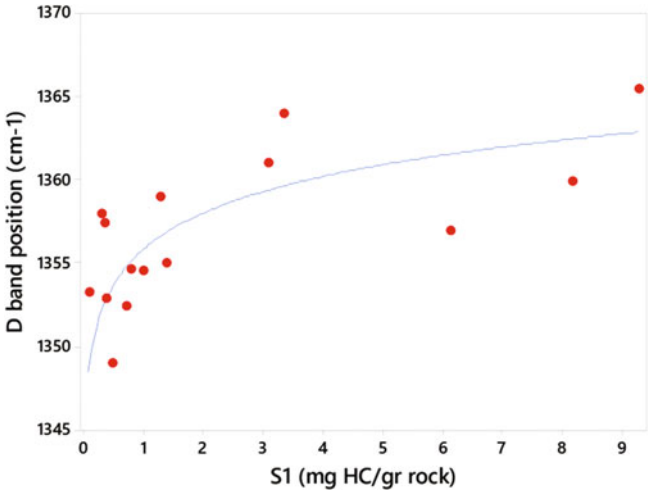

Fig. 3.8 D band position versus S1 from Rock-Eval

from aromatic carbons increases (Kelemen and Fang 2001). It was mentioned earlier that D band refers to a disorder in the atoms which is resultant from the Raman-active A_{1g} symmetry associated with in-plane lattice defects and discontinuities of the sp^2 carbon network like heteroatoms (Sauerer et al. 2017). Therefore, D band from Raman spectroscopy can be used as a measure of attachments separated from organic matter which is concurrent with hydrocarbon generation. This process can be presented by S1 peak in Rock-Eval, Fig. 3.8.

In addition to geochemical properties of organic matter, Raman spectroscopy has the potential to predict the mechanical property of organic matter in terms of Young's modulus (Khatibi et al. 2018). This method is helpful since kerogen is dispersed in the rock matrix and conventional mechanical properties measurements in literature on core samples (Aghajanpour et al. 2017) cannot be performed on organic matter.

It is believed that in immature source rock samples, the organic matter appears to surround other minerals, becoming a load-bearing part of the rock framework. However, as the maturity increases, kerogen becomes more isolated among other grains (Zargari et al. 2011; Dietrich 2015; Khatibi et al. 2018) and its Young's modulus increases. Few studies have been able to confirm this interpretation by direct measurement (Emmanuel et al. 2016; Li et al. 2017), Fig. 3.9. This phenomenon can be discussed from a molecular point of view. When maturity happens, kerogen loses heteroatoms (O, S and N) and its aliphatic carbons (hydrogen-rich groups). The residue is a hydrogen-poor structure molecule, which is dominated by aromatic carbons. During the process of maturation, which increases with burial depth, pore-walls rupture. This sequence promotes the mechanical reorientation and alignment of the aromatic units, thus will facilitate the reduction of defects (Khatibi et al. 2018). This is due to diffusion, elimination of bonding vacancies and annealing of aromatic sheets to triperiodic graphite (Bustin 1996). Therefore, from the early stages of maturation, the macromolecule arrangements transform gradually from the chaotic and mixed layers to a more ordered arrangement (Pan et al. 2013; Khatibi et al. 2018).

Considering the relationship that exists between Raman spectra versus maturity, Fig. 3.5, and Young's modulus versus maturity, Fig. 3.9, Raman data can be used

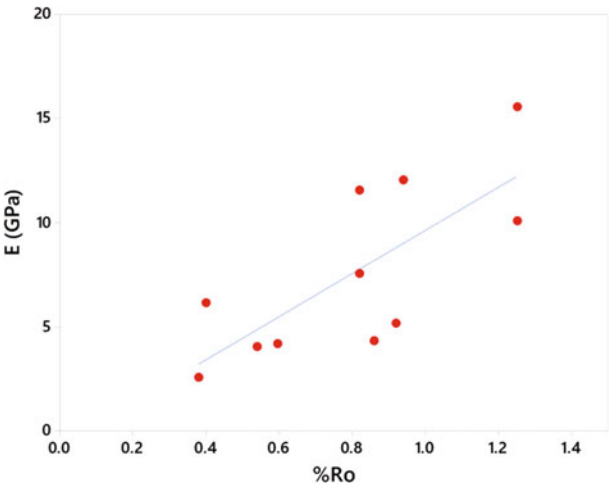

Fig. 3.9 Maturity versus Young's modulus for two different datasets. Note the general increasing trend in Young's modulus by increasing maturity

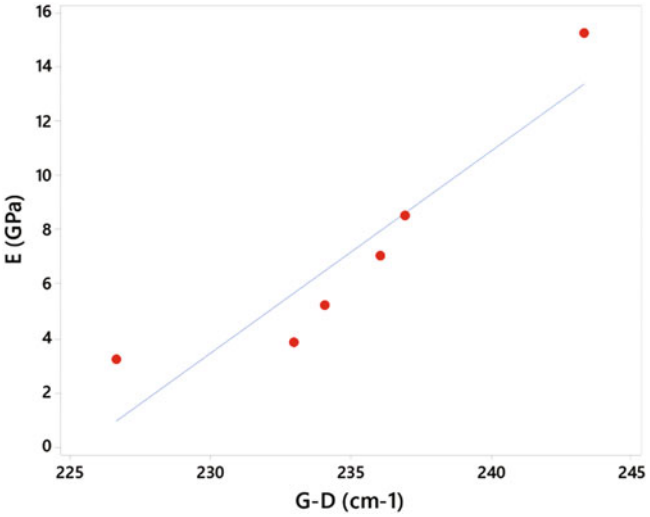

Fig. 3.10 Young's modulus versus band separation. Considering the relationship that exists between maturity and Raman spectra, and maturity with Young's modulus, Raman data can be used as an indirect method to study the mechanical properties of organic matter

as an indirect method to study the mechanical properties of organic matter (Khatibi et al. 2018), Fig. 3.10.

It was shown in Fig. 3.5 when %Ro varies from 0.3 to 3 (initial stages of maturation to the late dry gas window), band separation varies approximately between 210 and 255 cm^{-1}, respectively. Based on correlation in Fig. 3.10, Young's modulus (E) can be estimated approximately from 0.32 to 40 GPa for organic matter (Khatibi et al. 2018). This is in line with previous results by Eliyahu et al. (2015) who predicted Young's modulus of organic matter in the range of 0–25 GPa for maturities up to %Ro = 2.1.

What mentioned above was a brief introduction to different methods for characterizing organic matter and discussing employing new methods such as Raman spectroscopy in the study of shale reservoirs. High resolution for the laser focal volume of the Raman equipment (around 3 μm^3) allows for the analysis of small volumes of dispersed organic material with good precision. Furthermore, the minimal and rapid sample preparation for Raman spectroscopy enables acquiring Raman spectrum in minutes.

References

Aghajanpour A, Fallahzadeh SH, Khatibi S, Hossain MM, Kadkhodaie A (2017) Full waveform acoustic data as an aid in reducing uncertainty of mud window design in the absence of leak-off test. J Nat Gas Sci Eng 45:786–796

Amer M (2009) Raman spectroscopy for soft matter applications. Wiley, USA
Behar F, Beaumont V, Penteado HDB (2001) Rock-Eval 6 technology: performances and developments. Oil Gas Sci Technol 56:111–134
Beyssac O, Goffé B, Chopin C, Rouzaud J (2002) Raman spectra of carbonaceous material in metasediments: a new geothermometer. J Metamorph Geol 20:859–871
Beyssac O, Goffé B, Petitet J-P, Froigneux E, Moreau M, Rouzaud JN (2003) On the characterization of disordered and heterogeneous carbonaceous materials by Raman spectroscopy. Spectrochim Acta A 59(10):2267–2276
Bustin R (1996) Mechanisms of graphite formation from kerogen: experimental evidence. In: Fuel and energy abstracts. Elsevier, p 187
Carvajal-Ortiz H, Gentzis T (2015) Critical considerations when assessing hydrocarbon plays using Rock-Eval pyrolysis and organic petrology data: data quality revisited. Int J Coal Geol 152:113–122
Cesare B, Maineri C (1999) Fluid-present anatexis of metapelites at El Joyazo (SE Spain): constraints from Raman spectroscopy of graphite. Contrib Minerl Petrol 135:41–52
Chen Y, Zou C, Mastalerz M, Suyun H, Gasaway C, Tao X (2015) Applications of micro-fourier transform infrared spectroscopy (FTIR) in the geological sciences—a review. Int J Mol Sci 16 (12):30223–30250
Diessel C, Brothers R, Black P (1978) Coalification and graphitization in high-pressure schists in New Caledonia. Contrib Minerl Petrol 68:63–78
Dietrich AB (2015) The impact of organic matter on geomechanical properties and elastic anisotropy in the Vaca Muerta shale. PhD dissertation, Colorado School of Mines, Arthur Lakes Library
Eliyahu M, Emmanuel S, Day-Stirrat RJ, Macaulay CI (2015) Mechanical properties of organic matter in shales mapped at the nanometer scale. Mar Pet Geol 59:294–304
Emmanuel S, Eliyahu M, Day-Stirrat RJ, Hofmann R, Macaulay CI (2016) Impact of thermal maturation on nano-scale elastic properties of organic matter in shales. Mar Pet Geol 70:175–184
Espitalie J, Deroo G, Marquis F (1985) Rock-Eval pyrolysis and its applications. Rev De L Institut Fr Du Pet 40:563–579
Gao Y, Zou Y-R, Liang T, Peng PA (2017) Jump in the structure of type I kerogen revealed from pyrolysis and 13C DP MAS NMR. Org Geochem 112:105–118
Hackley PC, Araujo CV, Borrego AG, Bouzinos A, Cardott BJ, Cook AC, Eble C, Flores D, Gentzis T, Gonçalves PA (2015) Standardization of reflectance measurements in dispersed organic matter: results of an exercise to improve interlaboratory agreement. Mar Pet Geol 59:22–34
Huang E-P, Huang E, Yu S-C, Chen Y-H, Lee J-S, Fang J-N (2010) In situ Raman spectroscopy on kerogen at high temperatures and high pressures. Phys Chem Miner 37:593–600
Hutton A, Bharati S, Robl T (1994) Chemical and petrographic classification of kerogen/macerals. Energy Fuels 8:1478–1488
Jacob H (1989) Classification, structure, genesis and practical importance of natural solid oil bitumen ("migrabitumen"). Int J Coal Geol 11:65–79
Jarvie D, Claxton B, Henk B, Breyer J (2001) Oil and shale gas from Barnett shale, Ft. In: Worth basin, TX, poster presented at the AAPG national convention, Denver, CO
Kelemen S, Fang H (2001) Maturity trends in Raman spectra from kerogen and coal. Energy Fuels 15:653–658
Khatibi S, Ostadhassan M, Tuschel D, Gentzis T, Bubach B, Carvajal-Ortiz H (2018) Raman spectroscopy to study thermal maturity and elastic modulus of kerogen. Int J Coal Geol 185:103–118
Lafargue E, Marquis F, Pillot D (1998) Rock-Eval 6 applications in hydrocarbon exploration, production, and soil contamination studies. Rev De L'Institut Fr Du Pét 53:421–437
Li C, Ostadhassan M, Kong L (2017) Nanochemo-mechanical characterization of organic shale through AFM and EDS. In: 2017 SEG international exposition and annual meeting. Society of Exploration Geophysicists

Marshall CP, Edwards HG, Jehlicka J (2010) Understanding the application of Raman spectroscopy to the detection of traces of life. Astrobiology 10:229–243

Mitra SS (1962) Vibration spectra of solids. In: Solid state physics, vol 13. Academic Press, pp 1–80

Oberlin A, Boulmier J, Villey M (1980) Electron microscopic study of kerogen microtexture. Selected criteria for determining the evolution path and evolution stage of kerogen. In: Kerogen: Insoluble organic matter from sedimentary rocks. Editions Technip, Paris, pp 191–241

Pan J, Meng Z, Hou Q, Ju Y, Cao Y (2013) Coal strength and Young's modulus related to coal rank, compressional velocity and maceral composition. J Struct Geol 54:129–135

Peters K (1986) Guidelines for evaluating petroleum source rock using programmed pyrolysis. AAPG Bull 70:318–329

Quirico E, Rouzaud J-N, Bonal L, Montagnac G (2005) Maturation grade of coals as revealed by Raman spectroscopy: progress and problems. Spectrochim Acta Part A Mol Biomol Spectrosc 61:2368–2377

Reich S, Thomsen C (2004) Raman spectroscopy of graphite. Philos Trans R Soc Lond A Math Phys Eng Sci 362:2271–2288

Rouzaud J, Oberlin A (1989) Structure, microtexture, and optical properties of anthracene and saccharose-based carbons. Carbon 27:517–529

Sauerer B, Craddock PR, AlJohani MD, Alsamadony KL, Abdallah W (2017) Fast and accurate shale maturity determination by Raman spectroscopy measurement with minimal sample preparation. Int J Coal Geol 173:150–157

Schenk H, Witte E, Müller P, Schwochau K (1986) Infrared estimates of aliphatic kerogen carbon in sedimentary rocks. Org Geochem 10:1099–1104

Schito A, Romano C, Corrado S, Grigo D, Poe B (2017) Diagenetic thermal evolution of organic matter by Raman spectroscopy. Org Geochem 106:57–67

Tuschel D (2013) Raman spectroscopy of oil shale. Spectroscopy 28:5

Wang Y, Alsmeyer DC, McCreery RL (1990) Raman spectroscopy of carbon materials: structural basis of observed spectra. Chem Mater 2:557–563

Witte E, Schenk H, Müller P, Schwochau K (1988) Structural modifications of kerogen during natural evolution as derived from 13C CP/MAS NMR, IR spectroscopy and Rock-Eval pyrolysis of Toarcian shales. Org Geochem 13:1039–1044

Wopenka B, Pasteris JD (1993) Structural characterization of kerogens to granulite-facies graphite: applicability of Raman microprobe spectroscopy. Am Mineral 78:533–557

Zargari S, Prasad M, Mba KC, Mattson E (2011) Organic maturity, hydrous pyrolysis, and elastic property in shales. In: Canadian unconventional resources conference. Society of Petroleum Engineers

Chapter 4
Nano-mechanical Properties

Abstract With the development of production from shale oil and shale gas in North America during the last decade, more studies are being conducted in order to improve our knowledge of the shale characteristics. In this chapter, we talk about mechanical properties of shale samples in micro- and nano-scale. Nanoindentation and Atomic Force Microscopy were newly used advanced techniques in petroleum engineering to investigate the mechanical properties of shales. X-ray diffraction and energy diffusive spectroscopy were used to study the mineral compositions. Based on nanoindentation experiments, elastic modulus and hardness can be extracted from the force-displacement curve. AFM Peakforce quantitively nanomechanical mode is a relatively new mode which can produce maps of surface height and DMT modulus at the same time. In this chapter, we report the application of these two techniques on shale samples taken from Bakken Formation in Williston Basin, North Dakota.

4.1 Introduction: Why Do We Care About Mechanical Properties of Shale

After the commercial boom of shale gas and oil in North America during the past decade, exploration of unconventional shale reservoirs has been conducted in different countries with potential economic hydrocarbon reserves. With the advancements of hydraulic fracturing technology applied to enhance production from unconventional reservoirs, a great increase in oil and gas production has been experienced (Li et al. 2015). This technique often, in combination with horizontal drilling, has allowed the United States to produce economically from unconventional reservoirs.

In order to obtain shale properties, in particular, mechanical properties, core plugs are used to carry out dynamic or static type experiments at the lab scale, and the sonic logs are used to obtain the properties at larger scale representing the filed (Shukla et al. 2013). Due to chemical and mechanical instability of shales, retrieving cores or a suitable volume of samples to perform standard experiments can be challenging (Kong et al. 2018). In addition, due to the presence of various

M. Ostadhassan et al., *Fine Scale Characterization of Shale Reservoirs*,
SpringerBriefs in Petroleum Geoscience & Engineering,
https://doi.org/10.1007/978-3-319-76087-2_4

minerals in shales, such as the presence of quartz, feldspar, calcite and clay minerals, field driven elastic properties (Young's modulus, Poisson's ratio) can be erroneous.

In this chapter, we report two techniques to study the mechanical properties in micro and nano scale. This chapter were written in the following order: firstly, the principles of these two methods were illustrated, and then we report the results from a series of experiments using these two methods.

4.2 Methods: What Methods Do We Use

4.2.1 Nanoindentation

4.2.1.1 Stiffness (Young's Modulus and Hardness)

Nanoindentation is a technique which involves an indenter penetrating the sample surface, and the stiffness information such as Young's modulus and hardness of material can be obtained by measuring the penetration depth along with the applied depth. Compared to the traditional mechanical properties test experiments, this technique only requires a small sample volume.

The former Soviet Union developed the idea of depth sensing techniques and its implementation down to the nanoscale by recording load-depth diagrams for various metals and mineral since the mid-1950s. Then this technique has been developed rapidly worldwide especially after researchers found the method to explain the data from test and apply for the estimation of the mechanical properties of the materials (Doerner and Nix 1986). And nowadays nanoindentation constitutes a very powerful method to investigate the nanomechanical properties of metals, ceramics, polymers and composites (Naderi et al. 2016; Tanguy et al. 2016; Xiao et al. 2015). In recent years, researchers began to use this method in studying the mechanical properties of shale formations. Zhu et al. (2007) applied the nanoindentation method to map the mechanical properties of the natural rock in nanoscale. Delafargue (2003) and Gathier (2006) studied shale mechanical properties in multiscale and homogenized their strength to derive their strength in big scale. Bobko (2008) used nanoindentation method in shale studies and found the link between mineral compositions. But all their studies are just the ordinary sedimentary shale rock not the shale reservoir rocks. Alstadt et al. (2015) analyzed the morphology of kerogen and the nanomechanical properties of green river oil shale in different orientations (parallel and perpendicular to the bedding plane). Mason and Kuma studied the effect of mineralogy and organic matter on mechanical properties of shale (Kumar et al. 2012; Mason et al. 2014; Shukla et al. 2013), however, they limited their studies only in measuring Young's modulus and hardness. Nanoindentation technique shows promising applications to estimate the mechanical properties in different medium types. In petroleum and civil

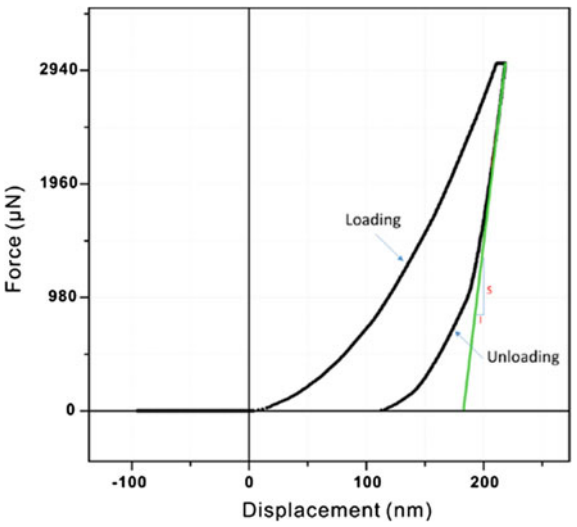

Fig. 4.1 Typical load-displacement curve derived from nanoindentation

engineering, many researchers have applied the nanoindentation method to study shale properties (Kumar et al. 2012; Mason et al. 2014).

The indentation modulus E_r and hardness H are calculated by the Oliver and Pharr method (Oliver and Pharr 1992):

$$E_r = \frac{\sqrt{\pi}}{2}\frac{S}{\sqrt{A_c}} \tag{4.1}$$

$$H = \frac{P}{A_c} \tag{4.2}$$

$$\frac{1}{E_r} = \frac{1-v^2}{E} + \frac{1-v_i^2}{E_i} \tag{4.3}$$

where P is the measured maximum indentation load, A_c is the projected contact area, and S is the unloading indentation stiffness which is quantified as the slope of the upper portion of the unloading curve (Fig. 4.1):

$$S = \left(\frac{dP}{dh}\right)_{h=h_{max}} \tag{4.4}$$

4.2.1.2 Fracture Toughness

There is a significant growth in the number of researchers who are using nanoindentation methods to study fracture toughness for its accurate and repeatable measurement (Kruzic et al. 2009; Scholz et al. 2004; Sebastiani et al. 2015; Wang

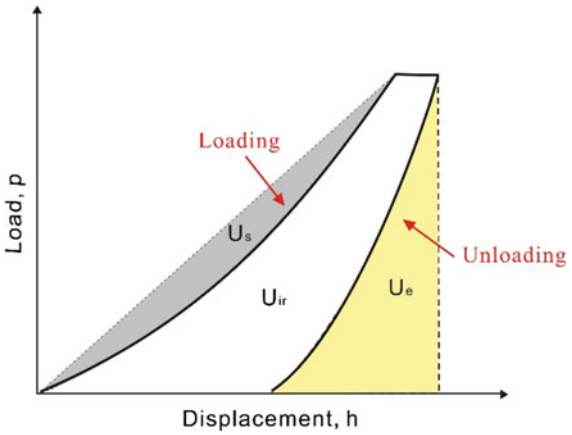

Fig. 4.2 Schematic illustration of the energy analysis for calculation purpose

et al. 2015), whereas using nanoindentation method to study the fracture toughness of rocks is very scarce to date. In this chapter, we acquired nanoindentation technique to study the fracture toughness of shale samples from the Bakken Formation. Due to the inhomogeneous nature of the samples and the different in measuring the crack length during the nanoindentation process, we applied energy analysis method in this study (Fig. 4.2). The theoretical concept behind the energy analysis method is that the irreversible energy (U_{ir}) can be defined as the difference of the total energy (U_t) and the elastic energy (U_e) (Cheng et al. 2002). Then fracture energy (U_{crack}) can be described using the following equation:

$$U_{crack} = U_{ir} - U_{PP} \tag{4.5}$$

In this equation U_{PP} is the energy cost due to the pure plasticity which can be calculated using the following mathematical relationship:

$$\frac{U_{PP}}{U_t} = 1 - \left[\frac{1 - 3\left(\frac{h_f}{h_{max}}\right)^2 + 2\left(\frac{h_f}{h_{max}}\right)^3}{1 - \left(\frac{h_f}{h_{max}}\right)^2} \right] \tag{4.6}$$

Therefore the critical energy release rate G_c can then be determined as:

$$G_c = \frac{\partial U_{crack}}{\partial A} = \frac{U_{crack}}{A_m} \tag{4.7}$$

where A_m is the maximum crack area. For Berkovich indenter, the area can be calculated as:

$$A_{max} = 24.5h_{max}^2 \tag{4.8}$$

Finally, the fracture stress intensity factor K_c can be computed as:

$$K_C = \sqrt{G_C E_r} \tag{4.9}$$

4.2.1.3 Creep

Creep is a term to describe the time-dependent behavior of the rocks under constant but long-time exposure to stress that is still below their yield strength. Creep happens due to the viscoelastic properties of rocks. Based on the study by Heap et al. (2009), the creep in rocks can be divided into three stages: (1) primary or decelerating stage; (2) secondary or stationary stage; (3) tertiary or accelerating stage. Uniaxial creep test and multistage triaxial creep experiments are the common laboratory testing methods that researchers perform to study the creep behavior (Li and Ghassemi 2012; Sone and Zoback 2014). These types of studies are limited in analyzing the creep behavior at macroscale and need large sample volumes, which are sometimes not practical to obtain especially from shale formations due to coring issues. Shale is known to be a fine-grained sedimentary rock consisting of a mixture of minerals (clay, quartz, feldspar, pyrite and carbonates) and organic matter, forming a highly heterogeneous nanocomposite (Ulm et al. 2007), while each of these components shows different creep behavior. Understanding the deformation that occurs when shale undergoes creep at the nano scale can provide an insight into the fundamental processes governing on this phenomenon at a larger scale for example when shale is as a cap rock and should exhibit a ductile deformation.

4.2.2 AFM PeakForce QNM

Atomic force microscopy (AFM) was extensively used in material science. The PeakForce Quantative Nano-mechanical Mapping (PeakForce QNM) mode of AFM is a relatively new mode which can produce height images and quantitative nano-mechanical map at the same time. This new mode was very popular in characterizing polymer, biological material and so on. In this mode, z piezo is used to control the probe, z piezo pushes probe towards surface until the PeakForce setpoint is reached and probe starts withdrawing from sample and then breaks free off sample at maximum adhesion point. While the probe scanning the surface of sample, the deflection of the cantilever is measured to produce a Force-Distance (FD) curve, and properties such as height sensor, DMT modulus, deformation and dissipation can be calculated from the FD curve (Fig. 4.3).

In AFM quantitative nano-mechanical mapping, cantilever with appropriate spring constant should be selected to get accurate measurement. Most of the

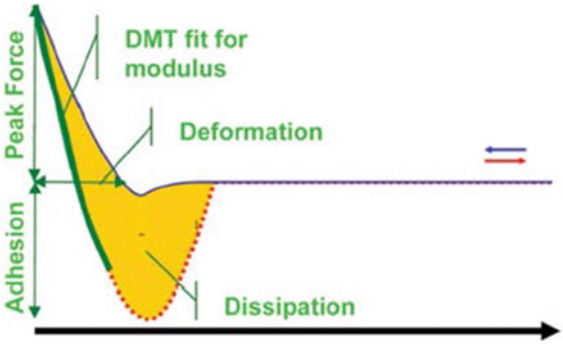

Fig. 4.3 Schematic force-distance curve

literature value of Young's modulus of organic matter in shales are under 20 GPa. Based on this, we choose tip RTESPA-525 (spring constant, k ~ 200 Nm^{-1}; Etip = 310 Nm^{-1}) which is optimal in measuring material with Young's modulus ranging 0–20 GPa in this study. For calibration the probe, a relative way is used: a ramp was firstly run on a stiff sapphire standard to measure the deflection sensitivity; secondly a highly-ordered pyrolytic graphite standard (HOPG) with the elastic modulus of 18 GPa was used for the calibration of the radius of the probe The reason to choose HOPG as calibration is because its similar stiffness with organic matter in shales. A spring constant k ~ 200 Nm^{-1} (based on the manual value) was used and then adjust the tip radius until a DMT modulus about 18 GPa was measured. After the calibration, a scan of 100 μm × 100 μm was carried out at a resolution of 256 × 256 pixels at 0.2 Hz on a shale sample.

The objective scan area was first found under the SEM image and then the pyrite and edge of the sample was used as mark to find the same location for AFM test.

4.3 Results and Discussion

4.3.1 Nano-indentation Curves Analysis

Figure 4.4 depicts some typical nanoindentation curves obtained from the tested samples. All the curves in Fig. 4.4 show the elastic plastic deformation during the loading process. Figure 4.4a illustrates the typical indentation curve without any abnormal phenomenon. From Fig. 4.4b, it is evident that the loading curve shows a normal pattern. However, the unloading curve follows an elbow pattern. The pressure beneath the indenter is very high and always increases as the indentation depth increases. Once the hydrostatic pressure is larger than the critical point, phase transformation occurs (Tabor 1978). The gradual change of the unloading curve is the result of the material expansion during the slow transformation to the amorphous phase, which contributes to the indenter uplift (Domnich et al. 2000). Figure 4.4c shows the "pop in" phenomena in the loading curve. This is interpreted

due to the cracks forming during the nanoindentation process. When the indenter contacts the material, the work by the indenter will change the elastic energy of the material once the elastic energy increases to a critical value at some point in the contact field, plastic deformation occurs with the increasing load. For the elastic plastic materials such as rocks, their elastic energy is almost invariant within the localized plastic deformation zones. However, rocks which are just exterior to this zone and in a state of incipient plastic deformation have less elastic energy and the elastic energy decreases significantly as the distance from the contact zone increases. The large energy difference in different zones can lead to the formation of the cracks (Cook and Pharr 1990; Lawn et al. 1980; Oyen and Cook 2009). Figure 4.4d shows combinations of "pop in" and "elbow" phenomena. The parameters of curve fitting to the loading and unloading stages of Fig. 4.4a–d are calculated respectively and reported in Table 4.1. The results explain that the loading and unloading curves fit the power law functions listed below very well:

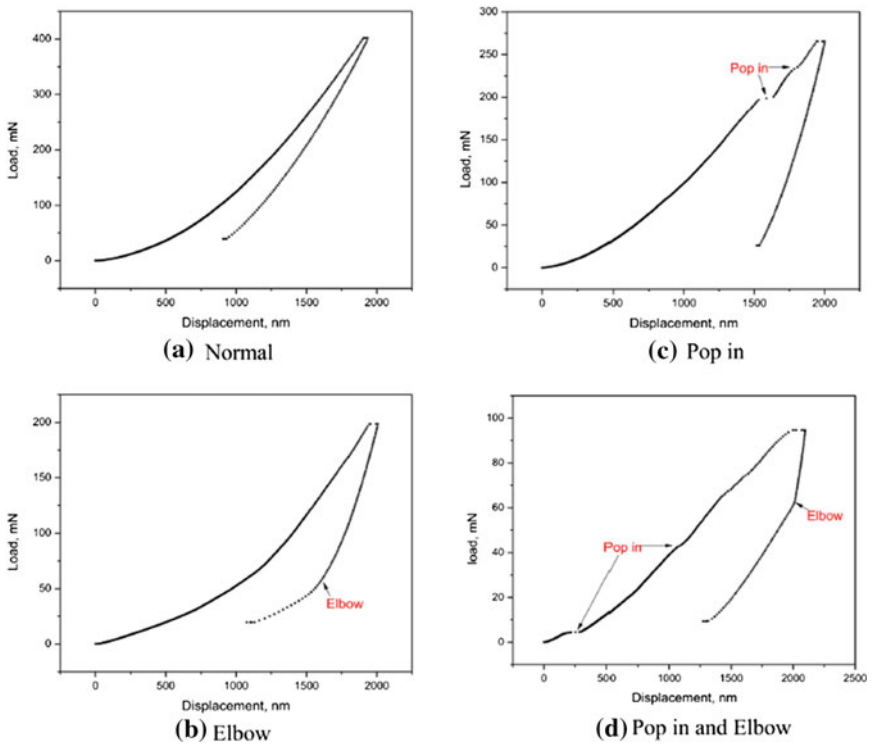

Fig. 4.4 Typical nanoindentation curves identified

Table 4.1 Curving fitting analysis of the loading and unloading process, respectively

	K	n	R^2
Loading process			
a	0.00048	1.80591	0.99992
b	0.00013	1.87968	0.99586
c	0.00265	1.52325	0.99848
d	0.02687	1.15039	0.96086
	α	m	R^2
Unloading process			
a	0.07906	1.22777	0.99450
b	0.0049	1.50995	0.99044
c	0.14466	1.21866	0.99238
d	0.00597	1.62741	0.98771

$$\begin{aligned} P &= Kh^n \quad \text{(loading)} \\ P &= \alpha(h - h_f)^m \quad \text{(unloading)} \end{aligned} \tag{4.10}$$

Where P and h are the loading force and displacement, respectively. hf is the residual displacement. K, n, α and m are constants which can be calculated based on the experiments. This is a similar behavior observed in other materials (Lawn et al. 1980), proving that the theory of nanoindentation may be used for the calculation of rock mechanical properties.

4.3.2 *Stiffness (Young's Modulus, Hardness)*

Young's modulus and hardness of the samples were calculated by the Oliver and Pharr method which mentioned in the previous section, and their values were plotted versus the penetration depth as shown in Fig. 4.5. This figure represents the results of a sample for calculating Young's modulus. From this figure, it is concluded that both plots adhere three distinguished stages. During the initial stage, we can assume that the contact is elastic, which means that the values of this stage are the mean values and less than the real mechanical value of the materials. At larger penetration depth, the influence of the substrate on the test values will become more pronounced as is visible from the third stage in the figure, so the hardness value extracted from the plateau stage will be considered as the real hardness value of the sample. For the Young's modulus we use the extrapolation technique (see Fig. 4.5b). We extended the plot from the second stage to the sample surface (i.e. when displacement equals to 0), and where the vertical axis intercept the graph, Young's modulus of the samples is read (Fischer-Cripps 2006). Following this procedure, for this test point in this sample, its hardness value is obtained to be 13.8 GPa and Young's modulus equal to 95 GPa.

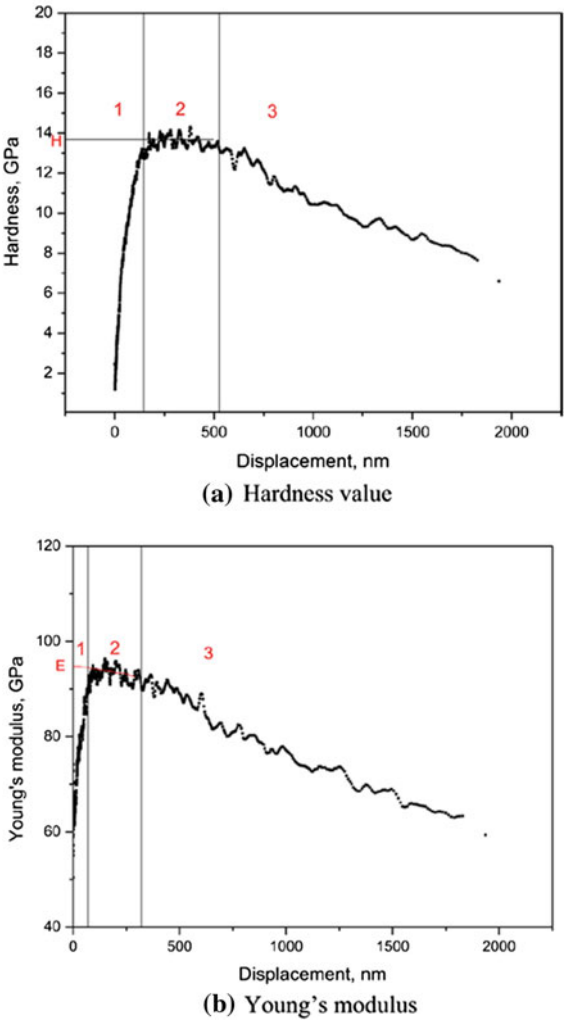

Fig. 4.5 Changes of elastic modulus and hardness versus penetration depth. Both plots show three distinguished stages: 1. initial rising; 2. plateau; 3. falling off

Based on a large number of indents of each sample, we calculated the Young's modulus and the hardness value of each sample. Figure 4.6 shows the elastic modulus and hardness values of the four samples we tested. The mineralogy informationed is shown in Table 4.2. Sample 1 is from Upper Bakken Formation while sample 2, 3 and sample 4 are from Middle Bakken Formation. The data shows that sample 4 has the highest elastic modulus while sample 3 has the lowest values.

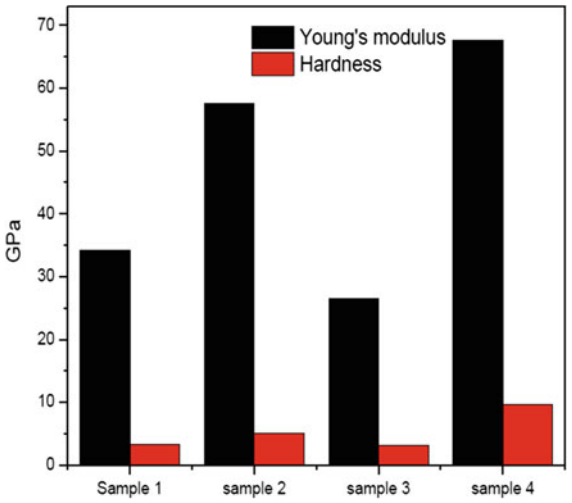

Fig. 4.6 Elastic properties of different samples

Table 4.2 Composition analysis of XRD

	Sample 1	Sample 2	Sample 3	Sample 4
Quartz	31.9	35.8	37.9	49.4
Calcite	0	2.5	2.6	1.7
Dolomite	12	0.1	0.3	2
Ankerite	0	4	6.3	3.4
Pyrite	0	3.6	5	4.8
K-feldspar	4.7	11.2	8.7	9.8
Albite	0	7.6	5.1	3.7
Clay minerals	51.3	35.2	34	25.2

4.3.3 Fracture Toughness of Shale

Based on the energy analysis method, nanoindentation tests were performed on four different samples from three members of the Bakken Formation. Figure 4.7a depicts the results of the contact stiffness, reduced modulus and Young's modulus. From this figure, it is seen that the higher contact stiffness, the higher the Young's modulus is. This is because the contact stiffness is the value of the slope of the nanoindentation curve at hmax. Elastic energy increases as the S increases. So Young's modulus which can reflect the elastic properties of rocks also increases as shown in Figs. 4.7b and 4.8 presents the energy distribution corresponding to each nanoindentation test. Figure 4.7c depicts the results of the energy release rate and fracture intensity factor of the nanoindentation tests, showing the fracture toughness increases and the energy release rate increases. The average value of K_{IC} for the samples from the Bakken in nanoscale is around 3.06 MPam. Plotting the Young's modulus versus the toughness values for the samples, a linear relationship is

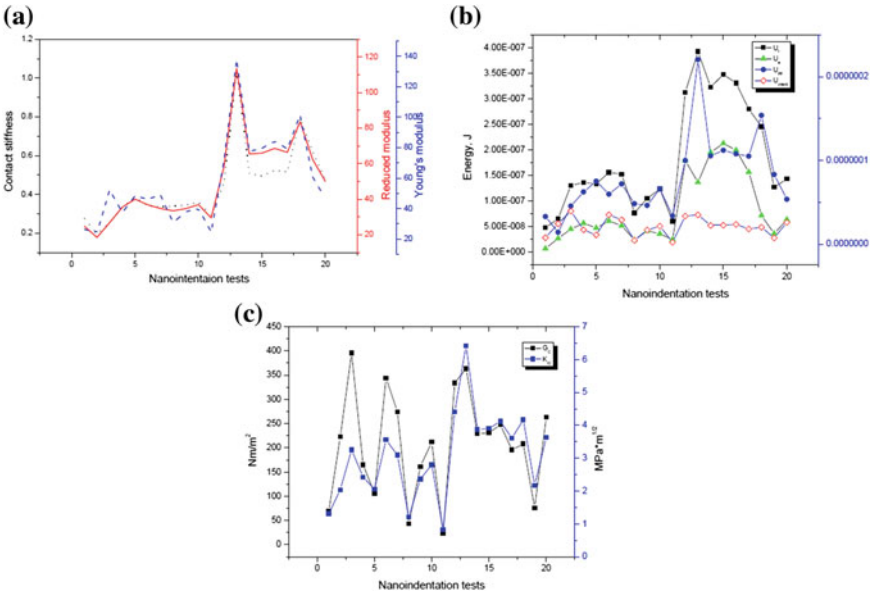

Fig. 4.7 Energy analysis results from nanoindentation. **a** contact stiffness, reduced modulus and Young's modulus; **b** total energy, plastic energy, elastic energy and crack energy; **c** energy release rate and fracture intensity fractor

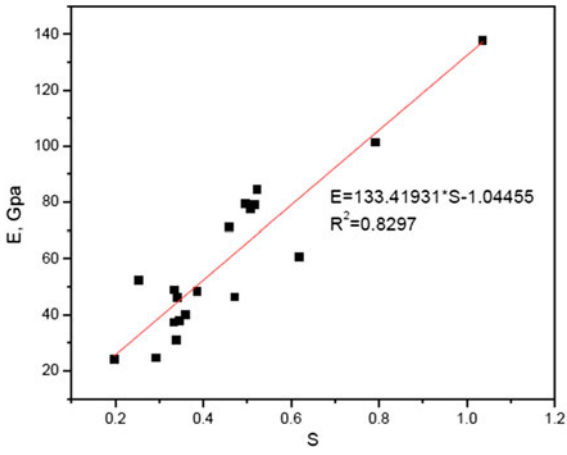

Fig. 4.8 Relationships between contact stiffness and Young's modulus

developed at the nanoscale as shown in Fig. 4.9. The following equation allows us to estimate the fracture toughness from Young's modulus at nanoscale:

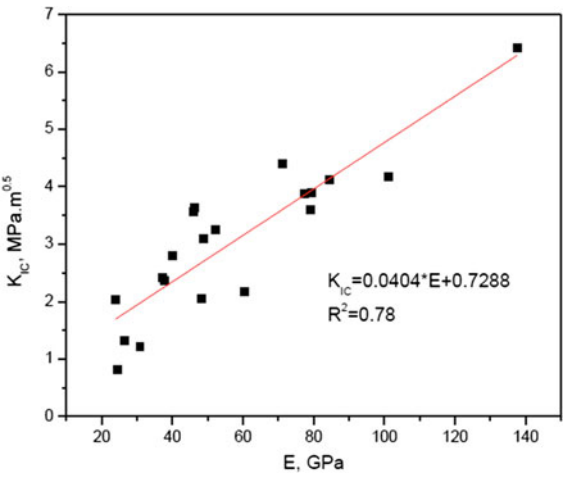

Fig. 4.9 Relationships between Young's modulus and fracture toughness

$$K_{IC} = 0.7288 + 0.04048t \tag{4.11}$$

This equation shows that as Young's modulus increases, the fracture toughness increases. This is due to the increase of the Young's modulus can increase the ultimate fracture strengths (Yuan and Xi 2011) thus enhancing the ability to resist fracture. The values of fracture toughness of Bakken formation rocks are rarely to be found in the literature while the information of elastic modulus is abundant and easily to be derived. Equation (4.11) gives us a potential estimation of the fracture toughness of Bakken formation without using big scale samples, making more profits.

4.3.4 *Creep Analysis by Nano-indentation*

Shales are composed of various minerals with different mechanical properties. Thus, the creep behavior of each mechanical phase might be different under the same stress conditions and time. In order to better investigate and attain a deeper insight into the creep behavior of shales at the nanoscale, we chose three points from the grid indents for more detailed analysis. Table 4.3 summarizes the information about these three data points where Points 1, 2 and 3, respectively, represent

Table 4.3 Summary of the mechanical properties of the three points

Points	Complex modulus (GPa)	Hardness (GPa)
Point 1	16.71	0.77
Point 2	38.45	2.69
Point 3	56.70	6.82

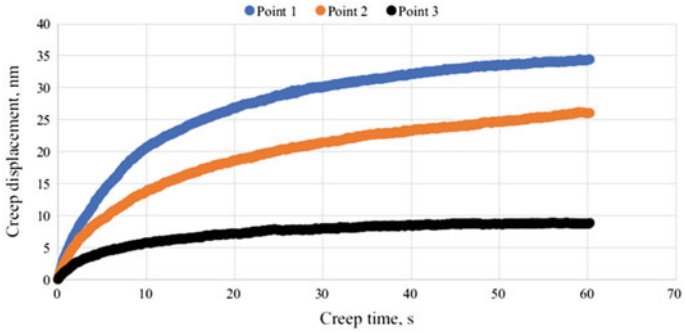

Fig. 4.10 Correlations between creep and displacement and creep time

Table 4.4 Constants and regression coefficients corresponding to the three points logarithmic functions

	a	*b*	*c*	R^2
Point 1	8.7913	0.7797	−0.5695	0.9919
Point 2	7.4478	1.8052	−4.5319	0.9990
Point 3	1.9998	0.4221	0.9926	0.9898

soft minerals, medium hard minerals and hard minerals. These data points are chosen based on their complex modulus and hardness values.

When plotting the displacement recorded for these three data points as a function of creep time, it can be found that the curve follows a similar trend in all data points (Fig. 4.10). In the beginning, creep displacement is rapidly increasing and then slows down over time. Under the same creep time, the mineral with a larger complex modulus and hardness showed less creep displacement. A curve fitting technique was used to quantify the changes in displacement, while the sample is under creep. The results are summarized in Table 4.4, indicating that all three creep curves follow a logarithmic function which is similar to conclusions in previous studies (Vandamme and Ulm 2009; Wu et al. 2011). The equation for the logarithmic function was found in the following format:

$$y = a\ln(t + b) + c \tag{4.12}$$

where y is creep displacement (nm); t is creep time (s); a, b, c are the constants derived from curve fitting. a is an important parameter that can be used to characterize creep behavior. The curve with higher a value would express a larger creep displacement. We further analyzed the impact of creep time on the mechanical and

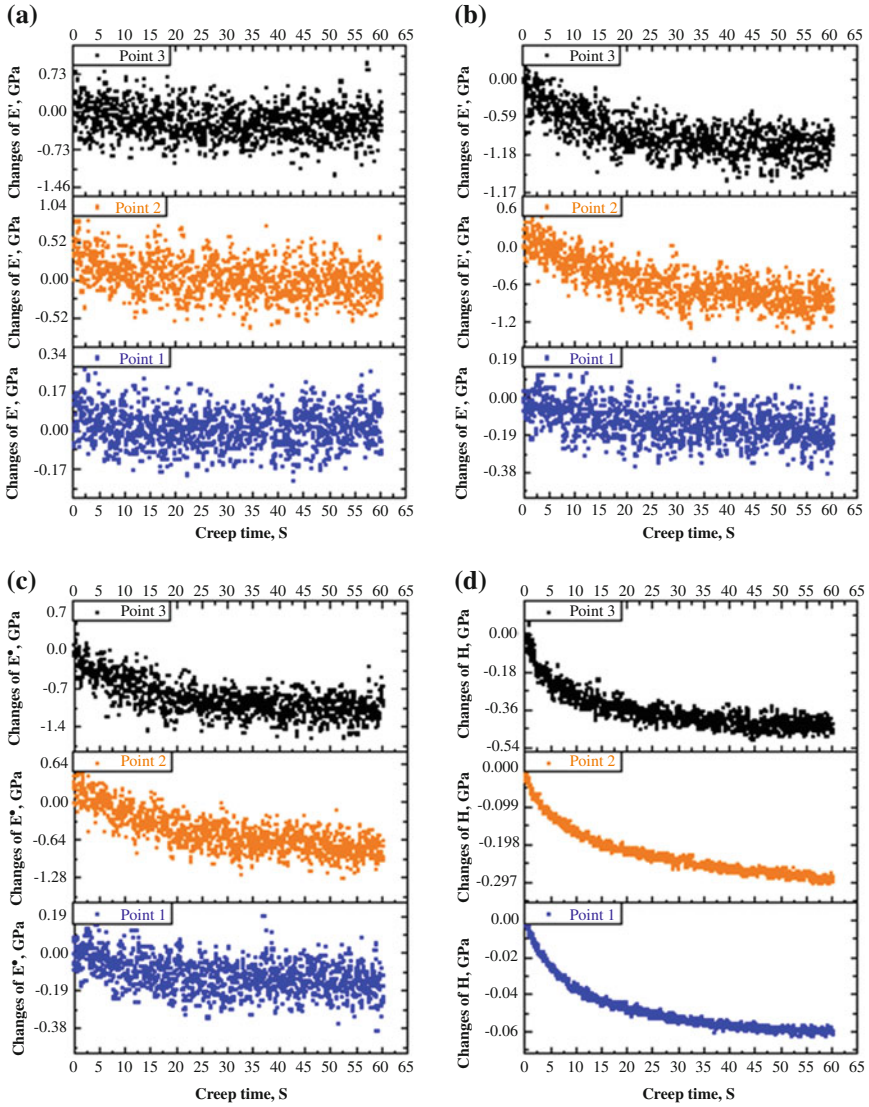

Fig. 4.11 Changes of the mechanical properties as a function of creep time: **a** loss modulus, **b** storage modulus, **c** complex modulus, **d** hardness

viscoelastic properties of these chosen data points. As creep time increases, loss modulus fluctuates around 0 without any distinguishable relationship between the loss modulus and creep time (Fig. 4.11a). However, considering other properties such as the storage modulus, complex modulus and hardness, as creep time evolves, the changes in these values increase (Fig. 4.11b–d). Figure 4.11b explains that variations in Point 1 which are measurements on a soft mineral are smaller

Table 4.5 Curve fitting results of the storage modulus, complex modulus and hardness

Properties	Points	*a*	*b*	*c*	R^2
Storage modulus	Point 1	−0.0564	4.1846	0.0632	0.1897
	Point 2	−0.4052	4.0786	0.7970	0.6508
	Point 3	−0.2797	1.1977	0.0431	0.5404
Complex modulus	Point 1	−0.0465	1.4891	0.0420	0.1966
	Point 2	−0.3936	2.9837	0.8041	0.6829
	Point 3	−0.2807	0.8335	0.0398	0.5587
Hardness	Point 1	−0.0148	0.5906	−0.0016	0.9834
	Point 2	−0.0724	1.1333	0.0077	0.9864
	Point 3	−0.0907	0.1919	−0.0782	0.8775

compared to Point 2 and Point 3 from medium hard and hard minerals, respectively. We applied the similar curve fitting method from earlier for the displacement, to quantify the changes in mechanical properties during creep time. Table 4.5 illustrates that Eq. 4.12 can also describe the effects of creep time on mechanical properties.

4.3.5 *Elastic Properties of Organic Matter by AFM*

Coupled with the SEM and EDS images (Figs. 4.12 and 4.13), it can be seen that the main phases including in the scanning area samples are clays and organic matter, with minor calcite and pyrite. In SEM BSE images, the organic matter represents as dark and grey dark; clays are grey; pyrite represents as white light spot; calcite is hard to identify through SEM-BSE image. In EDS, the phases identification can be double checked with the specific elements maps: organic

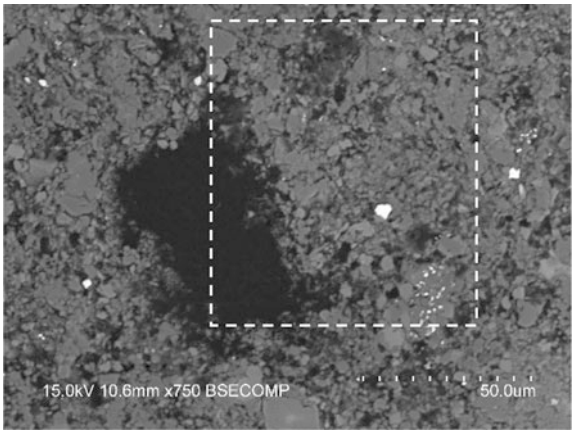

Fig. 4.12 SEM-BSE images of sample, the area in white-dashed frame is the same scan location with EDS and AFM

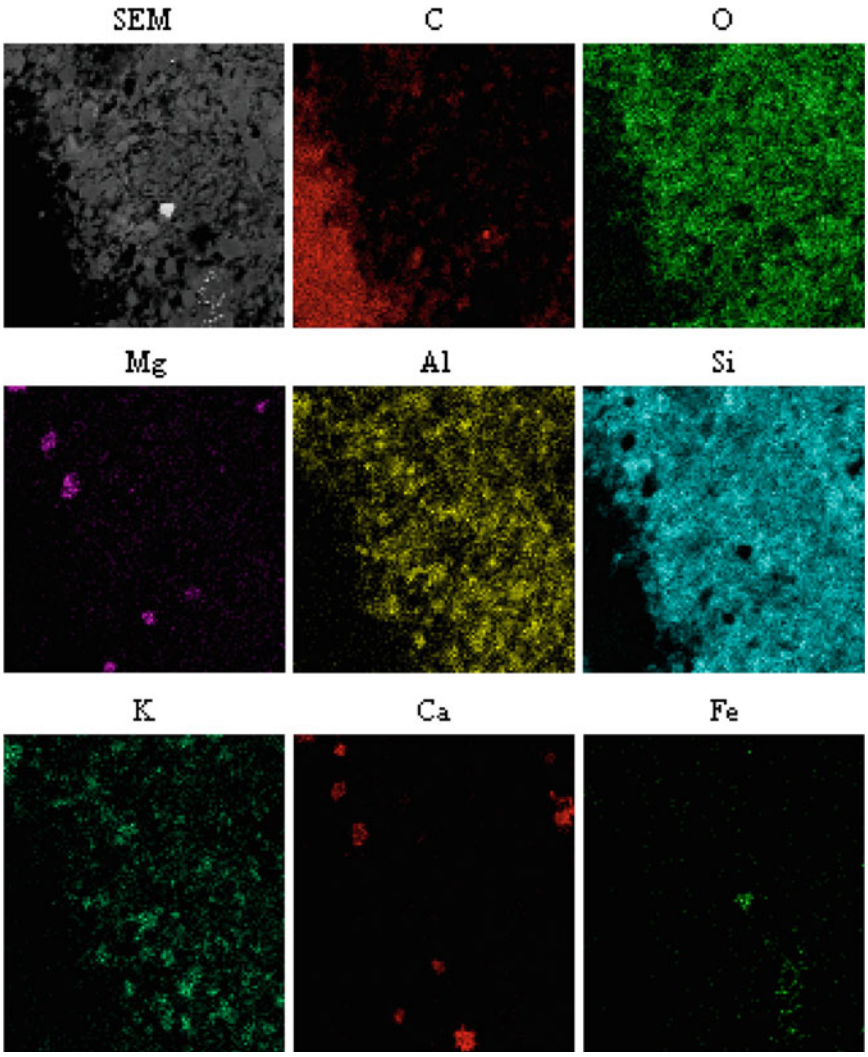

Fig. 4.13 EDS elemental mapping for scan area

matter corresponds to the C, clays to the O, Al and Si, calcite to Ca and Mg (Fig. 4.14).

The results show that the elastic modulus of organic matter in shale between 2 and 6 GPa (Li et al. 2017). Organic matter in shale can be either kerogen or solid bitumen. Kerogen can be identified by isolated particle surrounded by tightly packed small grains while bitumen has fracture-filling characteristics, occupying the inter-particle voids. Moreover, the solid bitumen can also be genetically classified into two type: pre-oil solid bitumen (early immature generation products of rich

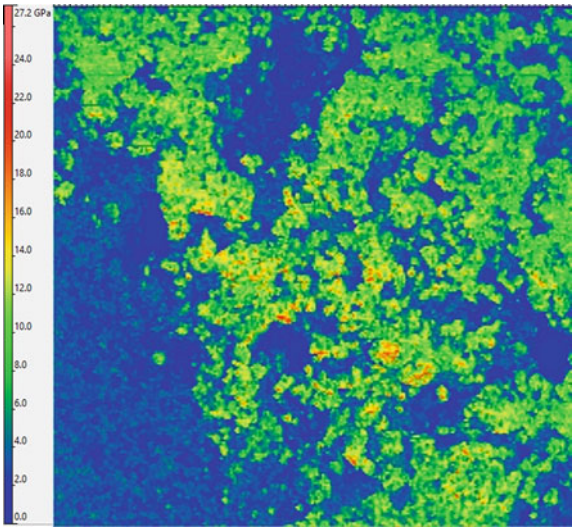

Fig. 4.14 Young's modulus map

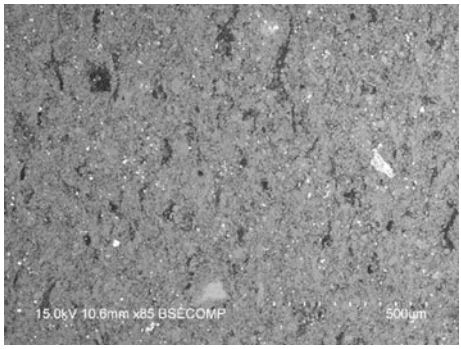

Fig. 4.15 SEM-BSE images (dark part is pre-oil bitumen)

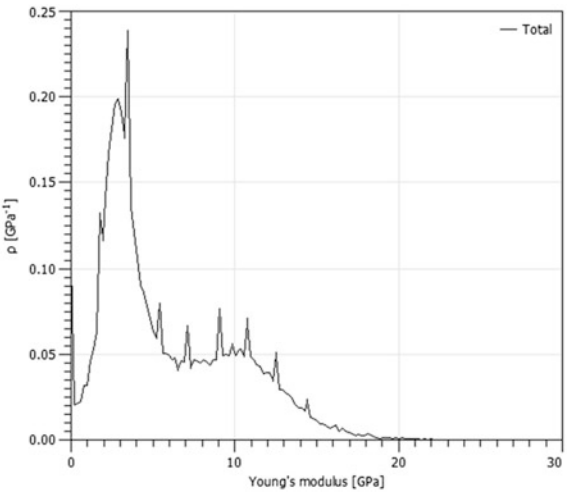

Fig. 4.16 PDF plot of Yong's modulus

source rocks, the intermediate product between kerogen and oil) and post-oil solid bitumen (migrating residue of once-liquid oil) (Curiale 1986). The depth of the sample is 8326 ft, which is located in immature section in Willison Basin, and based on the shape of the dark part in SEM-BSE image (Fig. 4.15), the organic matter in the sample could be identified as pre-oil solid bitumen. The probability density functions plot (Fig. 4.16) shows two distinctive peaks at 3 and 11 GPa, which corresponds to the pre-oil bitumen and clays. From literature, a relative wide range of values were reported: Eliyahu et al. (2015) found value range from 0 to 25 GPa for organic component, with specific scan showed 2 GPa for bitumen, while Zargari et al. (2013) also reported value of 2 GPa for extruded bitumen in Bakken shale.

It is shown from the PDF plot, a sharp peak can be seen for organic matter because of uniform values of elastic modulus which means that the bitumen in this sample is homogeneous in mechanical property, while the clays correspond to a wide peak, representing a relative heterogeneous structure.

References

Alstadt KN, Katti KS, Katti DR (2015) Nanoscale morphology of kerogen and in situ nanomechanical properties of Green River Oil shale. J Nanomech Micromech 6(1):04015003

Bobko CP (2008) Assessing the mechanical microstructure of shale by nanoindentation: the link between mineral composition and mechanical properties. PhD thesis

Cheng Y-T, Li Z, Cheng C-M (2002) Scaling relationships for indentation measurements. Philos Mag A 82(10):1821–1829

Cook RF, Pharr GM (1990) Direct observation and analysis of indentation cracking in glasses and ceramics. J Am Ceram Soc 73(4):787–817

Curiale JA (1986) Origin of solid bitumens, with emphasis on biological marker results. Org Geochem 10:559–580

Delafargue A (2003) Material invariant properties of shales: nanoindentation and micro poroelastic analysis. Master thesis

Doerner MF, Nix WD (1986) A method for interpreting the data from depth sensing indentation instruments. J Mater Res 1(4):601–609

Domnich V, Gogotsi Y, Dub S (2000) Effect of phase transformations on the shape of the unloading curve in the nanoindentation of silicon. Appl Phys Lett 76(16):2214–2216

Eliyahu M, Emmanuel S, Day-Stirrat RJ, Macaulay CI (2015) Mechanical properties of organic matter in shales mapped at the nanometer scale. Mar Pet Geol 59:294–304

Fischer-Cripps AC (2006) Critical review of analysis and interpretation of nanoindentation test data. Surf Coat Technol 200(14–15):4153–4165

Gathier B (2006) Multiscale strength homogenization—application to shale nanoindentation. Master thesis

Heap MJ, Baud P, Meredith PG et al (2009) Time-dependent brittle creep in Darley Dale sandstone. J Geophys Res Sol Earth 114(B07203):1–22

Kong L, Ostadhassan M, Li C, Tamimi N (2018) Pore characterization of 3D-printed gypsum rocks: a comprehensive approach. J Mater Sci 53(7):5063–5078

Kruzic JJ, Kim DK, Koester KJ, Ritchie RO (2009) Indentation techniques for evaluating the fracture toughness of biomaterials and hard tissues. J Mech Behav Biomed Mater 2(4):384–395

Kumar V, Curtis ME, Gupta N, Sondergeld CH, Rai CS (2012) Estimation of elastic properties of organic matter in Woodford shale through nanoindentation measurements. Society of Petroleum Engineers

Lawn BR, Evans AG, Marshall DB (1980) Elastic/plastic indentation damage in ceramics: the median/radial crack system. J Am Ceram Soc 63(9–10):574–581

Li C, Ostadhassan M, Kong L (2017) Nanochemo-mechanical characterization of organic shale through AFM and EDS. In: SEG International Exposition and Annual Meeting, Society of Exploration Geophysicists, 2017, October

Li Q, Xing H, Liu J, Liu X (2015) A review on hydraulic fracturing of unconventional reservoir. Petroleum 1(1):8–15

Li Y, Ghassemi A (2012) Creep behavior of Barnett, Haynesville, and Marcellus shale. Presented at the 46th US rock mechanics/geomechanics symposium. American Rock Mechanics Association

Mason J, Carloni J, Zehnder A, Baker SP, Jordan T (2014) Dependence of micromechanical properties on lithofacies: indentation experiments on Marcellus shale. Society of Petroleum Engineers

Naderi S et al (2016) Modeling of porosity in hydroxyapatite for finite element simulation of nanoindentation test. Ceram Int 42(6):7543–7550

Oliver WC, Pharr GM (1992) An improved technique for determining hardness and elastic modulus using load and displacement sensing indentation experiments. J Mater Res 7(6):1564–1583

Oyen ML, Cook RF (2009) A practical guide for analysis of nanoindentation data. J Mech Behav Biomed Mater 2(4):396–407

Scholz T, Schneider GA, Muñoz-Saldaña M, Swain MV (2004) Fracture toughness from submicron derived indentation cracks. Appl Phys Lett 84(16):3055–3057

Sebastiani M, Johanns KE, Herbert EG, Pharr GM (2015) Measurement of fracture toughness by nanoindentation methods: recent advances and future challenges. Curr Opin Solid State Mater Sci 19(6):324–333

Shukla P, Kumar V, Curtis M, Sondergeld CH, Rai CS (2013) Nanoindentation studies on shales. American Rock Mechanics Association

Sone H, Zoback MD (2014) Time-dependent deformation of shale gas reservoir rocks and its long-term effect on the in situ state of stress. Int J Rock Mech Min Sci 69:120–132

Tabor D (1978) Phase transitions and indentation hardness of Ge and diamond. Nature 273 (5661):406

Tanguy M, Bourmaud A, Baley C (2016) Plant cell walls to reinforce composite materials: relationship between nanoindentation and tensile modulus. Mater Lett 167:161–164

Ulm F-J, Vandamme M, Bobko C et al (2007) Statistical indentation techniques for hydrated nanocomposites: concrete, bone, and shale. J Am Ceram Soc 90(9):2677–2692

Vandamme M, Ulm F-J (2009) Nanogranular origin of concrete creep. PNAS 106(26):10552–10557

Wang X et al (2015) High damage tolerance of electrochemically lithiated silicon. Nat Commun 6:1–7

Wu Z, Baker TA, Ovaert TC et al (2011) The effect of holding time on nanoindentation measurements of creep in bone. J Bio Mech 44(6):1066–1072

Xiao G, Yang X, Yuan G, Li Z, Shu X (2015) Mechanical properties of intermetallic compounds at the Sn-3.0 Ag-0.5 Cu/Cu joint interface using nanoindentation. Mater Des 88:520–527

Yuan CC, Xi XK (2011) On the correlation of Young's modulus and the fracture strength of metallic glasses. J Appl Phys 109(3):1–5

Zargari S, Prasad M, Mba KC, Mattson ED (2013) Organic maturity, elastic properties, and textural characteristics of self resourcing reservoirs. Geophysics 78:D223–D235

Zhu W, Hughes JJ, Bicanic N, Pearce CJ (2007) Nanoindentation mapping of mechanical properties of cement paste and natural rocks. Mater Charact 58(11–12):1189–1198